University of Massachusetts Amherst
ScholarWorks@UMass Amherst

Doctoral Dissertations 1896 - February 2014

1-1-1979

The physics of poly(ethylene oxide)/poly(methyl methacrylate) blends.

Dennis Mark Hoffman
University of Massachusetts Amherst

Follow this and additional works at: https://scholarworks.umass.edu/dissertations_1

Recommended Citation
Hoffman, Dennis Mark, "The physics of poly(ethylene oxide)/poly(methyl methacrylate) blends." (1979). *Doctoral Dissertations 1896 - February 2014*. 642.
https://scholarworks.umass.edu/dissertations_1/642

This Open Access Dissertation is brought to you for free and open access by ScholarWorks@UMass Amherst. It has been accepted for inclusion in Doctoral Dissertations 1896 - February 2014 by an authorized administrator of ScholarWorks@UMass Amherst. For more information, please contact scholarworks@library.umass.edu.

THE PHYSICS OF
POLY(ETHYLENE OXIDE)/POLY(METHYL METHACRYLATE)
BLENDS

A DISSERTATION PRESENTED

BY

DENNIS MARK HOFFMAN

SUBMITTED TO THE GRADUATE SCHOOL OF THE

UNIVERSITY OF MASSACHUSETTS IN PARTIAL FULFILLMENT

OF THE REQUIREMENTS FOR THE DEGREE OF

DOCTOR OF PHILOSOPHY

AUGUST 1979

DEPARTMENT OF POLYMER SCIENCE AND ENGINEERING

(c) Dennis Mark Hoffman 1979

ALL RIGHTS RESERVED

The Physics of Poly(ethylene oxide)/Poly(methyl methacrylate) Blends

A Dissertation Presented

By

Dennis Mark Hoffman

Approved as to style and content by

(ISAAC C. SANCHEZ), Chairman of Committee

(WILLIAM J. MACKNIGHT), Head of Department

(ROGER S. PORTER), Member

August 1979

DEDICATED TO MY PARENTS

ACKNOWLEDGEMENTS

The author wishes to express his gratitude to the late Professor Fraser P. Price, without whose help this work would never have been started, and to Dr. Isaac C. Sanchez, without whose help this work might never have been finished.

Thanks also to Professor R. S. Porter for his encouragement and to Professor W. J. MacKnight for his constructive criticism. The discussions with and suggestions from members of the late Professor Price's research group are warmly acknowledged; especially those of Beata J. Abbs, Michael Wolkowicz, and Charles H. Sherwood. Edward Roche deserves a thank you for his assistance with the attempted small angle x-ray measurements, and Frederick L. Cummings for his good dinners.

The author is indebted to June Clements for typing this thesis and to several people at Lawrence Livermore Laboratory for their understanding and encouragement during the final stages of its completion, especially Walt Haefele and Mary Lewis.

ABSTRACT

The Physics of
Poly(ethylene oxide)/Poly(methyl methacrylate)
Blends

(August 1979)

Dennis Mark Hoffman, B.S., Juniata College
Ph.D., University of Massachusetts

Directed by: Professor Isaac C. Sanchez

Blends of poly(ethylene oxide), PEO, and poly(methyl methacrylate), PMMA, exhibit unique morphology, depression of spherulite growth rates with increasing PMMA concentration, and a complex transition behavior. The morphology and crystallization behaviors are functions of the glass transition of the blend. With increasing PEO content, the blend changes from a glass to a highly crystalline solid as shown by optical and electron microscopy. Based on the behavior of the glass transition, the spherulite growth rate, and morphological evidence, the PEO/PMMA blend is shown to be compatible at all compositions above the melting point of the PEO.

The temperature dependence of spherulite growth follows the well-known Fischer-Turnbull expression if a WLF modification of the diffusion term is used. If the glass transition temperature varies according to a Fox type equation, the depression of the spherulite growth rate follows from the hypothesis of compatibility in the melt.

Further evidence supporting the contention of melt compatibility is found from the shift in the dynamic mechanical tan delta maxima and DSC transition phenomena. At intermediate compositions these types of measurements are difficult to interpret because recrystallization and melting phenomena occur near T_g. Morphological and crystallization behaviors are used to show that these compositions are also compatible.

TABLE OF CONTENTS

INTRODUCTION

The purpose of this thesis is to demonstrate that the polyblend of poly(ethylene oxide) and poly(methyl methacrylate) exist in the molten state as an intimate mixture on the molecular level. The evidence for this conclusion comes from the variation of morphology and crystallization behaviors with blend composition and from dynamic mechanical and differential scanning calorimetry studies.

A compatible mixture or blend of two polymers is one in which the components are miscible at the molecular level. If phase separation occurs when the polymers are mixed, then the system is incompatible. Phase separation can occur in the liquid state or on crystallization if the component polymers can crystallize. The first chapter deals with the theoretical and historical background of polymer-polymer phase transitions, crystallization, and polymer morphology. In Chapter II, a discussion of the preparation of the polyblend and of experimental techniques used to characterize it is given. From the experimental results explained in Chapter III, it is concluded that the PEO/PMMA system is compatible above the melting point of PEO. Lastly, a discussion of some of the problems encountered during the course of this research is given, and some suggestions for further work are made.

CHAPTER I

THEORETICAL AND HISTORICAL BACKGROUND

In this chapter the reader is given some background on the theoretical treatments of polymer solutions and crystallization so that the results and conclusions of this research will be clear. Many aspects of the various theories will not be mentioned since they are not essential to the conclusions presented. In most cases the development of equations will be incomplete, but reference to complete information is provided.

The general approach to theories of liquids used will be that of thermodynamics and statistical mechanics. The system is modeled by either a partition function, Z, or a free energy function, G. These functions contain a complete description of the thermodynamics of the system. For the appropriate choice of independent variables (T and P) we have[39,40]

$$G(T,P) = H-TS = -kT \ln Z(T,P) \qquad (1)$$

where G is the Gibbs free energy; H is the enthalpy; T is the temperature; S is the entropy; P is the hydrostatic pressure; and k is Boltzmann's constant. Thus the object of the section on solution theories will be to examine expressions for H and S or equivalently Z.

In the section on crystallization a brief review of classical theories of nucleation and growth along with more recent aspects of polymer crystallization is presented. The spherulite growth rate

temperature dependence is discussed using the Fischer-Turnbull equation. Overall crystallization kinetics, as measured by DSC and dilatometry, are discussed in terms of the Avrami equation. Some of the problems associated with using this equation are pointed out.

Finally the morphology of crystalline polymers under quiescent conditions is reviewed with special emphasis on the behavior of PEO. Because of the controversy currently in the literature regarding the morphology of the amorphous state, this morphology is not considered in detail. Polymer morphology is also an extremely broad subject and, of necessity, many aspects are not included or discussed with extreme brevity. Here again references to the original literature are provided.

A. Solution Theories

In 1875 J. W. Gibbs[1] showed that the equilibrium conditions for a multiphase, isolated system were that the chemical potentials of a given component be equal in each phase. Ideal and regular solutions[2,3] of low molecular weight solvents and high molecular weight polymers[4,5] have been modeled using lattice statistics to calculate the entropy and the van Laar approximation for the energy.

1. The Flory-Huggins theory. The Flory-Huggins[6,7] theory of polymer solutions approximates the number of ways of arranging xn_2 polymer segments on N lattice sites as a product of the number of ways Υ_{i+1}, of arranging the $(i+1)^{th}$ chain taken over all chains.

$$\gamma_{i+1} = \left[(N-xi)! \;/\; [N-x(i+1)]! \right] \cdot [(z-1) / N]^{x-1} \qquad (2)$$

The number of ways of arranging all polymer segments is then

$$\Omega = \frac{1}{n_2!} \prod_{i=1}^{n_2} \gamma_{i+1}$$

Using Boltzmann's equation for the entropy, Scott[8] has shown that for two polymers

$$\Delta S = - \frac{kV_m}{V_r} \left[\left(\phi_1/x_1 \right) \ln \phi_1 + \left(\phi_2/x_2 \right) \ln \phi_2 \right] \qquad (3)$$

where ϕ_i is the volume fraction of polymer i. If van Laar's approximation[2,9] is used for the enthalpy of mixing, ΔH_m,

$$\Delta H_m = V_m \left(\delta_1 - \delta_2 \right)^2 \phi_1 \phi_2 = \frac{V_m}{V_r} RT \chi_{12} \phi_1 \phi_2 \qquad (4)$$

then the Gibbs free energy of mixing, ΔG_m, is given by[8,10]

$$\Delta G_m = \frac{RTV_m}{V_r} \left[\frac{\phi_1}{x_1} \ln \phi_1 + \frac{\phi_2}{x_2} \ln \phi_2 + \chi_{12} \phi_1 \phi_2 \right] \qquad (5)$$

where V_m is the volume of the mixture; V_r is the reference volume; n_i is the number of moles of polymer i; χ_{12} is the interaction parameter between the two polymer segments; x_i is the number of lattice sites per mole of polymer i; and δ_i is the solubility parameter. In this case

$$\phi_1 = \frac{x_1 n_1}{x_1 n_1 + x_2 n_2} \quad ; \quad \phi_2 = \frac{x_2 n_2}{x_1 n_1 + x_2 n_2}$$

Figure 1 is a plot of equation (5) for two hypothetical polymers of the same molecular weight with changing interaction parameter. The critical

condition for the onset of phase separation is given by[10]

$$\left(\frac{\partial^2 \Delta G_m}{\partial \phi_1^{\,2}} \right)_{T,P} = \left(\frac{\partial^3 \Delta G_m}{\partial \phi_1^{\,3}} \right)_{T,P} = 0 \qquad (6)$$

This defines the plait point or the maximun in the binodal and spinodal curves for upper critical solution temperature (UCST) composition diagrams. The spinodal (the limit of instability of the homogeneous phase) is given by

$$\left(\frac{\partial^2 \Delta G_m}{\partial \phi_1^{\,2}} \right)_{T,P} = 0 \qquad (7)$$

and the binodal (the limit of metastability of a homogeneous phase) is given by

$$\mu_1' = \mu_1'' \qquad (8)$$

$$\mu_2' = \mu_2''$$

where the prime and double prime represent the two incompatible phases. Figure 2 shows the spinodal, binodal and plait or critical point obtained from conditions (6) - (8) applied to equation (5).

As shown in Figure 1, in the Flory-Huggins theory the mixing enthalpy is the factor that determines whether the two polymers are miscible at a given temperature. From equations (6) and (8) the critical value of the interaction parameter is

$$\chi_{12}\,(\text{critical}) = \frac{1}{2}\left(x_1^{-1/2} + x_2^{-1/2} \right)^2 \qquad (9)$$

Several other approaches to the polymer solubility problem have been

proposed because of the limitations of the Flory-Huggins theory; namely, (1) no volume change on mixing, (2) the lattice approximation for the entropy of mixing, and (3) entropic and concentration dependence of the interaction parameter. Considering these limitations, the Flory-Huggins theory predicts the molecular weight and concentration behavior surprisingly well.

2. Heats of solution and the solubility parameter approach. The solubility parameter approach ignores the entropy term and then semi-empirically correlates polymer structure to the cohesive energy density. Scatchard[14] has shown that, neglecting the volume change on mixing and any concentration dependence of a 1-2 pair interaction, the cohesive energy of the mixture, ε_x, may be expressed as the sum of the energies, ε_{ij}, of interaction of 11, 12, and 22 pairs.

$$\varepsilon_x = \kappa \left[\phi_1^2 \, \varepsilon_{11} + 2 \, \phi_1 \, \phi_2 \, \varepsilon_{12} + \phi_2^2 \, \varepsilon_{22} \right] \tag{10}$$

where κ is a constant proportional to the total number of pair interactions in the system.[15-17] The energy change on mixing is simply the difference between ε_x and the energies of the two pure liquids.

$$\begin{aligned} \Delta\varepsilon_m &= \kappa \left[\phi_1 \, \varepsilon_{11} + \phi_2 \, \varepsilon_{22} \right] - \varepsilon_x \\ &= \kappa \left(\varepsilon_{11} - 2\varepsilon_{12} + \varepsilon_{22} \right) \phi_1 \phi_1 \end{aligned} \tag{11}$$

Scatchard assumed

$$\varepsilon_{12} = \left(\varepsilon_{11} \, \varepsilon_{22} \right)^{1/2} \tag{12}$$

which permitted him to eliminate ε_{12} from equation (11). This assumption removes the possibility of energetically favorable interactions on mixing since now $2\varepsilon_{12} \leq \varepsilon_{11} + \varepsilon_{22}$. From (11) and (12) the energy density is

$$\frac{\Delta\varepsilon_m}{V} = \kappa \left[\left(\frac{\varepsilon_{11}}{V}\right)^{1/2} - \left(\frac{\varepsilon_{22}}{V}\right)^{1/2} \right]^2 \phi_1 \phi_2 = \kappa \phi_1 \phi_2 \left(\delta_1 - \delta_2\right)^2 \qquad (13)$$

which is one definition of the solubility parameter, δ_i.

Many authors[18-21] have tried to correlate solubility and solubility parameters to polymer structure. There are several excellent reviews[3, 11-13] of the solubility parameter approach in the literature. Small[18] catalogued four types of intermolecular interactions and showed that if dispersion forces are the predominant type of interaction, the chemical structure of the components can be correlated with the solubility parameter by the equation

$$\delta = \left(\Sigma f_i / V \right) \qquad (14)$$

where f_i is the molecular attraction coefficient of the i-group in the polymer repeat unit.

If the size and shape of the two components are different, if the volume changes on mixing, or if a specific interaction occurs in the mixture; the geometric mean approximation (equation 12) breaks down. For favorable polar or chemical interactions the interaction energy of the 1-2 pair may be greater than that of the pure component. Approaches which allow for negative mixing energies[14,18,24] and empirical extensions of the solubility parameter to favorable interactions[19-23] have been proposed. The empirical approach defines solubility parameters for

each type of interaction and then sums these for the total solubility parameter. Most solvents for a given polymer fall within a given radius of δ while nonsolvents fall outside this radius. Unfortunately the total solubility parameter can no longer be used to calculate a theoretical heat mixing.

Drago, et al.,[24] have used equation (11) without assuming $\varepsilon_{12} = \varepsilon_{21}$. The resulting four-parameter equation correlates a very large number of acid-base enthalpies of mixing for low molecular weight solvents. Drago was able to predict enthalpies of mixing for hard and soft acid-base reactions. This analysis has been used to explain filler behavior[25] and could perhaps be used to explain acid-base polymer-polymer association complexes such as poly(acrylic acid)-poly(ethylene oxide)[26] and poly(vinyl chloride)-poly(methyl methacrylate)[27] complexes. It might also explain the negative interaction parameters observed in poly(ε-caprolactone)-poly(vinyl chloride)[28] and poly(vinylidene fluoride)-poly(methyl methacrylate)[29] blends.

Smolders and Koenhen[30] have compared polymer solubility parameters with other measurable quantities such as surface tension, refractive index, and dipole moment with some success. This empirical approach has proven very useful if the molecular attraction coefficients for the particular type of interaction has been tabulated. The solubility parameter approach does not account for molecular weight dependence, and there are many important solvents such as alcohols that consistently fall in the insoluble region of the circle but dissolve the polymer.

Clearly a generalized approach to heats of solution would be useful.

Further, experimental techniques for measuring this quantity in polymer-polymer mixtures need to be developed. The solubility parameters approach or perhaps Drago's approach should be set in a more theoretical basis so that these empirical results could be extended or easily incorporated into theory.

3. Equations-of-state. Although the Flory-Huggins theory predicts the correct qualitative behavior of upper critical solution temperatures (UCSTs), it cannot predict lower critical solution temperatures (LCSTs) observed in many polymer-solvent[31-33] and polymer-polymer[34,35] mixtures. One limitation of this theory is that it is independent of the physical properties of the pure components. More recent equation-of-state theories incorporate the pressure, P, volume, V, and thermal properties of the pure components into the free energy of mixing or the partition function.

a. Flory's equation-of-state. The equation-of-state approach has been recently reviewed by Curro.[38] Flory and coworkers[36] have simplified Prigogine's[41] cell theory and obtained a canonical ensemble partition function

$$Z(TV) = Z_{int}(T)\left[Z_{ext}(TV)\right]^{3crN} \exp\left(-E_0/kT\right) \qquad (15)$$

where c is the average number of external degrees of freedom per segment available to the molecule; $Z_{int}(T)$ is the partition function for Flory-Huggins theory; $Z_{ext}(TV)$ is a function of volume and temperature; and E_0 is the mean intermolecular energy. In reduced variables Flory's equation is

$$\frac{\tilde{P}\tilde{v}}{\tilde{T}} = \frac{\tilde{v}^{1/3}}{\tilde{v}^{1/3}-1} - \frac{1}{\tilde{v}\tilde{T}} \qquad (16)$$

where the reduced variable $\tilde{X}$ is the ratio of the variable X measured under any set of conditions compared to a reference value X*; i.e., $\tilde{X} = X/X^*$.

Four fundamental parameters for a pure liquid are used to obtain the three equation-of-state reference values (T*, the characteristic temperature; P*, the characteristic pressure; and v*, the hard core volume of a segment). It can be shown[42] that when this equation is applied to mixtures both UCST and LCST behaviors are predicted.

b. Sanchez and Lacombe's equation-of-state. Another PVT theory based on Ising lattice statistics has been developed by Sanchez and Lacombe.[37] Using the partition function for the pressure ensemble with volume changes arising from allowing the lattice to contain empty sites or holes, their equation for a pure fluid in reduced variables is

$$\tilde{\rho}^2 + \tilde{P} + \tilde{T}\left[\ln\left(1-\tilde{\rho}\right) + \left(1 - \frac{1}{r}\right)\tilde{\rho}\right] = 0 \qquad (17)$$

In this case the equation-of-state parameters P*, T* (the characteristic pressure and temperature), and $v^*_{sp} = 1/\rho^*$, the close packed specific volume are related to the molecular properties E*, the segment-segment interaction energy v*, the close packed segment volume, and r, the number of segments per molecule. Using two mixing rules to determine the hard core volume of the mixture and the number of close packed pair interactions, the equation-of-state for mixtures is the same as that for the pure fluid. Now, however, the reduced variables are related to the concentration of each component in the mixture.

According to this theory, the requirement for phase stability (spinodal condition) depends on three parameters, χ, β, and ψ. The four types of temperature composition diagrams predicted by the theory are shown in figure 3. The interaction parameter, χ, varies inversely with temperature so that positive values of χ produce UCST behavior just as in the Flory Huggins theory. On the other hand, the isothermal compressibility, β, has a positive temperature coefficient as required for LCST behavior.[43] The parameter ψ is squared in the equation for phase stability and can only contribute to LCST behavior.

The theory predicts several interesting results. (1) All mixtures will exhibit LCST behavior unless vaporization or degradation occurs first. (2) The UCST and LCST behaviors are coupled inversely to the molecular weight so that as the molecular weight increases the UCST and LCST approach each other and ultimately merge to form hour-glass shaped temperature composition diagrams. This result is consistent with experimental behavior.[44,45] (3) For high molecular weight polymers to be compatible, χ must be very small or negative and the pure component parameters T*, P*, and v* must be similar.

B. Polymer Crystallization

1. Classical nucleation theory. The inception of nucleation theory is again attributed to Gibbs.[1] For a fluctuation or crystal embryo to grow, it must reach a critical size where the free energy gained by crystallization equals the energy required to create new surface in the

mother liquor. Becker and Doring[46] and Volmer[47] applied this condition to low molecular weight crystals and were able to demonstrate that at low supercoolings nucleation rates are inversely proportional to the temperature. Turnbull and Fischer[48] realized the importance of the change in viscosity of the liquid with temperature. This effects the transporting of liquid across the liquid-crystal interface, and the Turnbull-Fischer equation, with some modification, is used in theories of polymer crystallization today.

Shortly after the discovery of chain-folded polymer single crystals[49-51] two schools of thought regarding polymer crystallization arose. Peterlin,[52] et al., proposed an equilibrium theory of chain vibrations as a function of temperature. On the other hand, several authors[53-55] proposed a kinetic approach based on the work of Turnbull and Fischer. Since the equilibrium theory cannot predict crystal growth rates, it has largely been abandoned. The kinetic approach, however, has increased considerably in complexity.

Several books[56-58] and review articles[59-63] have been written on classical polymer crystallization. A brief discussion, following the review by Price,[59] is given here. The driving force for the growth of a crystal from the melt depends on the free energy difference between the crystal and the melt. Because energy is required to create new crystal surface, there will be a critical nucleus size where the bulk free energy of a specific number of molecules equals the surface energy. Addition of molecules to crystals larger than the critical nucleus is always thermodynamically favorable, and so these nuclei grow. For a

cubic crystal of dimensions η, μ, and ν with unit cell dimensions a_o, b_o, and c_o, the Gibbs free energy is given by

$$\Delta G = -\eta c_o \mu b_o \nu a_o \Delta f + 2\mu\nu a_o b_o \sigma_e$$
$$+2\sigma\left|\eta\mu c_o b_o + \nu\eta a_o c_o\right| \qquad (18)$$

where σ_e is the surface free energy normal to the c-axis and σ is the surface free energy of the other four faces. Δf is the bulk free energy of an infinitely large crystal per unit volume of crystal.

The dimensions of the critical nucleus are determined by the location of the saddle point on the free energy surface given by equation (18).

$$\frac{1}{c_o}\left(\frac{\partial \Delta G}{\partial \eta}\right) = 0 = -\nu\mu a_o b_o \Delta f + 2\sigma\left|b_o\mu + a_o\nu\right|$$
$$\frac{1}{b_o}\left(\frac{\partial \Delta G}{\partial \mu}\right) = 0 = -\nu\eta a_o b_o \Delta f + 2\sigma_e a_o \nu + 2\sigma c_o \eta \qquad (19)$$
$$\frac{1}{a_o}\left(\frac{\partial \Delta G}{\partial \nu}\right) = 0 = -\mu\eta b_o c_o \Delta f + 2\sigma_e b_o \mu + 2\sigma c_o \eta$$

Crystal formation that takes place in pure supercooled melt is called homogeneous nucleation, and the free energy of formation of a critical nucleus is found by solving for the critical nucleus dimensions from the saddle point conditions and then substituting these dimensions into equation (18).

$$\Delta G_{Homogeneous} = \frac{32\sigma^2\sigma_e}{\Delta f^2} \tag{20}$$

Hetergeneous nucleation occurs if the embryo crystallizes on an already existing heterogeneity. If the difference between the interfacial free energy of the crystal and the melt and the interfacial free energy of the heterogeneity and the crystal is $\Delta\sigma$, then

$$\Delta G_{Heterogeneous} = \frac{16\sigma\sigma_e\Delta\sigma}{\Delta f^2} \tag{21}$$

For nucleation on an already existing crystal surface

$$\Delta G = \frac{4b_o\sigma\sigma_e}{\Delta f} \tag{22}$$

Obviously, the lower free energy of formation of the critical nucleus makes heterogeneous nucleation the favored kinetic process. In fact, interactions between the polymer melt and heterogeneous nucleating agents can occur well above the equilibrium melting temperature.[48b]

Problems encountered when applying classical nucleation theory to polymer crystallization should be mentioned. Several authors[54b,55,65] have pointed out that classical theory does not recognize the long chain nature of the crystallizing polymer. Each polymer segment is interconnected to the next and must align itself in the crystal accordingly. Computer modeling of the nucleation phenomena[66] gives a temperature dependence similar to that of classical nucleation theory but very rough nuclei instead of the minimized surface energy nuclei of classical

theory. The problem of chain folding in other than an adjacent reentry mechanism[67] and fluctuations in the fold surface cannot be treated without using a variable fold surface free energy. It has been proposed[68,69] that the addition of each macromolecule determines the kinetics of growth instead of the classical free energy barrier, but this approach leads to the classical result, equation (22), so that it is very difficult to demonstrate this effect.

2. Recent kinetic theories. Lauritzen, Passaglia, and DiMarzio[65] have derived kinetic equations for multicomponent chains which have been applied to model polymer crystallization.[70] If a layer or strip of molecules is allowed to grow on a crystal face for a system of n components with only nearest neighbor interactions along the chain, the ratio of currents, S (the rate at which a strip is attached and detached), to occupation numbers, Q (the number of crystals with a site where a crystal strip can be attached), is a constant. This constant depends only on the terminal species of the chain and the occupation number, but is independent of the other components and the length of the chain. Further, if a series of cyclic steps (such as the formation of a stable nucleus by attachment of many segments of a polymer) is independent of the polymer already in the crystal, the rate constants for the attachment and removal of segments (α and β) may be replaced by rate constants for the overall process, A and B.

Energies of activation of the forward and backward rate constants are assigned from absolute rate theory.[71]

$$\alpha_0 / \beta_1 \propto \exp \left(-\Delta G_1 / kT \right) \qquad (23)$$

$$\alpha \; / \; \beta \propto \exp - \left(\Delta G_i - \Delta G_{i-1} \; / kT \right) \tag{24}$$

Further analysis of the crystallization kinetics depends on the model for the free energy of nucleation from the liquid, ΔG_i, and the free energy change on addition of the i^{th} stem or segment to an already existing nucleus ($\Delta G_{i-1} - \Delta G_i$). For a model similar to that of classical nucleation, equations (20) and (22), Hoffman and Lauritzen[60f] have assigned overall rate constants A_1, B_0 for initial stem attachment and A,B for subsequent attachment as

$$A_o = \beta \exp \left(-2b\ell\sigma/kT + \phi b^2 \Delta f \ell / kT \right) \tag{25}$$

$$B_1 = \beta \exp \left[-(1-\phi) b^2 \Delta f \ell / kT \right] \tag{26}$$

$$A = \beta \exp \left[-2b^2 \sigma_e / kT + \phi b^2 \Delta f \ell / kT \right] \tag{27}$$

$$B = \beta \exp \left[-(1-\phi) b^2 \Delta f \ell / kT \right] \tag{28}$$

Where terms inside the brackets have the same definitions as in the classical case except that $b = b_o$ and $\ell = c_o \nu$. The term for the transfer of liquid polymer to the crystal surface (β) has the form of the WLF equation.

$$\beta = \left(\frac{kT}{h} \right) J_1 \exp \left[-U^*/R \; (T-T_\infty) \right] \tag{29}$$

U^* represents the energy barrier to segmental motion of a polymer near T_g; J_1 is a factor accounting for noncrystallographic attachment at the crystal face, and (kT/h) is the jump frequency of classical kinetics.

The parameter ϕ is used to apportion the free energy between the forward and backward reactions.

The total current is given by

$$S_T = \frac{A_o\ (A-B)}{B_1 + (A-B)}\ N_o \tag{30}$$

and substituting the values for A_o, A, B_1, and B with equation (30), we find that the modern equation for nucleation and subsequent attachment of polymer chains to the crystal face is very similar to the classical equation (22).

$$S_T = N_o S_o \beta \exp\left(-4b\sigma\sigma_e / \Delta f k T\right) \tag{31}$$

If nucleation is the rate determining step, that is, if no further nucleation occurs before the rest of the polymer chain has laid down, the growth rate, G, is

$$G = bS_T h_s / N_A = bLS_T / aN_A \tag{32}$$

where N_A is Avagadro's number; h_s is the number of nucleation sites per crystal surface; a is the unit cell dimension along the fold direction; and L is the length of the crystal substrate surface. Substituting (29) and (31) into (32) and collecting constants, an expression similar to the Fischer-Turnbull equation is obtained.

$$G = G_o \exp\left[-U^*/R\left(T-T_\infty\right)\right] \exp\left[-4b\sigma\sigma_e / \Delta f k T\right] \tag{33}$$

At low supercoolings, <u>i.e.</u>, slightly below the polymer melting point nucleation is infrequent and crystal growth slow so that equations (32)

and (33) hold reasonably well. Obviously, however, at large supercoolings polymer crystals grow rapidly and multiple nucleations probably occur before all of the segments from a single chain have been incorporated into the crystal.

Sanchez and DiMarzio[70] have shown that as the rate of nucleation approaches the rate at which subsequent chain is attached, the growth rate is expected to depend on the square root of the total nucleation rate, S_T. Thus

$$G = b\left(S_T g/a\ N\right)^{1/2} \tag{34}$$

where $g = a(A-B)$ is the rate at which the polymer crystal stems spread across the crystal surface. This reduces the last term in equation (33) by a factor of two and changes G_o by $1/\left[n_s \exp\left(ab\sigma_e/kt\right)\right]$. Thus G_o should be much larger at low supercoolings where equation (33) applies than at high supercoolings when

$$G = G_o \exp\left[-U^*/R\left(T-T_\infty\right)\right] \exp\left[-2b\sigma\sigma_e/\Delta fkT\right] \tag{35}$$

Lauritzen and Hoffman[60] designate equation (33) and (35) regimes I and II, and Lauritzen[72] has shown that they can be distinguished from each other by the value of the slope, K_g, of $\ln\left(G/G_o\right) + U^*/R\left(T-T_\infty\right)$ plots. Lauritzen's Z condition for distinguishing between regime I and regime II growth kinetics is

$$Z = \frac{iL^2}{4g} \cong 10^3(L/2a)^2 \exp\left(-K_g/T\Delta T\right) \tag{36}$$

where

$$Kg = Y\, b\sigma\sigma_e T^o / \Delta H_f k$$

so that for regime I kinetics, $Z \leq 0.01$ and for regime II, $Z \geq 1.0$. Solving equation (36) for L, the crystal length, in regime I we have

$$L = 2a \left[10^{-5} \exp \left(K_g / T\Delta T \right) \right]^{1/2} \qquad (37)$$

Single crystal sizes are about one micron; thus, for reasonable values of K_g, the change from regime I to regime II should require only about twenty degrees supercooling. Both regimes have been observed in polyethylene.[60g]

3. The influence of diluent. The addition of a compatible diluent to a crystallizable polymer can affect at least three aspects of the polymers crystallization kinetics. (1) Diluent can depress the melting point of the polymer and as a result decrease the amount of supercooling which slows down the crystallization rate. (2) Diluent can increase or decrease the glass transition temperature of the polymer. Increasing T_g increases the interfacial viscosity between liquid and crystal which would lower the crystallization rate. (3) As the diluent concentration increases the crystallization rate should decrease because of interference between the noncrystallizing and crystallizing components.

a. The melting point depression. The effect on the melting point of adding a compatible diluent to a crystallizable polymer may be expressed thermodynamically as the difference between the chemical potentials of the polymer crystal segments, μ_1^c, and the pure liquid polymer

segments, μ_1^o, at the same temperature and pressure.

$$\mu_1^c - \mu_1^c = -\Delta H_f \left(1-T/T_m^o\right) \tag{38}$$

Here the simplest approximation for the difference in free energy between the crystal and the melt has been assumed, i.e., $\Delta G = \Delta H_f \Delta T/T_m^o$. It is also assumed that no diluent is incorporated into the crystal and that the equilibrium melting point, T_m^o, is that of large perfect crystals.

The chemical potential of a polymer segment, μ_1, in a polymer-diluent mixture will be lower than for pure polymer, μ_1^o, by the derivative of Scott's[8] free energy of mixing (equation 5) with respect to a segment of crystallizable polymer $(x_1 n_1)$[27,73]

$$\mu_1 - \mu_1^o = \frac{RTV_1}{V_r}\left[\frac{1}{x_1} \ln \phi_1 + \left(\frac{1}{x_1} - \frac{1}{x_2}\right)\phi_2 + \chi_{12}\,\phi_2^2\right] \tag{39}$$

The equation predicts the decrease in chemical potential of the polymer-diluent mixture, μ_1, relative to the pure polymer liquid. At the melting point, T_d, the chemical potentials of the crystal and the polymer-diluent mixture must be equal. Equating T and T_d^o in equation (38) and (39) and rearranging yields, Flory's[74] well-known equation for the melting point depression of a polymer crystal and also the first approximation used by Sanchez and DiMarzio.[70b]

$$1/T_d^o - 1/T_m^o = \frac{-RV_1}{V_r \Delta H_f}\left[\frac{1}{x_1} \ln \phi_1 + \left(\frac{1}{x_1} - \frac{1}{x_2}\right)\phi_2 + \chi_{12}\,\phi_2^2\right] \tag{40}$$

where ϕ_2 is the volume fraction of polymer diluent. If x_1 and x_2 are very large

$$1/T_d^o - 1/T_m^o = \frac{-RV_1}{V_r \Delta H_f}\left(\chi_{12}\,\phi_2^2\right) \tag{41}$$

thus for two high molecular weight polymers, no melting point depression is expected unless χ_{12} is negative. Melting point elevation is apparently not possible since χ_{12} would have to exceed χ_{12} (critical).

Figure 4 is a plot of the expected melting point depression for PEO crystals based on equation (40). The values for ΔH_f, the heat of fusion per gram of repeating unit, and T_m^o, the equilibrium melting point of pure PEO, are given in Table III of Chapter III. For low molecular weight diluents ($x_1 = 1$; solid lines in figure 4) significant melting point depressions are predicted even for large positive χ_{12} values. High molecular weight diluents ($x_1 = x_2 = 10^5$; dotted lines in figure 4) do not show melting point depressions unless χ_{12} is large and negative.[73,74] More than 60 volume percent of high molecular weight, extremely good solvents ($\chi_{12} = -3$) must be added to the crystallizable polymer to achieve greater than 15^oC melting point depression. Since the interaction parameter is usually positive or zero,[34b] only for very favorable polymer-polymer interactions should the equilibrium melting point of a blend be lowered.[77,78]

Where liquid-liquid phase separation occurs, any composition between the two equilibrium compositions separates into the equilibrium compositions. Since the term in brackets in equation (40) is the chemical potential for a segment of polymer in diluent at T_d times a constant factor, between the equilibrium compositions this term will not change. Thus the melting point of the mixture is constant because the crystallizing polymer sees only the equilibrium composition regardless of the initial composition of the mixture until the mixture

composition passes beyond the limit of metastability on the opposite side of the phase diagram. In the region between the two equilibrium compositions neither the equilibrium dissolution temperature (as indicated by the dashed lines in figure 4) nor the crystal growth rate will change. This result has been observed for polymers crystallizing from low molecular weight diluents in several instances.[75,76]

In many instances the viscosity,[78] mechanical history,[79] or thermal history[80] of the blend produce small crystals in a highly nonequilibrium state. From the previous discussion of chain folded crystals, it should be evident that the crystallite size, which depends on crystallization temperature, also affects the melting point. Because of the small crystallites, the method of Hoffman and Weeks[84] could be applied at each concentration to determine $T_d^o(\phi_2)$ and then equation (40) used to obtain the interaction parameter. In the two cases in which this technique has been used,[73,78] negative or zero values of the interaction parameter are found for compatible blends.

Although Mandelkern[81] and others[82,83] have shown that for dilute solution crystallization the fold surface free energy is independent of solvent at low supercoolings. This is not necessarily expected to be the case with polymer diluents, especially at high diluent concentration or high supercoolings. As the rate of crystallization increase, polymer diluent entanglements would raise the fold surface free energy. This will also cause an apparent depression of the polymer blend melting point.

The influence of diluent on the total current, S_T, is expected to

be related to the number of crystalline segments available for attachment to the crystal face from the mother liquor. Most authors[56,62,74,85,86] who have considered the effect of concentration include a term of the form

$$S\left(\phi_1\right) = \phi_1 S_T \tag{42}$$

in equation (33). In some cases this term has been incorporated into the bulk free energy term to express the excess entropy associated with loose folds. It is not clear that this procedure is necessary. At low crystalline polymer concentrations, the inadequacy of the approximation is evidently caused by competition between cilia and regular nucleation.[70b,87,88] A better approximation might be to replace ϕ_1 by the fraction of amorphous, crystallizable polymer, but this would result in a decrease in growth rate with time. Keith and Padden[141] found constant growth rates with increasing diluent concentration resulting from the lamella tips projecting into virgin melt and leaving the noncrystalline material to fill the intersticies of the spherulite. Since the growth rate of atactic-isotactic polystyrene blends,[90] for example, is constant for a given concentration of atactic polystyrene and temperature, equation (42) should be satisfactory. Note that including the concentration term affects only the pre-exponential in the growth rate equation.

b. Effect of diluent on Tg. Hoffman, et al.,[60] have shown that the diffusion term for bulk polymers is

$$\beta = \exp\left[-U^*/R\left(T-T_\infty\right)\right]$$

where U*, the activation energy for segmental motion near the liquid-crystal interface, is much lower than would be expected from viscosity measurements,[91] and T_∞ is higher than would be expected from the WLF equation.[92] Various authors[60,93-95] have found that U* is approximately 1500 cal/mole of repeat units, and T_∞ is thirty degrees below T_g for many crystalline polymers and sterically hindered low molecular weight compounds.

The effect of diluent on T_∞ should be the same as that on T_g. Either the Gordon-Taylor[96] expression (generally applied to copolymers[97])

$$T_g = \left[T_{g_1} + \left(kT_{g_2} - T_{g_1}\right) W_2\right] \Big/ \left[1 - (1-k)\, W_2\right] \qquad (43)$$

where k is a constant and W_2 is the weight fraction of component 2, or the Fox[221] equation

$$T_g = W_1/T_{g_1} + W_2/T_{g_2} \qquad (44)$$

can be used to describe the composition dependence of T_∞ in a compatible blend. Experimental viscosity measurements for low[98] and high[99] molecular weight diluents have been shown to follow this equation.

Figure 5 shows the effect of increasing glass transition on the spherulite growth rate calculated from

$$G = G_o \exp\left[-K_g/T\,\left(T_m^o - T\right)\right] \exp\left[-K_D/T-T_\infty\right] \qquad (45)$$

allowing T_∞ to vary according to the Fox equation. K_g is defined in equation (36) and K_D is U*/R. The values used for calculating figure 5 are given in Table III of Chapter III. The growth rates indicated by

solid lines in the figure are calculated assuming sufficiently high molecular weight diluent to preclude significant melting point depression unless χ_{12} is negative.

If the interaction parameter is large and negative (χ_{12} = -3 is used in figure 5 indicated by the dotted lines), the difference between the free energy of the pure crystal and the diluent containing melt is

$$\Delta f\left(\phi_2\right) = \Delta H_u \left(T_d^o - T\right) / T_d^o \qquad (46)$$

where T_d^o may be calculated from equation (41). Using this result in equation (45) decreases the growth rate only slightly and shifts the growth rate maxima to lower temperatures as shown by the second set of curves in figure 5. The effect becomes most pronounced at high diluent concentrations and low degree of supercoolings.

4. Overall crystallization kinetics and the Avrami equation. The kinetics of crystallization of polymer spherulites are governed by two phenomena. The first, birth of the crystalline phase in the melt, is called primary nucleation and the second is subsequent growth of the primary nuclei. The overall kinetics of crystallization can be described by the Abrami equation.[100,101] Consider N identical spheres in a total volume V_o. Assuming that no impingement occurs, the volume of a sphere, v, at time, t, is $(4/3)\pi R(t)^3$ where R(t) is the radius of the sphere. If the spheres are put randomly into the volume, the probability that the first sphere falls into a small volume $\delta v << v$ is v/V_o and that it falls outside δv is $(1-v/V_o)$. The probability that δv lies in the amorphous region after placing all N spheres into the system is

$$\theta = \left(1-v/V_o\right)^N \tag{47}$$

Where θ is simply the volume fraction of amorphous material in the system. In the limit of large N and small v

$$\theta = \left[1 - \frac{Nv/V_o}{N}\right]^N \cong \exp\left(-Nv/V_o\right) \tag{48}$$

Substituting for v,

$$v = \frac{4}{3}\pi R^3 = \frac{4}{3}\pi (Gt)^3$$

we have

$$\theta = \exp\left[-\frac{4}{3}\pi \dot{N} G^3 t^3\right] = \exp\left(-kt^n\right) \tag{49}$$

the well-known Avrami equation for constant growth rate and fixed number of nuclei per unit volume of polymer $\dot{N}$. If the number of nuclei varies with time, the Nv term must be integrated over time.[102,103]

The density of the amorphous region and the spherical crystals are assumed to be equal. The error caused by this assumption can be as large as 10 percent.[104,105] Because of the amorphous material in polymer spherulites, Mandelkern[102] has included a factor λ, the untransformed fraction at infinite time in his version of the Avrami equation.

$$(1-\theta) = \lambda\left[1-\exp-\left(kt^n\right)\right] \tag{50}$$

Secondary crystallization,[104b] impingement,[105] multiple growth rates and nucleation rates,[106,107] and a variety of other phenomena have been invoked to explain the noninteger time dependence often observed experimentally when the Avrami equation is applied to polymer crystallization.

Solutions for k and n in equation (49) may be obtained from plots of $\ln[-\ln(\theta)]$ versus ln t. These plots should yield straight lines with slope n and intercept k. Because of the approximations in equation (48) and the impingement problem, experiment is expected to agree with theory only at low degrees of crystallinity (30 percent or less).[104,106] If the kinetics of the transformation are similar, the values of n should be the same for a constant conversion. Choosing the inflection point of equation (48), it can be shown[107] that

$$\frac{n-1}{n} = kt_{infl}^{n} \tag{51}$$

and therefore

$$n = \left[1 - \ln \theta_{infl}\right]^{-1}$$

Thus n and k can be obtained from θ_{infl}, the fraction of untransformed polymer, at t_{infl}, the time the inflection point is reached. Other methods for determining n and k have also been proposed.[108,109] One recent attempt[110] to include the effect of impingement predicts fractional n, and that n changes as crystallization proceeds; effects which are often observed.

Because of these problems, the Avrami equation gives only qualitative information regarding the nucleation and growth mechanisms of overall crystallization kinetics. However, it is an extremely useful equation for data tabulation because it describes a considerable portion of the overall crystallization behavior with two simple parameters, k and n.

C. The Morphology of PEO

The morphology of crystalline polymers is a subject too broad to cover in a thesis. For this reason and because it is the crystalline component studied in Chapter III, only the morphology of PEO will be discussed. Reviews on single crystals[111-116] as well as on bulk morphology[117-121] under a variety of conditions are available in the literature. In the following section the morphology of PEO single crystals, including their growth, folding, thickening, and deformation behaviors, is discussed. Based on the single crystal morphology and the crystal structure, PEO spherulite morphology is examined. Finally the morphology of polymer blends is considered.

1. Single crystals of PEO. Flat, lozenge-shaped PEO single crystals will grow in dilute (0.1%) zylene solution at temperatures below $35^{o}C$.[118,122,123] The unit cell is a 7/2 helix,[124] but the actual molecular weight PEO shows a large distortion of the molecules in the helix (see figure 6a). This is attributed to the flexibility of the chain caused by lack of side groups. The unit cell dimensions are $a = 8.05\text{Å}$, $b = 13.04\text{Å}$, and $c = 19.48\text{Å}$; the chain lies along the c-axis. Although other unit cells have been reported,[126] a monoclinic cell having parameters similar to those above and angle β of approximately 125.4^{o} is favored by most authors.[122b,125,127] Figure 6b is the Balta-Calleja[127] version of that cell looking down the chain axis.

Since the lamella thickness is much less (100 - 500 Å) than the length of the polymer chain (4000 Å), the chain must fold back on itself into the single crystal. Although the nature of the fold surface in polymer crystals is a matter of considerable debate, in well-organized single crystals the polymer chain folds relatively tightly back on itself to begin the next crystal stem. Evidence supporting regular folding of PEO single crystals in the (120) planes parallel to the growth face is based on wavy dark field electron micrographs in (120) sectors parallel to the growth face which are straight in sectors where the (120) diffracting spot used to produce the dark field micrograph runs normal to the growth face. The waviness of the dark field pattern is caused by the deformation of the PEO crystal lattice when the macromolecule twists out of register to make a fold. Since the pattern is distorted parallel to the crystal faces rather than perpendicular, the folds must be along this direction for the most part. Sectorization, a slight puckering of the crystals, preferential melting at the intersection of two sectors, and twinning phenomena all imply considerable regularity of the folds.

Kovacs, Gonthier and Straup[129] have studied single crystals of low molecular weight fractions of PEO grown from the melt. The growth rates of low molecular weight fractions of PEO change abruptly with increasing supercooling when the number of folds in the chain increases. The morphology near the transition temperature to the next higher number of folds varies widely depending on growth rates of the different crystal faces and the rate of isothermal thickening. Crystals that grow

at sufficient supercoolings to produce at least one fold tend to thicken spontaneously but more slowly than they grow. This produces a thick central portion of the single crystal which continues to grow until the melt is exhausted. Apparently the polymer chains have sufficient mobility in the crystal to unfold, but only as long as molten polymer is available to fill in the holes left in the folded crystal. Perhaps the molten polymer assists in the thickening process by nucleating on the thickened crystal edge and forcing itself into less perfect areas of the folded crystal. At molecular weights above 20,000 and supercoolings greater than twenty degrees, the discontinuities in the growth rate with change in number of folds are not observed. Thus, these phenomena have been attributed to the effect of chain ends on the crystallization driving force for low molecular weight polymer and the anisotropic behavior of the PEO growth faces at low supercoolings. The effect of methyl and ethyl end groups instead of hydroxy end groups reinforces the above conclusion.[130]

2. PEO spherulites. The transition from single crystal to spherulite probably varies from polymer to polymer, but in general there are four stages.[131] First, nucleation of a single crystal must occur. In concentrated solutions[132] and in the melt layers,[133] terraces, or spiral growth[134] cause the crystal to branch. A number of reasons for branching have been proposed, including nucleation on defects in the polymer surface,[135] puckering of the tentlike single crystals,[136] and recently an interesting twinning mechanism in which crystals nucleate almost perpendicularly to the original single crystal called crystal halving.[137]

Whatever the mechanism, the initial rod-like structure becomes sheaf-like. The lamellae comprising the two ends of the sheaf continue to branch until they meet, at which point the spherulite grows radially in all directions. Figure 7a shows the sequence schematically.

PEO spherulites were among the first synthetic high polymer spherulites to be observed.[138] Spherulitic morphology is found in relatively high viscosity systems. Other characteristics of polymer spherulites include constant growth rate, twisting of radiating fibers or lamellae,[139-141] and complicated fine structure. Figure 7b is an electron micrograph of the lamellar fine structure of a PEO spherulite surface.

Although some high purity organic materials[93] produce spherulites, impurities and multicomponent systems often enhance spherulite formation.[142] Block copolymers of ethylene oxide and styrene,[143-145] methyl methacrylate,[146,147] ethylene terephthalate,[148] cellulose triacetate,[149] and urethanes[150] have all been synthesized; and if the PEO molecular weight is high enough, all these copolymers form spherulites.

The morphology of blends of PEO has not been studied to any significant extent. It is known that several blends of PEO form one-to-one complexes,[10,26,151] but to the author's knowledge there are no entirely compatible blends of this polymer mentioned in the literature.

CHAPTER II

EXPERIMENTAL PROCEDURES

A. Materials

The materials used in this study were poly(ethylene oxide), poly(methyl methacrylate) and methyl methacrylate monomer, abbreviated PEO, PMMA, and MMA, respectively. The structural formula for the PEO repeat unit is

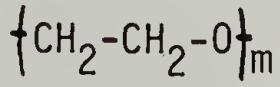

and the PMMA repeat unit is

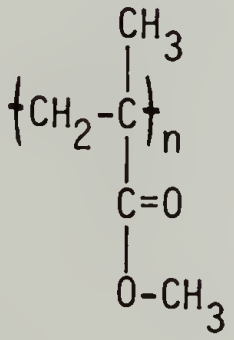

where m and n represent the degree of polymerization of PEO and PMMA. Two PEO samples having different average molecular weights were obtained from Union Carbide. The high molecular weight material, WSR-N-3000(R), had a viscosity average molecular weight of 400,000, and the low molecular weight material, Carbowax-6000(R), had a viscosity average molecular weight of 10,000. PMMA, having a viscosity average molecular weight of 350,000, was obtained from Cellomer Associates. The MMA monomer was obtained from Bordon Chemical Company and Aldrich Chemical Company.

The PEO/PMMA blends have been identified by a simple shorthand nomenclature. The polymers are identified as PEO/PMMA and the weight percent of each component is given separated by a slash. The identity of each material is abbreviated as WSR for WSR-N-3000 PEO, C6K for Carbowax 6000 PEO, $H\overline{M}$ for high molecular weight PMMA, and MMA for PMMA formed by polymerization of monomer. A colon separates the weight fractions from the polymers. For example, a 70/30 blend of WSR-N-3000 with high molecular weight PMMA would be abbreviated as PEO/PMMA:70/30: WSR/$H\overline{M}$. In some instances when MMA monomer is used, the volume of monomer is given per weight of PEO. These abbreviations are always followed by the weight percentages of PEO/PMMA in parentheses. For example, if 15g of Carbowax 6000 were dissolved in MMA monomer and polymerized to a solid, the sample will be identified either as PEO/PMMA: 15/25:C6K/MMA (40/60) or PEO/PMMA:40/60:C6K/MMA.

Viscosity average molecular weights were determined in water at $30^{o}C$ for PEO and at $25^{o}C$ in acetone for PMMA using Ubbelohde suspended level viscometers. Since flow times for the solutions were about 100 seconds, no kinetic correction was made.[152] Bath temperature was controlled to $\pm 0.1^{o}C$ and flow times were reproducible to ±0.1 percent or better.

Flow times at four concentrations were extrapolated to infinite dilution in the usual way to obtain the intrinsic viscosity, $[\eta]$, from the relative, η_r, and specific, η_{sp}, viscosities. The following relationships were used

$$\eta_r = t_1/t_o \qquad (52)$$

$$\eta_{sp} = \eta_r - 1 \tag{53}$$

$$\eta_{red} = \eta_{sp}/c \tag{54}$$

where η_{red} is the reduced viscosity; t_o is the solvent flow time; t_1 is the solution flow time; and c is the solution concentration in grams per deciliter.

The intrinsic viscosity was determined from the specific viscosity using Huggins'[153] equation

$$\eta_{sp}/c = [\eta] + k' [\eta]^2 c \tag{55}$$

and from the relative viscosity using Kraemer's equation[154]

$$\ln(\eta_r)/c = [\eta] + k'' [\eta]^2 c \tag{56}$$

where k' and k'' are constants. Figures 8-10 are plots of η_{sp}/c versus c and $\ln(\eta_r)/c$ versus c for solutions of high and low molecular weight PEO and PMMA, respectively. Linear regression analysis[155,156] requiring that equations (55) and (56) pass through the same intercept values was used to determine the intrinsic viscosities. Viscosity average molecular weights were calculated from the Mark-Howink[157] equation

$$[\eta] = KM^a \tag{57}$$

where $K = 1.25 \times 10^{-4}$ and a = 0.78 for PEO in water at 30°C.[158,159] $K = 7.5 \times 10^{-5}$ and a = 0.70 for PMMA in acetone at 25°C.[160] The molecular weights calculated from equation (57) were 9.6×10^3 for Carbowax-6000, 4.1×10^5 for WSR-N-3000, and 3.5×10^5 for PMMA.

B. Sample Preparation

Blends of PEO and PMMA were prepared by dissolving Carbowax-6000 in MMA, initiating the monomer with AIBN or benzoyl peroxide, and allowing the polymerization to continue until solid. Weighed samples of PEO were mixed with purified[161] MMA and a small amount of initiator in thick-walled polymerization tubes. The mixtures were frozen in liquid nitrogen and the test tubes were sealed under vacuum with a torch, as shown schematically in figure 11.

After sealing, the solutions were warmed slowly until the PEO in each tube had dissolved completely. The tubes were transferred to an oven at 80°C ±2°C to activate the free radical initiator. The initiation mechanism for azobisisobutyronitrile, AIBN, is[162,163]

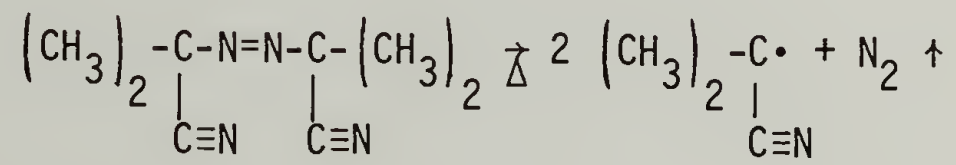

and for benzoyl peroxide is

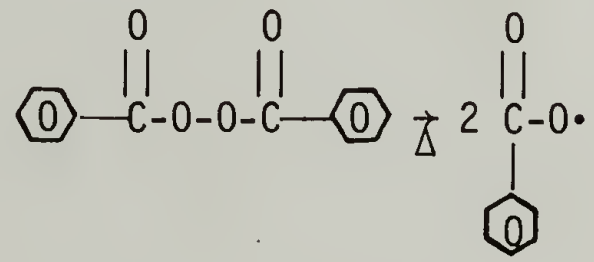

The free radical attacks the monomer double bond,

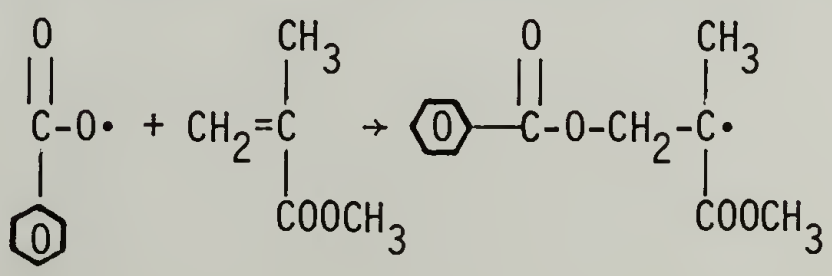

and subsequently the MMA radical attacks MMA monomer, the propagation step, to produce polymer.

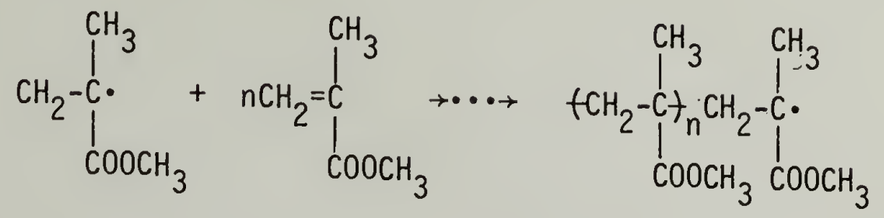

Both combination and disproportionation can terminate the polymer chain. Toward the end of the polymerization in the larger tubes (25 ml or more), the heat of reaction cannot be dissipated in the viscous mixture and depolymerization occurs. This causes bubbles in the mixtures, especially at low PEO concentrations. To minimize this problem as the solutions became viscous, the polymerization tubes were removed from the oven, cooled for a few minutes, and then replaced.

When the blends had solidified, usually after about 8 to 24 hours, the tubes were removed from the oven and cooled. In all cases when the temperature of the mixtures was above the PEO crystallization temperature, the solid produced from the polymerization was clear. At room temperature the glass was broken and the solid polymer rods removed and stored in a desiccator.

There were three problems with the polymerization technique. High molecular weight PEO did not dissolve sufficiently to make a uniform mixture before the monomer had polymerized to a solid. Also, at fifty percent or higher PEO concentration, the rate of polymerization was depressed so far that even after long times (five days), some monomer remained unpolymerized. Because of these factors and the difficulties

in characterizing the resulting PMMA, most of the experiments were carried out using blends cast from a common solvent.

Weighed mixtures of the two polymers were dissolved in warm acetone by stirring to make 5 percent solutions. Although the WSR-N-3000 PEO solutions were slightly cloudy, this did not seem to affect the cast films. The solutions were poured over glass slides in petri dishes and placed in an oven at 80°C to remove the acetone. After 10 to 24 hours, the dried films were transferred to a vacuum oven at 80°C for from 2 days to several weeks. Because the blends tended to degrade at this temperature over long periods of time, the temperature was lowered to 45°C, usually after the first few days. Howard[164] has shown that acidic additives cause polymer degradation in PEO at 70°C. If the ester interchange reaction between small amounts of water and PMMA produces catalytic amounts of carboxylic acid, this might explain the observed degradation. Samples were kept at 45°C for 2 to 5 weeks to allow the PEO to crystallize. Large spherulites formed in mixtures in which the PEO concentration was greater than 60 percent; crystallization was evident until the PEO concentration dropped below 30 percent. Non-crystalline blends containing less than 30 percent PEO were optically clear.

C. Morphological Techniques

1. Optical measurements. Two Zeiss Standard Research Polarizing Microscopes, types GFL and WL, were used in the photomicrographic growth

rate studies. Long working distance objectives must be used with the Mettler FP-2 hot stage. The magnification and numerical aperture of each objective are listed in Table I. Unless noted, all optical micrographs were taken under cross-polarized light. For a discussion of the interaction of polarized light with anisotropic crystals and spherulites; see references 165 to 168. A Leitz ortholux research microscope and 35mm Leica camera with light meter were used to photograph some of the blends after crystallization was complete.

Table I. Long Working Distance Objectives

Magnification	40	32	20	16	6.3
Numerical Aperture	0.65	0.30	0.57	0.17	0.12

The procedure for measuring spherulite growth rates depended on the concentration of PEO and the supercooling. At high PEO concentrations and large supercoolings, spherulite growth was rapid; a 16mm Bolex movie camera was used at 12 frames per second. For moderate and slow growth rates, intervalometers capable of photographic rates of from 1 frame per 60 hours to 1 frame per 10 seconds were used. A brief description of this equipment is given below. More detailed information may be found elsewhere.[169,170]

The apparatus for slow and moderate growth rate studies is shown in figure 12. The sample is transferred from an oven or hot plate at $100^{o}C \pm 5^{o}C$ into the Mettler heating chamber, (a). The microscope, (b), is focused and the intervalometer set for the appropriate time delay

between frames. After the time has elapsed, a 24-volt relay activates the shutter release and the motorized back, (c). A 110-volt relay synchronously lights the microscope lamp. When the shutter closes, the next frame of film is fed from a 200-foot film magazine, (e), into the Robot 35mm camera, (d).

Measurements at temperatures as low as $-15^{o}C \pm 0.05^{o}C$ were made by passing cold nitrogen gas from the liquid nitrogen dewar, (h), through the gas inlet on the hot stage chamber. A Sorvall LTC-2 low temperature controller kept the gas between 20 and 40 degrees colder at the sensing element, (i), than in the chamber itself. For fast crystallization rates, the sample was inserted into the hot stage with the microscope prefocused as much as possible. If the spherulites filled the microscope field in less than two minutes, a 16mm camera was used without the intervalometer.

Calibration of the Mettler hot stage against known temperature standards showed that the readout was consistently 1 degree below the melting temperature of the standards with ± 0.1 degree variation on extrapolation to zero heating rate. Figure 13 is a plot of readout temperature versus melting point of the birefringent standards. These standards were obtained from A. H. Thomas Company. At heating rates of $10^{o}C$/minute, the temperature of the readout was approximately $2.5 \pm 0.3^{o}C$ higher than the actual melting point.

Standard sample preparatory procedures[165,166] were adequate except at high supercoolings. Samples for high supercooling measurements were approximately .003 inch thick. These thin films were sandwiched between

two glass coverslips, melted, and glued to a thin wooden stick to enable movement of the specimen in the temperature chamber.

Prior to a series of experiments, micrographs of a 0.01mm stage micrometer were taken with each of the objective lenses to determine the exact magnification scale. Whenever an objective or ocular was changed, a micrograph of the calibration stage was taken. All of the optical micrographs in this thesis have 50-micron-bar overlays unless indicated. The calibration stage was also used to focus the camera by positioning it in the field; focusing with the binocular eyepiece; then adjusting the camera height so that the image of the micrometer lines were resolved on a ground glass plate at the back of the camera.

2. Scanning electron microscopy (SEM). After crystallization, the PEO/PMMA blends were examined in an ETEC autoscan scanning electron microscope. Because of the low atomic number of the atoms in these polymers, they were coated with gold, a high secondary electron scattering material, to improve resolution and prevent specimen charging. Chromium was also used as a coating material. Several recent reviews of SEM theory and experimental techniques have been written; see, for example, O. Wells[171] or S. Kimoto.[172]

Samples from the growth rate studies were divided into three pieces. One sample was only metal coated and served as a control. Another was etched in water for about five minutes to selectively extract the PEO. The remaining piece was treated in an ultrasonic bath to partially break down the blend superstructure. Selective solvent etching[142] and ultrasonic degradation[174] are well-known morphological preparative techniques.

All samples were coated with gold or chromium. If transmission replicas were to be made, chromium was deposited at a shadowing angle of five degrees; otherwise a rotary apparatus was used to eliminate the shadowing effect.[175] For SEM work, gold is the better coating because of its secondary electron emission characteristics. However, vacuum evaporated chromium has a much smaller particle size than gold and therefore better resolution in TEM.

3. Transmission electron microscopy (TEM). TEM examination of several blends was carried out on a Phillips EM-75. Preparation techniques[174,176] including ultramicrotoming, etching, and shadowing were used to study the blend morphologies. A Sorvall M-2B Porter-Blum ultramicrotome was used to cut 1000 - 500 Å thick (estimated by interference colors) sections. Because the blends are more dense than water, samples had to be microtomed without floating. Since the thin sections must be handled with tweezers and attached to the copper grids without the aid of the floating medium, samples are easily deformed and this technique proved very unsatisfactory.

Magnification for the TEM micrographs was calculated from a 17,500-line-per-inch carbon replica grating. Bar overlays on TEM micrographs represent 1 micron and on SEM micrographs 100 microns unless indicated.

4. Light scattering. Since small-angle light scattering, SALS, is not covered in Chapter I, a brief outline of theory and experimental procedures are given here. Several excellent reviews on the subject are available in the literature.[177-180] The mathematical model used to describe the scattering of light from solids depends on how the scatterers are characterized. Debye and Beuche[181] proposed a statistical

scattering theory for heterogeneous solids caused by refractive index fluctuations. The size of the fluctuation and the distance over which the variation in refractive index extends are defined by a correlation function. Goldstein and Mahalik[182] incorporated anisotropic fluctuations into this theory. A simplification of this theory by Stein, et al.[179,183] was made by modeling the anisotropic fluctuations as uniaxial rods or disks which can change their orientation. More sophisticated models can account for scattering patterns from ringed spherulites,[184] stretched polymers,[185] and other phenomena observed in crystalline polymers.[179,186]

There are two types of SALS patterns from which useful information on polymers can be obtained. In the H_v pattern the incident light is polarized vertically and the scattered light resolved on a horizontal analyzer. Since anisotropic aggregates will transmit light between crossed polaroids but isotropic aggregates (fluctuations) will not,[187] the H_v pattern will depend only on the nature of the anisotropic aggregate responsible for the scattering. If the anisotropic aggregate is a sphere, i.e., a reasonably good approximation of a polymer spherulite, the intensity of the H_v pattern is[185]

$$I_{H_v} = KV^2 \left\{ \left(\frac{3}{U^3} \right) \left(\alpha_t - \alpha_r \right) \cos(\theta/2) \sin\mu \cos\mu \cdot (4 \sin U - U \cos U - 3 \, Si \, U) \right\}^2 \qquad (58)$$

where $V = (4/3)\pi R^3$ is the volume of the sphere of radius R; α_t and α_r are the tangential and radial polarizabilities; and the term $\left(3/U^3\right)$ [sin U - U cos U] is the scattering function for spheres. The angles

θ and μ are defined in figure 14

$$U = 4\pi \left|\frac{R}{\lambda}\right| \sin(\theta/2) \tag{59}$$

$$\text{Si } U = \int_0^u \frac{\sin x}{x}\, dx$$

and K is a proportionality constant

$$K = \frac{16\pi \cos^2\theta}{c^4\lambda^4}$$

where c is the speed of light in vacuum, and λ is the wavelength of the scattered light (632.8 nm for the Spectral-Physics helium-neon laser used in these experiments).

The H_v pattern for spheres has a four-leaf clover appearance with intensity maxima at an azimuthal angle of 45^o such that

$$4.1 = \frac{4\pi R}{\lambda} \sin\left|\frac{\theta_{max}}{2}\right| \tag{60}$$

The intensity of an H_v pattern for a thin anisotropic rod lying in a plane perpendicular to the incident beam is given by[188]

$$I_{H_v}(\alpha) = K'L\left\{\left[\sin(kaL/2) \,/\, (kaL/2)\right] \cdot \sin\alpha'\cos\alpha'\right\}^2 \tag{61}$$

where L is the length of the rod; α is the angle of tilt relative to the vertical; k is $2\pi/\lambda$; and a is given by

$$a = -\sin(\alpha + \mu)\sin\theta$$

Here α′ is α + ω where ω is the angle between the rod long axis and the optic axis. In rod H_v patterns the intensity of the light decreases

with increasing scattering angle θ from the center of the pattern along the 45^{o} azimuthal angle μ. Unlike sphere scattering patterns, the intensity along the 45^{o} direction does not have a maximum except at the center of the pattern. The insert in figure 19b is an example of this type of pattern. It is not possible to obtain L from a cursory examination of the H_v pattern of rod-like scatterers.

Clearly, quite different H_v patterns are obtained from rod-like scatterers as compared to spherical scatters. Misra et al.,[189] have correlated the early stages of spherulite growth in poly(ethylene terephthalate) with SALS patterns and have found that the initial Zweiblatten spherulite precursors scatter as rods; but after a certain time, a maximum in the 45^{o} intensity occurs indicating that the spherulite structure is complete. In other words, during the early stages of spherulite growth, the H_v scattering pattern intensity decreases monotonically from the center along a 45^{o} angle to the polars. This is characteristic of rod-like scatterers. At longer times, the intensity along this 45^{o} angle goes through a maximum. The position of the maximum is related to the spherulite radius by equation (60).

Interference between spherulites produces speckling in the H_v patterns.[190] This effect was observed in the nonimpinging spherulite morphology discussed in the next chapter.

The other type of SALS pattern, the V_v pattern, is formed if the plane of vibration of the polarizer and the analyzer are vertical. The intensity of the V_v pattern for spherical scatterers is given by

$$I_{V_v} = KU^2 \left\{ \left(\frac{3}{U^3} \right) \left(\alpha_t - \alpha_s \right) \left(2 \sin U - U\cos U - \mathrm{Si}U \right) \right.$$

$$+ \left(\alpha_r - \alpha_s \right) \left(\mathrm{Si}U - \sin U \right) + \left(\alpha_t - \alpha_r \right) \cos^2 \left(\frac{\theta}{2} \right) \qquad (62)$$

$$\left. \cdot \cos^2 \mu \left(4 \sin U - U\cos U - 3\, \mathrm{Si}U \right) \right\}^2$$

Unlike the H_v pattern, the V_v pattern depends on both anisotropic and isotropic refractive index fluctuations, i.e., on the size and shape of the scattering particle and also on the polarizability of the surrounding matrix, α_s. According to Samuels,[191] the first and second terms in equation (62) have almost spherical symmetry at low angles. The third term, containing the azimuthal dependence, is the major contributor to the V_v pattern's anisotropy.

Samuels has shown that even though the terms containing the surround polarizability are nearly symmetrical, there is a marked effect on the V_v pattern as the surround refractive index is varied. For positive spherulites ($\alpha_r > \alpha_t$) if the polarizability of the surround is lower than the tangential polarizability, the maximum intensity is in the central elliptical region with outer lobes of weaker intensity. As α_s approaches α_t, the intensity and size of the central lobe decreases while the upper lobe intensity remains fairly constant. As the refractive index of the surround becomes larger than the largest refractive index of the crystal, the central lobe diminishes in size and intensity until the upper lobes are now more intense. The upper lobes do not actually increase in intensity, but the drastic reduction of the two symmetric terms in equation (62) causes this effect.

Few SALS studies of blends have been published; none deal with an in-depth analysis of the V_v patterns. Stein[180] has reviewed the optical behavior of blends recently but cites only two references where SALS was used to analyze compatible, crystalline blends. Variation of the H_v pattern with crystalline component concentration in the poly(vinyl chloride) - poly (caprolactone) system[192] showed an increase in the spherulite size with small increase in noncrystalline, poly(vinyl chloride) concentration and then a decrease with further increase in PVC concentration. The very complex poly(butylene terephthalate) - poly(ethylene terephthalate) system lends itself nicely to SALS studies since the optic axis is oriented differently in the two crystalline polymers.[193] Clearly SALS could be a very useful technique for studying crystallization phenomena in polyblends.

D. Differential Scanning Calorimetry

Differential scanning calorimetry (DSC) is a very useful technique for characterizing crystalline and amorphous polymers. Unfortunately, analysis of DSC traces differs from author to author.[194-198] All thermal measurements in this research were run on a Perkin-Elmer DSC-2, and the results were analyzed as suggested by the manufacturer.[199] The temperature range from -100^{o}C to 190^{o}C was examined using liquid nitrogen to cool to the low temperature and helium as a purge gas. When thermal measurements above ambient temperature were made, nitrogen was used as the purge gas.

The crystal-crystal and melting transitions of high purity cyclohexane, benzoic acid, and indium were used to calibrate the instrument temperature scale.[199] With the exception of several early runs, temperature observed on the digital readout corresponded to within 0.5^{o} at 10^{o} per minute heating rate over the entire temperature range. The earlier runs were fitted at three points to the standard transitions using quadratic Laguerre polynomials.[155] The variation in the readout temperature with heating rate may be calculated from

$$T_A - T_{obs} = - C \frac{dT}{dt} + D \qquad (63)$$

where T_A is the actual transition temperature of the standard; T_{obs} is the DSC readout temperature; dT/dt is the heating rate; and C and D are constants which varied between 0.25 - 0.069 and 1.0 - 1.39, respectively, from day to day. The transition temperatures and enthalpies of the standards are listed in Table II.

Table II. DSC Calibration Standards.

Standard	Type Transition	Temperature, ^{o}K	ΔH_f, Cal/gr.
Indium	Melt	$433.9^{o}K$	6.79 cal./gr.
Benzoic Acid	Melt	$395^{o}K$	33.9 cal./gr.
Cyclohexane	Melt	$279.7^{o}K$	7.47 cal./gr.
	Crystal-crystal	$186.1^{o}K$	19.02 cal./gr.

Transition temperatures for the standards and PEO were determined by the method of Barrall and Johnson.[200] They claim that for high purity standards, the melting point is the intersection of the recorder slope with the instrument baseline. The PEO/PMMA mixture melting points from

samples annealed 2 to 8 weeks at 45°C were measured in this manner. This approach is similar to that described by Flynn.[201] The glass transition temperature was taken as the intersection of the recorder slope with the instrument baseline, which is almost equivalent to the more complicated method of Guttman, et al.[202]

Enthalpy measurements can be made if the instrument constant is known. The instrument constant, K, is calculated by integration of a melting endotherm of a standard of known enthalpy of fusion, ΔH_f, from[196,199,201]

$$K = \frac{\Delta H_f \, w_s}{A_s r_s} \tag{64}$$

where w_s is the weight of the standard; A_s is the area under the melting endotherm; and r_s is the sensitivity setting or measurement range of the instrument. Knowing the instrument constant, equation (64) can be rearranged to give the enthalpy of melting of PEO from the area under its endotherm. Since the enthalpy of fusion of perfectly (100 percent) crystalline PEO is known,[203-205] the degree of crystallinity of the blend is

$$X_c \text{ (Blend)} = \frac{H_t - H_a}{H_c - H_a} = \frac{\Delta H_m}{\Delta H_f(\text{PEO})} = \frac{A_p r_p}{W_p \Delta H_f(\text{PEO}) K} \tag{65}$$

where H_a, H_c, and H_t are the enthalpies of amorphous, perfectly crystalline, and partially crystalline PEO. The subscript p refers to the blend. The fraction of PEO which is crystalline, X_c(PEO) is

$$X_c(\text{PEO}) = X_c(\text{Blend})/W(\text{PEO}) \tag{66}$$

where W(PEO) is the weight fraction of PEO in the blend.

1. Isothermal crystallization. Measurements of crystallization exotherms at different supercoolings were made by holding the temperature of the sample between 100°C and 130°C for not less than five minutes and then quenching at 320°C/minute to the desired crystallization temperature, T_x. This temperature was maintained until the crystallization exotherm was complete, i.e., until the instrument pen returned to the isothermal baseline and no further heat evolution could be detected. After the crystallization exotherm was completed, the polymer was remelted and crystallized at another T_x. As many as nine successive isotherms were run without significant variation. In fact, more variation was observed from sample to sample than on the same sample in agreement with the microscopic results.

E. Dynamic Mechanical Properties

1. Principles of operation. By definition, Young's modulus is

$$E = \frac{\sigma}{\varepsilon} = \frac{F/A}{\Delta L/L} \tag{67}$$

where σ is the tensile stress or force, F, applied, in this case to a rectangular parallopiped along the Z axis (as shown in figure 15a) per unit area, A; and ε is the strain or change in length, ΔL, divided by the length, L.

In the Rheovibron D.D.V.II, a displacement transducer oscillates at a given frequency driving one of the metal arms which holds the sample

in a reciprocating motion through a small distance, ΔL. In a linear isotropic polymer, this produces a small sinusoidal tensile strain, ε^*. This oscillating strain is transmitted through the polymer to the other arm of the instrument, which is attached to a stress transducer. The oscillating stress, σ^*, measured as a result of the applied strain is slightly out of phase.[206-210] This is expressed mathematically as

$$\sigma^* = \sigma_o \exp i(\omega t + \delta) \tag{68}$$

$$\varepsilon^* = \varepsilon_o \exp i\omega t \tag{69}$$

Defining the complex modulus by analogy to equation (67),

$$E^* = \frac{\sigma^*}{\varepsilon^*} = \frac{\sigma_o}{\varepsilon_o} e^{i\delta} \tag{70}$$

Since any complex number may be written in terms of its real and imaginary parts,

$$E^* = E' + iE'' = \frac{\sigma_o}{\varepsilon_o} \cos \delta + i \frac{\sigma_o}{\varepsilon_o} \sin \delta \tag{71}$$

where E' is the tensile storage modulus and E'' is the tensile loss modulus. The complex compliance is given by[211] $D^* = 1/E^*$.

Various phenomenological[212,213] and molecular[214-217] models have been proposed to describe relaxations in polymers. Vibron measurements give the complex tensile modulus defined in equation (70) as a function of temperature. The absolute value of E^* was calculated from[214]

$$|E^*| = \left(2 \times 10^9 \text{ dynes/cm}^2\right) \frac{(L + \alpha)}{ADS} \tag{72}$$

where S is the amplitude factor; A is the cross sectional area of the specimen; D is the dynamic force; and $(L + \alpha)$ is the total length of the sample between the specimen grips. The value α is the change in length associated with thermal expansion of the polymer as the temperature increases and is obtained from a micrometer attached to one arm of the sample. The factor 2×10^9 contains the small sinusoidal length variation and other conversion factors so that the modulus has units of dynes per square centimeter. The average tensile strain on a specimen was about 0.2 percent.

Samples for dynamic mechanical measurements were either cast or pressed to between 3 and 4 mils thick and stored under vacuum at $80^{o}C$ for several days before being transferred to the Vibron. The machine was cooled as rapidly as possible to $-160^{o}C$ or lower to prevent or reduce the crystallinity in the samples; then the sample was allowed to warm up slowly as modulus measurements were made. Consecutive measurements at 110, 11, and 3.5 Hertz were made every 3 to 5 degrees. With the Lissajous' figure properly adjusted, the dynamic force, tan δ, temperature, change in length, and amplification factor were recorded. The data were transcribed onto computer cards and analyzed using the program listed in Appendix I.

2. Dynamic mechanical properties of blends. A short discussion of mechanical relaxations is in order. For a polymer with a single relaxation time, it can easily be shown[213,220] that

$$E'(T) = E_R + \frac{(E_u - E_R)\exp\left[\frac{-2C_1(T - T_g)}{C_2 + T - T_g}\right]}{1 + \exp\left[\frac{-2C_1(T - T_g)}{C_2 + T - T_g}\right]} \tag{73}$$

$$E''(T) = \frac{(E_u - E_R)\exp\left[-C_1(T - T_g)/(C_2 + T - T_g)\right]}{1 + \exp\left[\frac{-2C_1(T - T_g)}{C_2 + T - T_g}\right]} \tag{74}$$

where E_R is the modulus of the relaxed polymer; E_u is the modulus of the unrelaxed polymer; and C_1 and C_2 are the WLF constants 17.4 and 51.6, respectively. Here, of course, it has been assumed that the relaxations are glass transitions with WLF temperature dependence

$$\log a_T = \log(\tau/\tau_o) = \frac{-C_1(T - T_g)}{C_2 + T - T_g} \tag{75}$$

and that the frequency remains constant (for convenience it is chosen as $\omega = 1/\tau_o$).

For a compatible blend of two amorphous polymers with T_g's of 200^oK and 380^oK respectively, equations (73) and (74) were used to show the effect of blend composition on the dynamic mechanical properties. Assuming $E_u = 10^{10}$ and $E_R = 10^7$ dynes/cm^2 and allowing the T_g of the blend to vary according to Fox's equation[221] (equation 44 in Chapter I) results in modulus-temperature curves that change with blend composition as shown in figure 16a. Note that the loss modulus is skewed slightly, which is not the case for E'' versus ω.[213] Also there is only one

inflection point in the storage modulus of any given curve. The tan delta curves have been omitted for clarity but would reach a maximum slightly to the higher temperature side of the E'' maximum. This would be the behavior expected for a compatible blend of PEO and PMMA with glass transitions T_{g_1} ($206^{o}K$) and T_{g_2} ($377^{o}K$) as the blend composition is changed if no crystallinity or secondary relaxations complicate the mechanical spectrum.

For incompatible polymer blends, two polymer phases exist, each with its own relaxation time or glass transition.[222] Pakula, et al.[223] have applied Takayangi's models[224,225] for crystalline polymers to incompatible blends. The complex modulus for a two-component system, according to Pakula, can be described by the series model in figure 15b or the parallel model in figure 15c. The equations describing the models are

$$E^*_{series} = \left\{ \frac{\phi}{(1 - \lambda)\, E^*_1 + \lambda E^*_2} + \frac{1 - \phi}{E^*_1} \right\}^{-1} \tag{76}$$

$$E^*_{parallel} = \lambda \left\{ \frac{\phi}{E^*_1} + \frac{1 - \phi}{E^*_2} \right\}^{-1} + (1 - \lambda)\, E^*_1 \tag{77}$$

where ϕ is the fraction of series interaction of the second component, and λ is the fraction of parallel interaction of the second component. Notice that if ϕ goes to one, the series model moduli are additive whereas the parallel model becomes independent of the second component.

In the incompatible blend, the glass transition of the two phases do not shift in temperature; only the magnitude of the relaxation strength changes as the blend composition changes. The relaxation strength of a

transition is defined as $(E_u - E_r)/E_r$. By separating E* into its real and imaginary parts and taking the limit as the loss terms go to zero, equations for the storage modulus E´ for Takayanagi's models are obtained. These turn out to be the same as equations (76) and (77) except that E* is replaced by E´. Substituting E´ for E* in the series and parallel models should give a reasonably accurate representation of the storage modulus at temperatures more than twenty degrees from the glass transition. Assuming E_u and E_R of the pure incompatible polymers are the same (10^{10} dynes/cm^2 and 10^7 dynes/cm^2 respectively) and using the T_g values of 200^{o}K and 380^{o}K, figure 16b shows log E´ versus temperature plots for the series model with ϕ and λ equal to the weight fraction of the low T_g polymer (solid lines) and high T_g polymer (dotted lines). Even at 75 percent low T_g polymer, if E_1' is the high T_g polymer (solid lines), a very weak low temperature transition occurs. Thus assuming this model it is possible to incorrectly identify a polymer blend as compatible when the scatter in the dynamic mechanical data exceeds the relaxation strength of the low temperature transition.

For a compatible blend in which one of the components will crystallize below its melting temperature without incorporation of the second polymer in the crystal, Takayanagi's models should apply. Note that now the amorphous component will have a glass transition temperature which depends on the concentration of crystallizable polymer remaining in the melt. Using DSC data from figures 25 and 43 to determine the percent crystallinity of the crystalline component and assuming E_1' (the crystalline modulus) to be 10^{10} below T_m and 10^7 dynes/cm^2 above T_m, figure 17

was calculated. The amorphous blend glass transition temperature $T_g(a)$ depends on the percent of amorphous crystallizable polymer (PEO), which is $X_a = 1 - X_c$, and the weight fraction of PMMA. The weight fraction of PEO in the amorphous region Φ (PEO) is

$$\Phi \text{ (PEO)} = X_a \text{ W (PEO)} / \left(X_a \text{ W (PEO)} + \text{W (PMMA)} \right) \qquad (78)$$

where W(i) is the weight fraction of species i. The weight fraction of the PMMA in the amorphous phase is 1 - Φ (PEO). The T_g of the amorphous phase can be estimated from the Fox equation (equation 44 in Chapter I) with the weight fractions of amorphous material Φ substituted for the weight fractions of the blend.

The storage modulus depends on T_{ga}, the glass transition of the amorphous phase in the blend, and the melting temperature of the crystallites (taken as 320^{o}K for PEO). If the glass temperature is less than the melting temperature, the storage modulus behaves as an incompatible mixture of crystal and amorphous homopolymers, except that the glass transition increases with increasing crystallinity (assuming the glass temperature of the amorphous polymer, PMMA, is higher than the crystalline polymer). If the crystallinity decreases, the glass transition can actually decrease as more high-glass-transition-temperature polymer is added. The glass transition of the amorphous phase is higher for the 60 percent PEO than for the 40 percent PEO blend because of the higher degree of crystallinity in the 60/40:PEO/PMMA blend. However, the total concentration of the amorphous phase is greater in the 40/60:PEO/PMMA blend. The amount of amorphous material controls the relaxation strength

of the glass transition but the transition temperature is controlled by the composition of the amorphous phase. Thus in figure 17, the 40/60:PEO/PMMA blend has a larger relaxation strength and lower glass transition than the 60/40:PEO/PMMA blend.

When the degree of crystallinity varies with crystallizing temperature or annealing in blends with a low PEO concentration, the glass transition of the amorphous phase can shift over a $35^{o}C$ temperature range. This is shown in figure 17 by the horizontal arrows between $35^{o}C$ and $70^{o}C$ for the 30/70:PEO/PMMA blend. The T_g of the amorphous phase changes by this extreme if the degree of crystallinity varies from 0 to 0.5. No attempt was made to account for recrystallization effects, the influence of the fold surface, phase inversion effects, or effects of secondary relaxations on the dynamic mechanical properties of blends with a highly crystalline component which can be complex and difficult to interpret unambiguously.

CHAPTER III

RESULTS AND CONCLUSIONS

This chapter discusses (1) the morphology of PEO/PMMA mixtures, (2) the effect of amorphous PMMA on the crystallization behavior of PEO, and (3) evidence for intimate mixing of PEO/PMMA at temperatures above the crystallization temperature of PEO. The chapter also addresses some unsolved problems and suggests future work on crystallizable blends.

A. Morphology

The morphology of compatible blends of a crystallizable polymer having a low glass transition temperature and an amorphous polymer having a high glass transition temperature is controlled by the degree of supercooling and the glass transition temperature of the blend. At a high concentration of crystallizable polymer, the number of primary nuclei is suppressed and larger spherulites form than in the pure polymer. At intermediate concentrations of crystalline polymer, primary nucleation is apparently enhanced by the excess amorphous material in the blend. As the blend glass transition temperature approaches the melting temperature, crystallization proceeds very slowly. If the glass temperature exceeds the melting point, the blend will not crystallize.

Poly(caprolactone)/poly(vinyl chloride)[192,226] and poly(vinylidene flouride)/PMMA[73,77] are examples of blends which exhibit this type of morphology. Poly(2,6 dimethylphenylene oxide)/atatic polystyrene,[277]

however, is completely amorphous unless exposed to small amounts of solvent vapor. But if isotactic polystyrene is mixed with poly(2,6 dimethylphenylene oxide), crystallization behavior is similar to that of other blends in which the second component is amorphous and has a high glass transition temperature.

In blends of an atactic polymer and a crystalline polymer having the same repeat unit, spherulites will grow even at a very high (90%) amorphous concentration.[85,90,142] The concentration of the crystalline component changes the growth rate but not the glass transition. Morphological information about blends of two crystallizable polymers is limited and more difficult to rationalize.[193]

In the present study, four morphologies of PEO/PMMA blends occur, depending on the concentration of PEO. At very low PEO concentrations, the glass transition is higher than the melting point, and no crystallinity is observed. At slightly higher PEO concentrations, non-impinging spherulites are found. If the concentration of crystalline and amorphous polymers is nearly equal, rod-like crystals resembling the early stages of spherulite growth are observed. About 60 percent PEO, the morphology is spherulitic, which is characteristic of pure polymer.

Studies of the morphology of forcibly mixed, noncrystalline and crystalline, incompatible blends[228,229] showed distinct phases of the crystalline component in a spherulite morphology surrounded by an amorphous phase. With an increasing concentration of amorphous component, the crystalline domains become smaller, but little or no intermixing between the two phases was observed.

1. Glassy blends - low PEO concentration. At PEO concentrations between zero and twenty percent by weight, mixtures of PEO/PMMA are noncrystalline glasses. Figure 18 contains transmission and scanning electron micrographs of 18 percent PEO blends. These samples were etched by soaking in water for about 30 seconds to remove the PEO, dried, metal shadowed, and scanned. Soaking caused the bulk material to become cloudy, but this etching was necessary, since unetched specimens showed only the parallel knife marks of the ultramicrotome or the blistering phenomena in the upper left hand corner of the scanning micrograph (figure 18b).

The pits and bumps in figure 18a are the result of water etching away the PEO accompanied by some swelling of the mixture. They vary in size from 300 to about 1500Å and are probably the reason for the turbidity of the etched samples. The large circular structures visible in the transmission micrograph are suspected to be PEO residue left after the water evaporated. These 18 percent PEO samples were considerably more flexible than pure PMMA and microtomed quite easily.

2. Blends with low crystallinity: non-impinging spherulites. At PEO concentrations between 20 and 40 percent, non-impinging spherulites (figures 18c and 18d) were present in the samples made from polymerized solutions of low molecular weight Carbowax 6000 and MMA monomer. Because of the lower crystallinity of high molecular weight polymers resulting from entanglements, the WSR-N-3000 mixtures crystallize only at PEO concentrations above 30 percent. The non-impinging morphology was enhanced by the viscosity lowering effect of trapped monomer and

lower molecular weight PMMA in the polymerized samples as compared to the solvent cast samples.

Unetched, ultramicrotomed specimens taken from these samples did not show spherulites in the TEM. Etching thin samples tends to shrivel and dissolve large portions of the film, making micrography difficult. Unfortunately, microtoming the sample destroys its surface structure. Without a surface structure, the shadowing technique provides no variation in specimen contrast. Since the electron density difference between the two components is small, transmission micrographs taken without etching or staining have very poor resolution. The birefringent spherulites in the thin sections are visible under a polarizing microscope, but not in the TEM (see figure 18d).

If these blends are intimately mixed prior to crystallization, then to form spherulites at this low concentration the PEO must travel a considerable distance on the molecular scale. Since the refractive indices of the two components are different (r.i. of PEO = 1.4563 at 30^{o}C and r.i. of PMMA = 1.490 at 20^{o}C),[230] as the PEO crystallizes the refractive index of the surround between two spherulites should increase because the low refractive index PEO is being withdrawn. If there are surface or refractive index fluctuations in the sample,[231] interference fringes can be observed with a Nemarski interference microscope. An interference micrograph of a thin section of 33 percent PEO with non-impinging spherulites is shown in figure 18e. The black fringes, although difficult to see in the reproduction, indicate either that to reach the crystal PEO has traveled through the amorphous blend almost

20μ, or that there is a very uniform thickness change surrounding the spherulite. If these interference rings are caused by refractive index changes in the amorphous phase, this would imply that some PEO has migrated a remarkable distance. If the mixtures are two-phased prior to crystallization, no refractive index variation would be expected except in a narrow interfacial region less than 0.1 micron. This is strong morphological evidence for melt compatibility at this composition.

3. Intermediate compositions: rod-like crystallites. At nearly equal concentrations of PEO and PMMA, i.e., between 40 and 60 percent, rod-like crystallites are present. This morphology, shown in crossed polar optical and SEM micrographs of 40/60:WSR/HM blends in figures 19a and 19b, is characteristic of the early stages of spherulite growth. The small angle light scattering pattern inserted in the lower right corner of the optical micrograph is consistent with this interpretation.[188,189]

It is evident from the SEM micrographs that the impressions left after extraction of the PEO are deeper in the center but have definite impingement boundaries. If the spherulite had crystallized from a two-phase liquid, holes from which PEO had been extracted would be found without the spherulites traversing the second phase and impinging. The large number of nuclei at these intermediate concentrations is probably the result of interference of the PMMA with PEO crystallization. The PMMA might both prevent advancement of a growing crystal and act as a nucleating agent to induce new crystal formation.

When these crystalline blends were remelted within a few days after crystallization or cycled through the crystallization and melting process

several times, the melt remained optically homogeneous. (A sealed sample of 50/50:WSR/H$\overline{M}$ was held at 30°C until crystallization was apparently complete, then heated in the Mettler at 10°C/min. to 120°C for five cycles. The melt was transparent on each cycle.) However, when crystals that had been annealed for several weeks were melted, the melting point increased several degrees; further, as long as the temperature was held below about 110°C, regions of different refractive index were observed in the melt. When the temperature of the mixture was raised above the PMMA glass transition, the two phases coalesced rapidly until only a vague outline of the surface remained. After coalescence, if the mixture were cooled to a temperature slightly above the melting temperature and held there for several hours, no evidence of phase separation occurred as long as the mixture was kept dry. The mixture can be crystallized and remelted as before without phase separation in the melt unless it is annealed for several days. During secondary crystallization, accreation of the PEO from the melt apparently continues, but at a much slower rate.

Figure 19c is an optical micrograph of an annealed, 50/50 blend of WSR-N-3000 PEO and PMMA under crossed polars at room temperature. This sample was heated at 10°C/min. After melting, photographs were taken at 10°C intervals under oblique illumination to enhance the optical effects of the refractive index difference. Coalescence of the two polymer phases can be seen in figures 19d through 19k. Coalescence indicated that at this composition the PEO was compatible with PMMA above the crystallization temperature.

Above the melting temperature blends between 40 and 60 percent PEO

were more sensitive to degradation and moisture than blends of lower or higher PEO concentration. Howard[165] showed that PEO degrades badly above 80°C in the presence of acidic fillers. After more than 3 months under vacuum at this temperature, the mixtures degraded to low molecular weight oils. At 80°C or above, moisture in the air also causes blends in this composition range to degrade and phase separate. PEO will absorb 3 to 5 percent water from the air,[173] and catalytic amounts of water could cause a water-ester hydrolysis reaction in PMMA

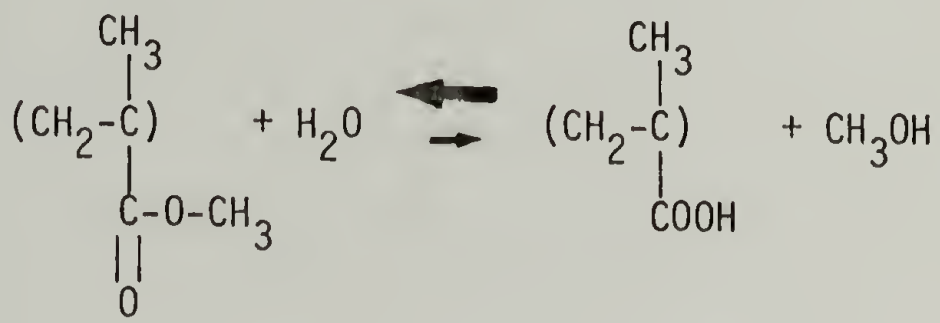

generating the acidic groups responsible for degradation of the PEO.

Another reason for the enhanced sensitivity to degradation and moisture of the liquid 40 to 60 percent PEO blends is that these compositions are less thermodynamically stable to changes in the interaction parameter of the mixture than blends of higher or lower PEO content. As the PEO degrades the hydroxyl concentration increases changing the interaction parameter. If small amounts of water selectively solvate the PEO chains changing the interaction parameter, the 40 to 60 percent PEO compositions would be the compositions which first showed phase separation. When the mixture has crystallized, the composition of the amorphous phase must increase in PMMA. Crystalline and annealed blends in this composition range are much less sensitive to degradation and

moisture. Blends exposed to temperatures above the melting point of PEO were kept under nitrogen or vacuum to minimize degradation. No further attempt to understand the degradation mechanism was made.

4. Spherulitic blends: high PEO concentration. Compositions in which the percentage of PEO was 60 or higher had the typical spherulite morphology of pure PEO. To describe the effect of PMMA on the PEO spherulites, Keith and Padden's[89] terminology will be used. According to these authors, the compactness of a spherulite refers to both the coarseness of the crystalline fibers, i.e., the distance from one fiber to the next, and the frequency of branching. At any stage of growth the compactness of a spherulite is determined by material inside the spherulite boundary, including crystalline and uncrystallized interfibrillar polymer. The compactness is a function of the molecular weight of both species, the concentration of diluent, and the degree of supercooling. With increasing supercooling, branching increases but fiber thickness decreases; thus the effect of diluent on spherulite compactness should be measured at the same supercooling.

As PMMA is added to PEO, the compactness of the PEO spherulites increases and then decreases at constant supercooling. At constant blend composition with increasing supercooling, both spherulite size and compactness decrease. Figures 20 through 23 are SEM and optical micrographs which show this behavior quite clearly.

Figure 20 contains six SEM micrographs of pure PEO (WSR-N-3000) that had been supercooled to various degrees. As ΔT increases, (1) the spherulite size decreases; (2) the coarseness of the spherulite increases; and

(3) the fibril branching increases. Although the thickness of the lamellar fibrils decreased with supercooling,[111] the increase in branching with supercooling produced spherulites with open texture. In other words, as the supercooling increases, the distance between the main radial fibers increases even though the fine structure increases because of the increased branching. In polymer single crystals, this increase in small angle branching with supercooling has been called dendritic behavior.[135,232] There is also considerable void formation during crystallization. Because of the volume contraction, pure PEO spherulites crack at the center (as in figure 20e), parallel to the radial fibers (as in figures 20a and f), and along the boundaries (as in figure 20c).

A comparison of the pure PEO and a 90/10 mixture in figures 20 and 21 revealed that in the blend (1) the spherulite size at the same supercooling increased slightly; (2) the surface texture was concealed, and (3) the voids have been eliminated except at the spherulite boundaries. Clearly, the PMMA was incorporated in the interlamellar regions. The PMMA has filled the voids and leveled out the spaces between the radiating fibers, making the texture almost impossible to evaluate from SEM micrographs. The spherulites appear more compact even though there is more amorphous intersticial material because of the removal of the voids and surface structure. Table I lists the average spherulite size as a function of composition and temperature.

Table I. SALS and optical microscopic measurements of spherulite size as a function of temperature and blend composition. Spherulite radius in mm.

[PEO] \ T°C	45	40	35	30	25	20	15
100	6.6	3.65±.5	1.9±.4		0.61	0.32±.1	0.24±.04
90	6.75	3.9±.5	1.9±.5	2.2±.4	0.10±.05	0.14±.04	0.13±.06
80		3.35	1.0±.2	0.78±.1	0.14±.05	0.093±.03	0.074*
70		1.17±.1	0.51±.03		0.12±.02	0.051*	0.067±.07
60		0.24*	0.20*	0.13*	0.10*		0.057±.05

*measured from SALS H_v maximum.

The change in spherulite morphology with increasing PMMA in figures 21 through 24 was similar to that found in other blends of one crystalline and one amorphous polymer.[85,90,192] As the PMMA concentration increased from 10 and 40 percent (1) the spherulite size at the same supercooling decreased; (2) the spherulite texture became more open and coarse; and (3) the interlamellar spacing increased.

Table II lists the apparent lamella thicknesses at various PMMA concentrations and supercoolings as measured from SEM micrographs at high magnification. At the same supercooling, the lamella thickness increases with increasing PMMA. The values from the SEM measurements were considerably larger than would be expected on the basis of single crystal lamella thickness. Larger values are attributed to the limit of resolution of the instrument (100Å), multiple layered crystals, and the angle

at which the stacks of lamellae are viewed. When the lamella thickness is near the resolution of the instrument, the SEM could resolve only a fiber composed of several lamellae since the intersticies would be smaller than the crystal and not resolvable. If several lamellae are stacked in close register but terraced, the actual thickness could be determined only when the stack is viewed end on. Also, at high magnification the electron beam causes severe degradation, crosslinking, and deformation of the crystal. For the above reasons the lamellar thickness measurements were only approximate. Even so, for a given crystallization temperature, the distance between resolvable fibers increases in direct proportion to the amount of PMMA in the blend.

Table II. Apparent variation of interlamellar spacing with temperature and blend composition. The spacings are listed as S X 10^3 Å.

[PEO] \ T^oC	30	25	20	15
90	1.72±0.2			
80	2.49±0.3		1.31	1.19
70	3.77±0.4	1.82±0.3	1.42	0.98±0.1
60	5.0	2.37		1.65±0.2

Data from small angle light scattering, optical micrographs and SEM measurements on blends of PEO/PMMA lead to the following conclusions: (1) at low concentrations of PMMA (10 percent or less), the largest PEO spherulites were formed; (2) at 20 percent PMMA or higher, the spherulite

radius decreased with increasing PMMA until crystal growth ceased; (3) at between 40 and 60 percent PMMA, the spherulite radii were difficult to measure because of the small crystallite size and poorly defined boundaries; (4) at between 60 and 80 percent PMMA, non-impinging spherulites grew. No crystallites would grow above 80 percent PMMA.

The explanation for this morphological behavior is that these two polymers are compatible in the melt. This being the case, at 20 percent or less PEO, the glass transition temperature is higher than the melting temperature and no crystals will grow. Between 20 and 40 percent PEO, only a small portion of the PEO can be crystallized (at most 25 percent) before the glass transition of the amorphous material exceeds the melting point. Thus as the crystal grows and crystallizable PEO is extracted from the melt, the viscosity of the melt rises rapidly choking off the influx of crystallizable polymer from the surround which produces non-impinging spherulites.

The morphology above 40 percent PEO is controlled by nucleation and growth rates. Between 40 and 60 percent PEO the concentration of the noncrystallizable component (PMMA) is sufficiently high that the growth rates are very slow. Because it will not crystallize and is not mobile, the PMMA interferes with crystallization. Although heterogeneous nucleation in PEO is not well-understood,[170] if PMMA acts as a substrate with a different surface free energy than other heterogeneities in the melt, coherent or time dependent heterogeneous nucleation would increase the number of nuclei formed. When the number of nuclei is large, the sizes of the spherulites will be smaller. The effect of the PMMA then

is to nucleate many spherulites but not allow them to grow. This produces the rod-like crystallites found in this composition range.

Above 60 percent PEO, the glass transition temperature is much lower than the melting temperature, and sufficient concentrations of PEO are available to allow spherulites to grow to completion. The reason for the formation of larger PEO spherulites in a 10-percent PMMA mixture than in pure PEO is not clear. At low concentrations PMMA might preferentially adsorb onto heterogeneities in the melt making them less attractive nucleating agents. The larger spherulites in the 90/10 blend could be due to the combined effects of PMMA on nucleation, growth, and the relief of stress caused by the presence of extra amorphous material during the volume change on crystallization.

B. Crystallization of PEO/PMMA Blends

Studies of the degree of crystallinity, melting, and growth rates elucidated the influence of a high molecular weight diluent on the crystallization of PEO. When PMMA diluted the PEO, the change in melt viscosity as a result of increasing T_g was the main factor which determined the crystallization behavior of the blends. Both optical and calorimetric growth rate measurements showed decreasing crystallization rates with increasing PMMA concentration. Little effect on the interfacial surface free energies or melting point of the PEO spherulites was found. This is consistent with a very small interaction parameter

and mixing entropy for the PEO/PMMA blends. The half-time of isothermal overall crystallization, which depended on the spherulite growth rate, also shifted to longer times with increasing PMMA content. These data supported the contention that above the crystallization temperature the PEO/PMMA blends were homogeneous, i.e., the two polymers were intimately mixed or compatible in the melt.

1. The degree of crystallinity and melting behavior in PEO/PMMA blends. As the concentration of PMMA increased in these blends, the degree of crystallinity of the PEO decreased. Similar results[192,227,259] have been observed for other compatible blends in which the amorphous component had the higher glass transition. Because the degree of crystallinity depended[56,58] on the crystallization temperature and crystallite perfection as well as blend composition, the blends were annealed at 45°C for a month or more before determining the degree of crystallinity. Lamellar thickening[260] and secondary crystallization occuring during the annealing process increased the crystallite perfection. These annealed PEO spherulite crystals had a higher melting point than unannealed crystals.

Figure 25 is a plot of the percent crystallinity of PEO as a function of the weight fraction of PEO in annealed blends. Equation (65) from Chapter II, which assumes the usual two-phase model,[261] was used to calculate the percentage of crystallinity from first scans of annealed blends on the DSC. Subsequent DSC traces indicated lower crystallinity and melting points, as expected for unannealed samples. Up to 70 percent PEO, the degree of crystallinity of the PEO in annealed blends was almost

independent of the PMMA content. From 40 to 70 percent PEO, the crystallinity of the PEO in the blend increased very rapidly. Below 40 percent PEO, less than 10 percent of the total PEO concentration in the blend was crystalline, and below 20 percent PEO, no crystallinity was observed. No crystallinity would be expected for compatible blends having T_g equal to T_m. For 20/80: PEO/PMMA blends, the T_g calculated from equation (44) was 50^oC, which is about the melting temperature of the quenched blends. The lack of crystallinity indicated by DSC measurements is in agreement with the lack of birefringent crystals in the optical morphology studies in Section A of this chapter.

The melting points of annealed blends were all the same ($63^oC \pm 0.5^oC$), independent of the blend composition (figure 26). This implied that the Flory-Huggins interaction parameter must be small.[75,76] Annealed samples always had higher melting points by from 2^oC to 15^oC on the first DSC scan than on subsequent scans or scans of unannealed samples. The difference between the melting point of annealed blends and unannealed blends depended on the blend composition and thermal history.

A plot of T_m versus composition (figure 26) is similar to a phase diagram[262] of a compatible blend in which above T_m the blend is a single liquid phase and below T_m both pure crystalline PEO and non-crystalline melt exist. As the concentration of PMMA increases, the blend glass transition temperature increases until T_g is above T_m. At that point no crystallites form; thus no melting is observed.

Crystallization under nonisothermal conditions was also a function of blend composition. When blends were cooled at 20°C/min in the DSC, the temperature at which the crystallization exotherms began decreased with increasing PMMA, as shown in the curve labeled T_c in figure 26. The temperature range over which most of the crystallization occurred broadened, as indicated by the width of the vertical bars in the curve for the different blends. Below 60 percent PEO, the crystallization exotherm was very broad and indistinguishable from the baseline even though a small melting endotherm was observed in samples with up to about 30 percent PEO when these samples were reheated. Notice that the non-isothermal crystallization exotherm curved labeled T_c intersected the glass transition curve labeled T_g at the 50/50 blend composition. This is the blend composition where the exotherm became indistinguishable from the baseline. Because the induction time, the time required for the crystal embro to reach its critical size and begin to grow, is longer for higher PMMA, these blends are more easily supercooled to a temperature range at which the crystallization rate is retarded or stopped by the mixture becoming glassy before well-developed spherulites can grow. Clearly, both the degree of crystallinity and the rate of spherulite growth are affected by blend viscosity and glass transition.

2. Spherulite Growth rates in blends of PEO/PMMA. The crystallization kinetics of polymer spherulites are nucleation controlled.[53-55] This means that the rate determining step in spherulite growth is the formation of a critical nucleus which is determined by the free energy difference between the crystal and melt rather than the rate of diffusion

of heat or polymer across the liquid-crystal interface. The two main characteristics of nucleation controlled growth are (1) constant growth rate under isothermal conditions, and (2) negative temperature coefficients of the growth rate at low supercooling. Diffusion controlled crystallization kinetics, on the other hand, are dependent on the square root of time.[56,57,263]

Nucleation controlled growth rates of PEO spherulites have been experimentally verified by optical microscopy,[264,265] dilatometry,[266,267] and DSC.[287,238] Low molecular weight diluent,[102b,268] block copolymers,[143,269] and grafting[146] change the crystallization rate but not the kinetic mechanism. Microscopic measurements are most amenable to theoretical interpretation because the rate of advancement of the spherulite boundary can be determined directly.

Time lapse optical photomicrographs showed that the spherulite growth rates for blends containing between 60 and 100 percent PEO were linear with negative temperature coefficients for low supercooling. The change in spherulite diameter for 90/10: PEO/PMMA blends versus time in figure 27 was very linear, and the growth rate increased as the temperature decreased from 45^{o}C to 35^{o}C. Therefore, nucleation controlled growth rate theories should be applicable in the 60 to 100 percent PEO composition range.

As the spherulite grows, the untransformed melt is depleted and ultimately the spherulites impinge on each other. Since higher molecular weight PEO is preferentially crystallized while low molecular weight and amorphous polymer is rejected, the composition of the melt at the

spherulite boundary will change as the spherulites approach each other if the rate of diffusion of noncrystalline melt is faster than the advancement of the spherulite fibrils. This causes the growth rate to decrease just prior to impingement.

For high molecular weight blends containing from 60 to 100 percent PEO, the spherulite growth rates did not decrease just prior to impingement. None the less, whenever possible spherulites chosen for study were separate and data taken just prior to impingement was not used to determine the growth rate. The lack of change in spherulite growth rate prior to abutment implied that the diffusion of polymer through the melt was slower than the rate of spherulite growth. Thus most of the amorphous material was trapped in the spherulite intersticies, as was shown by the scanning electron and optical microscopy in Section A.

Spherulite growth of blends between 40 and 60 percent PMMA was slow as compared to lower PMMA concentrations but the density of primary nuclei was very high. It was no longer possible to photograph spherulites which were well removed from neighboring spherulites. After a few minutes spherulites had impinged, but were so small and grew so slowly that differences in each time lapse photograph were small causing scatter in the data. In figure 28, the growth rates of a 45/55: PEO/PMMA blend at 45, 40, and 35^{o}C were curved to some extent. These data fit square root of time or linear time plots with about the same correlation coefficient.

The growth rates of non-impinging spherulites (40/60: PEO/PMMA) in figure 29 were also curved, fitted square root of time curves, and were

not influenced by other spherulites. Whether this implies a diffusion controlled growth mechanism is not entirely clear since with time the spherulite growth rate must decrease because there is no more crystallizable polymer and because the melt viscosity has increased. However, the square root of time dependence seems to indicate that diffusion controlled the growth at this concentration, and nucleation controlled growth kinetics may not apply to non-impinging spherulites.

The non-impinging spherulite blends were made from low molecular weight PEO and polymerized PMMA. Similar nonlinearity was observed in viscous oligomer/low molecular weight PEO mixtures.[89,268] Although the growth rates of these blends were not very repeatable from one polymerization to the next, they had dropped five orders of magnitude as compared to 90/10: PEO/PMMA blends at similar supercoolings (more than 200 hours as compared to five minutes' time to impingement). Further, the induction time for these blends was very long (10 hours as compared to 30 seconds or less). It must be inferred from the very slow crystallization rates and long induction times that the viscosity and T_g have increased significantly as compared to the blends with linear growth rates.

3. The Fischer-Turnbull equation.[48] If the crystallization of the PEO/PMMA blends is nucleation controlled, the growth rate, G, will depend on the free energy difference between liquid and crystal and the interfacial viscosity. The well-known Fischer-Turnbull equation describes this type of crystallization. Equation (45) from Chapter I can be written

$$G = G_o \exp(-\Delta F^{\ddagger}/RT)\exp(-\Delta E/RT) \tag{45}$$

where the free energy term may be written as

$$\Delta F^{\ddagger}/RT = Yb_o\sigma\sigma_e/\Delta fkT = (1 + y\Delta T)\ K_g/fT\Delta T \tag{79}$$

and

$$K_g = Yb_o\sigma\sigma_e T_m^{\ o}/\Delta H_f k \tag{80}$$

where Y is either 2 or 4; σ is the lateral surface free energy; σ_e is the fold surface free energy of the PEO lamellae in the spherulites; b_o is the b-axis lattice parameter for the PEO unit cell; ΔH_f is the heat of fusion for 100 percent crystalline PEO; and $T_m^{\ o}$ is the PEO equilibrium melting point. Table III lists some values of these variables and constants for PEO from the literature.

At high supercoolings, the driving force for crystallization will be lower than the simple $\Delta f = \Delta H\Delta T/T_m^{\ o}$ by a factor f because of the decrease in free energy of the supercooled liquid. A good approximation for f is $2T/(T_m^{\ o} + T)$.[60] Also high supercoolings cause the fold surface free energy of the crystal to become dependent on ΔT[60,65]

$$\sigma_e = \sigma_{e1}\ (1 + y\Delta T) \tag{81}$$

where σ_{e1} is obtained from lamellar thickness measurements and approaches the equilibrium fold surface free energy, σ_e, at low ΔT. This dependence will cause only small change in K_g since y should be small ($y = 0.014\ ^oK^{-1}$ for polyethylene). However, at high ΔT when the spherulite growth rates begin to decrease, these terms become very important and therefore

have been included in equation (79).

The interfacial diffusion term, ΔE, for polymer crystallization is usually written[60,65] in the form of the WLF equation [equation (29) in Chapter I].

$$\Delta E/RT = B/\left[C + (T - T_g)\right] = U/R(T - T_\infty) \qquad (29)$$

where $T_\infty = T_g - 30^oK$, and T_∞ is determined by blend composition. A variation in T_∞ of 10^oC causes the growth rate maximum to shift about 2^oC, but the maximum is very broad and only the trend is detectable. A large melting point depression would shift the growth rate maximum also but not enough to identify the effect for blend compositions above 60 percent PEO (see figure 5 in Chapter I).

4a. Comparison of experimental blend growth rates with theory: surface free energies and the bulk free energy term. Spherulite growth rates for WSR-N-3000 poly(ethylene oxide) and high molecular weight PMMA blends of from 100 to 50 percent PEO were plotted versus $1/T\Delta T$ in figure 30. The data used in these plots is tabulated in Appendix II. The plots were linear at low supercooling. Slower growth rates with decreasing ΔT were attributed to the bulk free energy term in the Fischer-Turnbull equation. Slower growth rates with increasing PMMA in the blends can be explained if the interfacial diffusion term, T_∞, in the Fischer-Turnbull equation increases. From the figure it is evident that pure PEO could not be cooled to a sufficiently low temperature for the interfacial diffusion or WLF term to decrease the growth rate. With additional PMMA,

the influence of the diffusion term caused the observed maximum and subsequent downward swing of blend growth rates.

The scatter in the growth rate data of samples of the same blend composition was very high. Although this has been observed for other crystallizable blends,[260] no explanation was given. Three possible explanations are suggested here. (1) It is possible that a slight variation in blend composition existed from sample to sample. (2) PEO degradation,[270-272] especially in acidic medium,[165] tends to decrease the spherulite growth rate. Degradation at high precrystallization temperatures was responsible for lowering the growth rate in low molecular weight PEO single crystals[165] and in poly (chlorotrifluoro-ethylene) crystals.[273] (3) PEO can grow along two different crystal faces[122b,127,274] at different rates. It could not be distinguished from wide angle x-ray patterms of 80/20: PEO/PMMA blends whether the two forms were present or not. Somewhat arbitrarily, the largest spherulites and highest growth rates were preferentially selected when different growth rates were found.

To estimate the effect of supercooling on the surface free energy of 70, 80, and 90 percent PEO blends, the growth rate data was fitted to $\ln G + U/R\ (T - T_\infty)$ versus $(1 + y\Delta T)/fT\Delta T$ for y values of 0.0, 0.0044, and 0.014. Based on the correlation coefficient and the standard deviation in K_g and $\ln G_o$, y values of zero produced the best fits for the three blends. This implies that the presence of high molecular weight diluent does not cause extreme roughness in the fold surface at these blend compositions.

TABLE III - Constants for PEO Crystallization Kinetics

CONSTANT	VALUE	REF
ΔH_f	44.96 cal./g. repeat unit	102b
	47.0 cal./g/ repeat unit	129
T_m^o	348.4^oK, 75.4^oC	60e, 205
	347^oK, 74.0^oC, 69.0	264, 267
k	1.380×10^{-16} erg/^oK	
A	0.214×10^{14} cm^2	
$b_o = \sqrt{A}$	4.63 Å, 4.65 Å	60e
ρ(PEO)	1.2285 g/cc	
ρ(PMMA)	1.17 - 1.19 g/cc	
σ_e	65 ergs/cm^2, 51 erg/cm^2, 70 erg/cm^2	129, 60e, 266b
σ	11.2 erg/cm^2	266b
$U^{\ddagger}$	1500 cal./g.	60e
T_∞ (PEO)	176^oK	
T_∞ (PMMA)	332^oK	
K_g (PEO)	$0.81 \times 10^5 K^2$	60e
ln G_o	11.7 cm/sec	

To estimate the effect of the melting depression, the growth rate data for the same three blend compositions was fitted to ln G + U/R $(T - T_\infty)$ versus $T_m^o/fT\Delta T$ for T_m^o values of 348.4°K, 345°K, and 340°K. In each case the least squares fit became progressively worse as the equilibrium melting temperature decreased. This implies that the high molecular weight diluent does not cause a large melting point depression and is consistent with the melting point measurements in Section B1.

To evaluate K_g and $\sigma\sigma_e$ values of PEO spherulites as functions of blend composition, plots of ln G_r + U/R $(T - T_\infty)$ versus $1/fT\Delta T$ (figure 31) were fitted to straight lines by the least squares technique.[155] The value of T_∞ was estimated as 30 degrees below the glass transition temperature predicted by Fox's equation (equation 44 in Chapter I). The slope of this plot, $-K_g$ and intercept, ln G_o, have been listed in Table IV. Using values from Table III, the $\sigma\sigma_e$ values for PEO spherulites were calculated from equation (80) with Y = 2 and 4. K_g is almost constant if T_∞ is adjusted according to Fox's equation as the PMMA concentration in the blend increases. There is a slight decrease followed by an increase in K_g as PMMA in the blend increases. Assuming T_m^o remains constant this leads to a curved behavior for the surface free energies with a minimum at about 80-percent PEO.

If Lauritzen's criterion[72] is used to determine whether regime I or II kinetics should be used to estimate the surface free energies of the PEO crystals, equation (53) and the K_g values from Table IV predict lamellar thicknesses of about 1.5 Å at 25° supercooling for regime I.

Thus regime II should be used to estimate $\sigma\sigma_e$ values for the PEO crystallites in all blends. Unfortunately, $\sigma\sigma_e$ values calculated for

$$\sigma\sigma_e = K_{gII}\, k\, \Delta H_f / 2b_o\, T_m^o \qquad (82)$$

yielded values of about 1200 erg^2/cm^4, which is too high. Several high molecular weight polymers are known[60] to have Y values from equation (80) that are intermediate between 2 and 4. A value of Y in this range produced $\sigma\sigma_e$ values which compared well with those reported elsewhere.[60,102]

The parabolic curvature of $\sigma\sigma_e$ values was not expected. If, as PMMA in the blend increases, more entanglements in the PEO fold surface occur, then the surface free energy should increase.[67] The implication of the decrease in $\sigma\sigma_e$ with low PMMA concentration is that the presence of PMMA near the fold surface of the PEO decreases the surface free energy as long as the blend viscosity is low enough so that the PEO can easily be removed from the PEO/PMMA melt. It has been proposed[275] for polyethylene that the density defect is not caused by large, switchboard-like folds of the crystallized polymer chain but rather by low molecular weight polymer absorbed on the fold surface. If this is correct, then the preferential adsorption of PMMA at the fold surface would result in a decrease in σ_e at low PMMA concentrations. At higher PMMA with increasing viscosity, entanglements would become significant causing σ_e to increase in accordance with observed behavior. Because of the standard deviation in K_g values, these observations cannot be considered conclusive.

4b. Comparison of experimental growth rates with theory: the diffusion term and T_∞. Plotting equation (49) as $-\left[\ln (G/G_o) + K_g/fT\Delta T\right]^{-1}$

versus temperature should produce straight lines of slope U/R and x-intercept T_∞. Using values from Table IV for K_g and G_o, figure 32 and Table V were obtained. The data at high temperatures, especially for pure PEO and 90/10: PEO/PMMA blends, was so badly scattered that it was not used. Only the high ΔT values for 90/10: PEO/PMMA blend were used. The slopes of these lines increased with PMMA in the blend implying that U decreased slightly. T_∞, the x-intercept, increased as PMMA in the blend increased. The values for T_∞ are all within $\pm 2^oC$ of the Fox equation predictions used to estimate K_g and G_o.

Five successive iterations were performed by substituting the K_g and ln G_o values calculated from fitting ln G + U/R (T - T_∞) versus $1/fT\Delta T$ into $-\left[\ln(G/G_o) + K_g/fT\Delta T\right]^{-1}$ to calculate U and T_∞ and then substituting these values back into the equation for K_g and ln G_o. In each case except for the 60/40: PEO/PMMA blend, the correlation coefficients of both plots improved very slightly. The coefficients for the 60/40 blend became progessively worse. The initial and final values of the 5 iterations are listed in Table VI. The decrease in U from 1600 cal/mole to 1400 cal/mole with increasing PMMA was not expected and could be the result of assuming σ_e values are independent of temperature. Since there were no accurate lamella thickness measurements available for WSR-N-3000 as a function of supercooling, the actual value of y is not known for PEO crystals. Kovacs and Suzuki[95] have shown that the values of U and T_∞ are extremely sensitive to the value of K_g chosen for polystyrene spherulite growth rates. Thus small errors in this term could be responsible for the changes in U and T_∞ with PMMA content.

TABLE IV - Values of K_g and $\sigma\sigma_e$

Calculated from Figure 31

[PEO]	K_g X $10^{5o}K^2$	$\sigma\sigma_e$(I) erg^2/cm^4	$\sigma\sigma_e$(II) ln G_o mm/min
100%	1.23 ± .22	703	1406 16.2 ± .8
90	1.085 ± .08	620	1241 14.9 ± 0.3
80	1.112 ± .04	636	1272 15.0 ± 0.1
70	1.03 ± 0.1	589	1178 14.0 ± 0.1
60	1.5 ± .5	858	1715 16.5 ± 3.0

TABLE V - Values of E and T_∞

Calculated from Figure 32

[PEO]	U X 10^3cal/mole	T_∞ ^oK		T_∞ ^oC
90	1.52	184.5	(186)	-88.5
80	1.50	197	(197)	-76
70	1.48	209	(208)	-64
60*	1.45	224	(222)	-49

*Least squares for straight line based on all points for 60/40: PEO/PMMA blend in figure 32.

TABLE VI - Iterations on K_g, ln G_o, U, and T_∞

[PEO]	Iteration	K_g	ln G_o	Correlation Coefficients
90	1	1.085	14.89	-.9940
	5	1.068	14.74	-.9951
80	1	1.117	14.95	-.9945
	5	1.116	14.96	-.9945
70	1	1.028	14.00	-.9875
	5	1.059	14.21	-.9876
60	1	1.511	16.55	-.9635
	5	1.915	19.81	-.9330

[PEO]	Iteration	U	T_∞	Correlation Coefficients
90	1	1500	186	N.A.
	5	1622	178	-.9774
80	1	1500	197	N.A.
	5	1505	196.8	-.9870
70	1	1500	208	N.A.
	5	1403	213	-.9606
60	1	1500	222	N.A.
	5	1104	240	-.9041

The T_∞ term for 90/10: PEO/PMMA blends decreased on successive iterations from the initial value calculated from Fox's equation. The 80/20: PEO/PMMA blend T_∞ remained constant and the higher PMMA blend T_∞ values tended to increase probably for similar reasons as proposed for the variation in U with PMMA. Notice that the 60/40: PEO/PMMA blend seemed to have a definite change in slope at about 308°K. This would result if the growth rate mechanism changes and the morphology of 60/40: PEO/PMMA blends crystallized at high ΔT are more rod-like than spherulitic. A similar phenomenon was found in DSC isothermal crystallization curves, but because of the limited number of data points, the T_∞ value for the 60/40 blend was taken as the x-intercept of the line fitted through all points. The increase in T_∞ with PMMA content clearly indicated that these two polymers are compatible in the melt over this composition range.

5. The Avrami equation and overall crystallization kinetics. The overall crystallization kinetics of PEO/PMMA blends were investigated by studying isothermal DSC crystallization exotherms as a function of time. The degree of crystallinity at time t for a crystallizing blend is given in Chapter II equation (65) as

$$X_c(t) = \left[H(t) - H_a \right] / \Delta H_f(PEO) = \int_o^t \frac{dQ}{dt}\, dt \qquad (65)$$

where Q is the heat per gram of blend released during crystallization. The overall crystallization rate from isothermal DSC curves at low, constant ΔT decreased with increasing PMMA concentration in the blend, as shown in figures 33 and 34. This reinforced the microscopic observations

that the spherulite growth rates were inversely proportional to PMMA content adding further support to the contention of compatibility in the melt.

The isothermal DSC exotherms for a given blend composition were all generated from the same sample so that the exotherm areas are independent of the mass of the sample and can be compared directly with other exotherms at different temperatures but the same blend composition. Cycling the sample also demonstrates the thermodynamic stability of these blends above their melting point.

If repeated cycling changed the overall growth rates, this would imply that the melt was changing composition. When sufficient time was allowed for the blend to redissolve the PEO formed when the spherulites melted, then repeated crystallization and remelting of any blend would not affect the overall crystallization kinetics as long as no degradation occurred. Cycling a metastable blend through the crystalline transition of one component and then remelting would produce a two-phase mixture with subsequent crystallization kinetics characteristic of the most thermodynamically stable composition.

If the amorphous component's glass transition temperature (the T_g of the PMMA and PEO which did not crystallize) increased as the crystallizing polymer was removed, the redissolution of the pure crystalline polymer into the amorphous blend on melting would take longer the higher the T_g of the amorphous blend that was rejected from the spherulites. This idea was confirmed by the precrystallization time required to get reproducible exotherms from blends of 60 and 70 percent PEO. These blends had to be

kept at 100°C for at least 5 minutes to obtain reproducible isotherms while the 80 to 100 percent PEO blends required only about 2 minutes at this temperature to give the same isotherm on each cycle.

If the Avrami equation (49) in Chapter I were applicable to the isotherms, plots of $\ln\ln(\theta)$ versus $\ln t$ should be straight lines.[100,101] As shown in figures 35 through 37, the plots are nearly linear. The exponent n is slightly higher than 2. The simplest interpretation of an n value of 2 is that nucleation is heterogeneous and independent of time and that growth is two dimensional. Care should be taken in attaching too much significance to this result since other nucleation and growth mechanisms can predict the same result.[65] This value is certainly consistent with spherulites found to grow as disks in a thin film inside a DSC pan.

To obtain constant slopes the assumption of random nuclei distribution must be made in the theory.[100,101] This does not imply that if varying slopes are observed, the Avrami equation cannot be used.[57,100] According to Avrami,[100] as long as the shape of the isotherms are similar, the phase transformation is in the "isokinetic range" within which the data should correlate to a reference time τ independent of temperature and composition.

If the time to 50 percent completion of crystallization, $t_{1/2}$, is arbitrarily chosen as the reference time, the inverse of $t_{1/2}$ should be proportional to G raised to a power. From the Fischer-Turnbull equation (49), G is exponentially dependent on $1/T\Delta T$. Thus a plot of $-\ln t_{1/2}$ versus $1/T\Delta T$ for different blend composition will be similar to the

spherulite growth rate plot in figure 30. For 60 to 100 percent PEO straight lines for low supercooling are observed. These curves in figure 38 are not exactly the same as the spherulite growth rate curves since ln $t_{1/2}$ is proportional to k in equation (65), and k contains both G, the growth rate, and N, the rate of primary nucleation.[276]

As with the optical growth rate measurements at higher PMMA concentrations, the overall crystallization rate passed through a maximum, resulting from the influence of an increased blend glass transition temperature on G and N. At high supercooling and high PMMA content there was more scatter in the data. Note that the data for the blend compositions was not displaced along the $1/T\Delta T$ axis in the same manner as in figure 30. In the optical measurements of spherulite growth rate, the largest shifts along the $1/T\Delta T$ axis were at the highest PMMA compositions because the spherulite growth rate depended on T_∞. The overall crystallization rates, however, depended on both the nucleation rate and spherulite growth rate. As the PMMA concentration increased, the rate of nucleation increased, causing the overall crystallization rate curves to come closer together.

A rough estimate of the number of primary nuclei was made from the value of ln k in the Avrami equation. The spherulite growth rate was calculated from the Fischer-Turnbull equation for a specific blend using the values in tables IV and V. Assuming that the spherulites are disks of height h and that no spherulite grows on top of another, the number of nuclei per unit volume N is given by

$$N \cong k/\pi G^2 h$$

Since the disk height is unknown only Nh can be calculated. This value should vary approximately as N. A plot of log Nh versus $1/fT\Delta T$ for the blend compositions between 60 and 100 percent PEO is shown in figure 39. At low supercoolings, the number of primary nuclei, as indicated in the figure, decreased with increasing PMMA concentration until the blend composition exceeded 30 percent PMMA. Above 30 percent PMMA the number of nuclei increased with PMMA concentration. This is the reason that larger spherulites form in the low PMMA blends than in the pure polymer.

At high supercoolings ($\Delta T > 50$), which were only attainable in the 60/40 and 70/30: PEO/PMMA blends, the number of primary nuclei increased very rapidly. This indicates a different type of primary nucleation mechanism is involved in the overall crystallization kinetics at high supercoolings. Price (referred to by Kovacs et al. in reference 129a) has shown that large numbers of small crystallites nucleate in pure PEO at very high supercoolings. Apparently, similar behavior occurs in highly supercooled blends.

As in the microscopic growth rate measurements, the 60/40: PEO/PMMA blend overall crystallization rate data scattered excessively. This result could be caused by instrumental limitations or by a change in crystallization mechanism. Because of smaller amounts of crystallizable polymer, the DSC sensitivity must be increased. Because crystal nucleation and growth behavior was not exactly the same for each cycle, more scatter in the data is observed. However, this scatter could be the result of competition between different kinetic mechanism. Heterogeneous nucleation controlled growth was the kinetic mechanism for blend crystallization at 60 percent or more PEO, but some possible competing mechanisms

for 60 percent or less PEO include homogeneous nucleation at high supercoolings, diffusion controlled growth, and growth rate changes as a result of degradation. To resolve which, if any, of these different possible mechanisms is correct, further study of the high PMMA composition crystallization kinetics is necessary.

C. Compatibility

A blend of two polymers is compatible when the mixture is miscible in all proportions on a molecular scale. Based on the optical clarity of the melt, the calculated parameters from solution theories, the behavior of the glass transition, and the decrease in crystal growth rate, the PEO/PMMA blend is shown to be compatible in the melt. The term compatibility applies only to the amorphous state. A compatible mixture of two polymers implies intimate mixing and the absence of heterogeneous structure in the liquid phase. When one component crystallizes, the definition of compatibility is violated since the blend is no longer homogeneous, but contains amorphous and crystalline polymer. Characteristics of a compatible mixture include optical clarity, a single glass transition intermediate between the transitions of the pure homopolymers, and effects on the thermodynamic and kinetic properties of the mixture.

1. Optical clarity. If a blend is homogeneous down to about $1/20^{th}$ of the wavelength of light, the mixture will be transparent. Larger inhomogeneities having refractive index differences of more than

0.002 cause opalescence. At all compositions above the melting point of the PEO crystals, the PEO/PMMA blends are transparent. Although transparency is not always conclusive evidence of compatibility,[230b] compatible polymer pairs which do not absorb light should be transparent.

Some of the strongest evidence for compatibility of the intermediate PEO/PMMA blend compositions comes from the redissolution of annealed samples of these blends on heating discussed in Section A-2 of this chapter. When the PEO concentration is between 40 and 60 percent, annealed crystalline blends coalesce very slowly when the temperature is raised above the melting point, and the dissolution process of the two viscous liquids can be observed in the optical microscope (figure 19).

Because this phase coalescence did not occur in blends that were repeatedly crystallized and melted over a short time, the slow perfection of the crystals after spherulite growth is complete, known as secondary crystallization, must continue to extract crystallizable PEO from the amorphous phase during the annealing process. As a result, the glass transition of the amorphous phase increases during the annealing process. The higher glass temperature of the amorphous phase is responsible for slowing down the rate of redissolution of the amorphous regions in the annealed blends when they are melted. The fact that the two liquid phases coalesce implies that these intermediate compositions are compatible.

2. Thermodynamic evidence of compatibility. According to Flory-Huggins theory, conclusive evidence of compatibility would be to show that χ_{12} was less than the critical value for phase separation given by

equation (9) in Chapter I. Unfortunately, the heat of mixing and therefore the interaction parameter was very nearly zero. If χ_{12} were very large and negative, it could be calculated from melting point depression measurements.[35,192] However, if χ_{12} approaches zero in high molecular weight blends, a melting point depression will not occur, as shown by equation (41) in Chapter I. Since both compatible blends with χ_{12} of 0 and incompatible polymers have no melting point depression, the lack of melting point depression implies neither compatibility nor incompatibility.

The theoretical value of the solubility parameters of both polymers can be calculated from equation (14) and Hoy's[19] values for the molecular attraction coefficients. Calculated values for PEO and PMMA are 9.252 and 9.205, respectively. Krause[16] has shown that the critical solubility parameter difference for two polymers with a degree polymerization of 1000 is 0.11; therefore, this pair is predicted to be miscible according to the Flory-Huggins' theory. The more advanced equation of state theory of Sanchez and Lacombe[37a] also predicts that if the blend mixing energy parameter is small, this pair should not have an upper critical solution temperature.

3. Glass transitions as measured by DSC. Ordinarily the compatibility of two polymers is demonstrated by measuring the glass transition temperature of the blend. If at any given composition the blend has a single glass transition, that composition is considered compatible.[10,234] Two glass transitions indicate the presence of two phases and hence an incompatible blend. However, the temperature at which the glass trans-

sition occurs is unsubstituted, highly crystalline, linear polymers is a subject of considerable confusion and controversy.[235-237]

In poly(ethylene oxide), for example, the glass transition temperature, as measured by calorimetry,[107,238,239] dynamic mechanical[240,241] and dielectric relaxations,[240,242,243] is a function of both molecular weight and degree or crystallinity. The glass transition temperature reaches a maximum at a molecular weight of 10,000 and then decreases with further molecular weight increase. Above this molecular weight, the percent crystallinity depends on thermal history; quenching the polymer thus decreases the glass temperature. Accordingly, the degree of crystallinity of the PEO causes the glass transition temperature to deviate from its usual molecular weight dependence.

Measuring the glass transition temperature of a blend, such as PEO/PMMA, containing a highly crystalline component presents three special problems not found in completely amorphous blends. (1) Because the crystallizable blend is difficult to quench to an entirely amorphous state,[241] the amorphous composition and therefore T_g depends on how much PEO has crystallized out. (2) The melting endotherm or recrystallization exotherm can obscure the glass transition if T_g and the crystalline phenomena are close together.[78,257] (3) Because the intensity of T_g decreases with increasing crystallinity, it is difficult to identify this amorphous transition in highly crystalline blends. These three factors make glass transition measurements on crystallizable blends difficult.

Different thermal histories, e.g., quenching, isothermally crystallizing, or annealing cause crystalline blends to have differing degrees

of crystallinity. Since the amorphous blend composition changes with the degree of crystallinity of the PEO, the glass transition temperature would be expected to increase with increasing crystallinity because T_g depends on the amorphous composition. The DSC thermograms in figure 40 illustrate the effect of thermal history on a crystallizable blend and the difficulties involved in determining an accurate glass transition temperature.

The calculated glass transition temperature for the 60/40: PEO/PMMA blend in figure 40 was -21^{o}C. When a DSC trace (scan a in the figure) was run on a specimen annealed at 45^{o}C under vacuum for 6 weeks, no transition was observed (other than melting) through the temperature range from -100^{o}C to 170^{o}C. The brackets in scan a indicate a change in sensitivity from 5 mcal/sec to 20 mcal/sec. The other scans were run at 5 mcal/sec. After this DSC trace was taken, the specimen was crystallized isothermally in the DSC at 22^{o}C and then rescanned (scan b in the figure) at the same heating rate and sensitivity. In the second scan an apparent glass transition was found at 40^{o}C, immediately prior to the recrystallization exotherm between 45^{o}C and 60^{o}C. This same sample was melted a third time, rapidly quenched to -100^{o}C, and then rescanned (scan c in the figure). Now the apparent glass transition temperature occurred at -43^{o}C and was followed by a broad recrystallization exotherm beginning at approximately -20^{o}C.

Although the reasons for this behavior are not entirely clear (probably several factors contribute), the change in amorphous composition is primarily responsible for the observed difference in glass

transition temperature. The glass transition temperature increases directly with the degree of crystallinity, thus annealed blends should have the highest T_g. If the blends could be quenched completely, the glass transition temperature should be predicted by equation (92), the well-known Fox equation.[221] However, because PEO nucleates homogeneously at about -20°C[247] as very small crystallites, and because of high nucleation rates in the blends at high supercoolings, it is not easy to quench this polymer. The apparent glass transition of quenched PEO/PMMA may be attributed to the onset of motions in the amorphous blend near the small, imperfect crystals. This transition would not be indicative of the interstitial amorphous blend composition.

There are two possible explanations for the lower than expected T_g (-41°C) in the quenched blend in figure 40c. (1) The homogeneously nucleated PEO crystals, being very small, would have a very rough fold surface rich in amorphous PEO which would be responsible for the low T_g. Mandelkern[249] has proposed a three-phase model that, with slight modification, applies here. His model, shown schematically in figure 41a, consists of an interzonal amorphous layer atop a random reentry interfacial zone of switchboard-like folds on the surface of the lamellar crystal. At high degrees of supercooling, this interfacial zone or very rough fold surface (it need not be a switchboard-like fold surface) is responsible for the low T_g. The recrystallization exotherm masks the T_g of the interzonal amorphous layer, causing the observed T_g (that due to the rough fold surface) to be lower than would be expected for the blend. In this adaptation of Mandelkern's model (figure 41a) the interzonal

amorphous phase contains a higher PMMA concentration, represented by dotted chains, than the fold surface.

In well-annealed or isothermally crystallized blends, which would have a more regularly folded surface (figure 26b), the interfacial zone is very regular and does not contribute an observable glass transition. The interzonal phase is now responsible for the glass transition. The interzonal phase is composed mostly of PMMA and has a glass transition temperature considerably higher than is predicted by Fox's equation. Annealed blends differ from quenched blends in that they have tighter, more regular folds; higher interzonal T_g; only a small recrystallization exotherm (if any); and more perfect crystals. Effectively the three-phase model has become the more common two-phase model. The interzonal phase rather than the fold surface is the amorphous phase and the PEO lamellae, including the fairly regular folds, are the crystalline phase.

The other possible explanation for the observed low T_g in quenched samples is that the PEO had not completely redissolved into the melt before the blend was quenched. In the section on crystallinity, it is found that blends of 30 to 60 percent PMMA require longer remelting times than pure PEO or the lower diluent concentration blends to obtain reproducible crystallization kinetics. If the PEO has not completely redissolved and the blend is rapidly quenched, a lower T_g would be expected for the same reason given above but without invoking Mandelkern's model.

DSC traces of rapidly quenched samples (figure 42) indicate that blends of 0 to 20 percent PMMA have glass transition temperatures that

increase with increasing PMMA content. Since the glass transition temperature of pure PEO increases with increasing crystallinity[239-243] and because of the high scanning rate, it is not surprising that the glass transition temperatures of these blends are slightly higher than the calculated value.

The small apparent transition at about -75°C in all the blends is probably the result of some contaminant in the PEO or a baseline anomaly in the instrument. However, a low temperature transition supposedly associated with PEO's glass transition has been reported in this region by DSC[245] and at much lower temperatures using a dilatometer.[246]

Notice in figure 42 that only the 70/30: PEO/PMMA blend (scanned in the figure) has a T_g lower than that predicted by Fox's equation. If the time in the melt is increased so that isothermal crystallization kinetics are repeatable (about 5 minutes), the spherulite growth rate depends on the T_g predicted by the Fox equation. This implies that the polymers are compatible in the melt despite the variation in glass transition temperature observed from DSC and dynamic mechanical measurements. For further discussion on this point, see the section on crystallinity. Neither the explanation based on Mandelkern's model nor that of incomplete redissolution can be proven conclusively from DSC results since the problems of homogeneous nucleation of PEO and recrystallization of less perfect crystals exist regardless of whether or not the PEO has completely redissolved.

It is possible to calculate the glass transition temperature of the interzonal amorphous blend from equation (78) in Chapter II using

the weight fraction of amorphous polymers only. Assuming all the amorphous PEO is in the interzonal layer,

$$\frac{1}{T_g} = \frac{(1-X_c)W_1 \; / \left[(1-X_c)W_1 + W_2\right]}{T_{g_1}} + \frac{W_2/\left[(1-X_c)W_1 + W_2\right]}{T_{g_2}} \qquad (83)$$

where the subscripts 1 and 2 indicate crystalline and amorphous polymer, respectively; W_i is the weight fraction of polymer i; T_{g_i} is the glass transition temperature of polymer i (taken as -67^oC for PEO and 104^oC for PMMA to calculate figure 43); and X_c is the degree of crystallinity of the PEO. When PEO crystallizes from the amorphous melt, the glass transition temperature of the remaining melt increases according to this equation.

The degree of crystallinity used in figure 43 was calculated by integrating DSC melting endotherms from annealed and quenched blends. The upper curve was based on the degree of crystallinity of annealed blends while the middle curve was from quenched samples. Equation (83) predicts the lowest T_g's for completely amorphous blends. Because of the complications of recrystallization and melting, it was impossible to verify the presence of an interzonal glass transition from DSC or dynamic mechanical measurements of blends between 30 and 60 percent PMMA.

4. Evidence for PEO/PMMA compatibility from dynamic mechanical relaxations. The dynamic tensile moduli and loss tangent for PEO/PMMA blends of from 40 to 100 percent PMMA were measured on a Rheovibron D.D.V.II. The thin vibron tensile specimens tended to break at spherulite boundaries during testing. Because of the large spherulites in

blends containing 70 percent or more PEO, these compositions were not tested. Because of their complexity, modulus curves of the different blends have been shifted up or down the abscissa, as indicated in the figure captions to reduce confusion. Samples were taken from a vacuum oven kept at 80°C; transferred to the instrument; and cooled as rapidly as possible in the low temperature chamber of the instrument using cold nitrogen gas.

Three specific difficulties, similar to those found with DSC measurements, were encountered in determining the glass transition temperatures of blends in which T_g was less than T_m. (1) When T_g approaches T_m, the melting point and alpha relaxations obscured the glass transition.[224,235] (2) Recrystallization, because of the broad temperature range over which it occurs, complicates the identification of other relaxations.[253,254] (3) The broad beta relaxation of the PMMA ester side group[255] may also be responsible for some of the confusion in the loss modulus curves.

The tensile storage modulus for blends of 40 to 100 percent PMMA (figure 44) depended (as in DSC measurements) on the degree of crystallinity of the PEO in the blend. Blends in which more than 20 percent of the PEO had crystallized (50 percent or higher PEO in the blend) all became rubbery at about 50°C. This was approximately the melting point of quenched blends, according to DSC measurements. When the glass transition was nearly equal to the melting point (40 percent or less PEO), crystallization is very slow, and the precipitous drop in storage modulus corresponded to the glass transition of the amorphous portion of the blend.

The arrows above the storage modulus curves indicate the glass transition temperature for each blend calculated from equation (44) in Chapter I. Taking the glass transition temperature as the temperature when the storage modulus is 0.9 times the modulus of the glassy polymer[211] yields consistently higher values of T_g than calculated because of a small amount of crystallinity present even in the 20/80: PEO/PMMA blends and the frequency dependence of the glass transition. Even though a few degrees higher than predicted, the glass transition temperatures for blends of 60 percent or more PMMA increase in the same manner as the equation predicts; therefore, these compositions are compatible.

The 50/50 blend (figure 44) is the best example of how recrystallization affected the modulus curves. At about -100^{o}C there is an increase in the storage modulus as a result of the perfecting of the PEO crystallites within the blend. Apparently, the formation of larger, more perfect crystals by melting and recrystallization or by isothermal thickening or other mechanisms produces internal stresses in the blend as the density decreases and the perfected crystalline regions have better load bearing capabilities. The modulus first decreases slightly as the poorly crystalline regions rearrange or melt, then increases as the crystallites thicken and become more perfect, and finally, decreases when the new crystals approach their melting point and the internal stresses caused by recrystallization relax. This behavior is exhibited to a lesser extent in all of the quenched blends which contain some crystallinity but occurs at higher temperatures as the PMMA

concentration increases.

Loss modulus curves for the five blends had several relaxation maxima (figure 45). In all cases there was a low temperature relaxation at about -130°C which shifted to higher temperatures with increasing PMMA content. A second relaxation occurred at about -50°C and also shifted to higher temperatures with increasing PMMA content. A very broad relaxation, or probably a combination of relaxations which was independent of blend composition, was found between -30° and 50°C.

Tentative assignments for these peaks were made from data in the literature for PEO[238-246] and PMMA.[249-251] The low temperature relaxation was associated with an amorphous backbone rotation in the PEO occurring at -128°C (Takayanagi, et al.[252]). These researchers also found a very low temperature shoulder (-163°C) below the temperature at which the current measurements were performed. Since the T_g of pure PEO depends on the degree of crystallinity, the relaxation at -50°C was probably caused by motions in the PEO fold surface.[246] The broad relaxation between -30° and 50°C probably conceals the alpha relaxation of crystalline PEO (40°C),[240] the broad beta relaxation in PMMA (0°C),[251] and the melting transition (50°C). It is also likely that PEO recrystallization contributed to the lack of peak definition in this temperature range.

The behavior of the loss tangent for these blends (figure 46) was similar to the storage modulus. Tan delta of the blends having a T_g lower than T_m increased dramatically at the melting point. For blends in which the T_g should be higher than T_m, the increase in tan delta

occurred at about the glass transition temperature of the blend. This confirmed the compatibility of blends between 60 and 100 percent PMMA. Unfortunately, there was no maximum in the tan delta curves. Although this is common with vibron measurements,[258] the T_g based on the maximum in tan delta could only be approximated for these samples.

5. Conclusion: The PEO/PMMA blend is compatible over its entire composition range. In summary, from these data and the crystal growth rates, discussed in Section B, it was concluded that the polymers PEO and PMMA are compatible above the crystallization temperature of the PEO. Although most of the data was taken on high molecular weight PEO (WSR-N-3000) and PMMA, data from low molecular weight Carbowax-6000 and PMMA also indicated low molecular weight blends were compatible. Theory[6,37] predicts that ultra-high molecular weight polymers become incompatible and equation-of-state theories[36,37] predict lower critical solution temperatures for high molecular weight polymers. Within the molecular weight range from 400,000 to 6,000, PEO and PMMA form compatible blends over their entire composition range from above the melting point of the PEO to 300°C. Above 300°C these polymers begin to degrade. No evidence of LCST behavior was observed. For low molecular weight PEO the solubility parameter increases considerably because of the increasing hydroxyl endgroup concentration. No attempt was made to determine if a lower molecular weight limit to compatibility of these blends existed.

The evidence for compatibility of the PEO/PMMA blends was not straightforward enough so that a single set of tests would prove definitive. Therefore, different methods were combined to demonstrate

blend compatibility over the entire composition range. The optical clarity of all blends above the melting point implied that refractive index fluctuations were small. In blends containing between 50 and 100 percent PEO, crystal growth rates were suppressed with increasing PMMA concentration, indicating that the viscosity of the melt depended on blend composition. The glass transition by DSC in blends containing between 80 and 100 percent PEO and by Rheovibron in blends containing between 60 and 100 percent PMMA showed that the onset of microbrownian motion (the glass transition) is determined by intimate mixing of both polymers. Above the melting point, coalescence of well annealed blends implied that the two liquids were miscible between 40 and 60 percent PEO. The influence of blend composition on these physical properties provided conclusive evidence of blend compatibility and lead to the surprising conclusion that in the liquid state, PEO and PMMA were homogeneously mixed on the molecular scale.

D. Conclusions

1. Blend compatibility above the melting temperature. Blends of poly(ethylene oxide) and poly(methyl methacrylate) exhibited unique morphologies, depression of spherulite growth rates with increasing PMMA concentration, and a complex transition behavior. The morphology and crystallization kinetics were functions of the glass transition temperature of the blend. Based on morphological evidence, the behavior of the glass transition, and the crystallization kinetics, the PEO/PMMA blend

was shown to be compatibility at all compositions above the melting point of the PEO.

Compatibility of the PEO/PMMA mixtures in the melt is responsible for the lower rates of crystallization found with increasing PMMA in the blend. Incompatibility in the melt would lead to constant spherulite growth rates, though, of course, primary nucleation could be affected. Because in all cases in which crystallites were formed, the growth rates depended on PMMA concentration and for glassy blend composition the T_g depended on blend composition, it must be concluded that this blend is compatible in the liquid state.

2. The effect of high molecular weight diluent on PEO crystallization. Crystallinity of the PEO is affected mainly by the WLF or interfacial transport term in the Fischer-Turnbull equation. The effects of T_g on spherulite growth rates and overall crystallization kinetics are consistent with Fox's equation for the dependence of the glass transition on blend composition. Thus the growth rate is an exponential function of ΔT and T_∞.

The bulk free energy term in the Fischer-Turnbull equation agreed with the melting behavior and thermodynamics of mixing predictions in that no melting point depression was found. K_g was shown to be almost independent of PMMA concentration which implied that $\sigma\sigma_e$ and T_m^o were independent of the free energy of mixing for a high molecular weight diluent of nearly zero interaction parameter. There was apparently a slight dependence of $\sigma\sigma_e$ on supercooling and on surface adsorption of

and entanglement with PMMA. Further study is needed to separate and characterize these effects.

The overall crystallization rate gave n values of about 2 for the Avrami equation indicating two-dimensional growth in the DSC. It was shown that there was an "isokinetic range" over which the kinetics of crystallization were simply related to a characteristic time. When the half time of crystallization was chosen as the characteristic time, the mechanism of overall crystallization was consistent with the nucleation controlled growth of Fischer and Turnbull at least up to blend compositions of 60/40: PEO/PMMA. Above this PMMA concentration, spherulite growth rates became nonlinear and some modification of the kinetic mechanism is required. Further work with 50 percent or higher PMMA blend crystallization kinetics will be necessary before the crystallization behavior at high viscosities can be completely understood.

E. Suggestions for Further Work

Before prediction of blend morphologies and of crystallization behavior of compatible blends is possible, much work is needed. Morphologically at least two areas of ignorance exist. (1) What is the effect of the second component on the lamella thickness? Preliminary attempts at small angle x-ray, SAX, measurements produced no maxima below 300 Å for 80/20: PEO/PMMA blends even though wide angle x-ray patterns indicate high degrees of crystallinity. This may have resulted from inadequate temperature control of the blend crystallization

or isothermal thickening of the lamellae to thicknesses beyond the 300 Å limit of the SAX camera. (2) Small angle light scattering measurements of these blends, expecially V_V patterns at high PMMA compositions could be used to study both nonimpinging spherulite and redissolution phenomena of the 40 to 60 percent annealed PEO blends.

Studies of the compatibility of these blends in the melt, the effect of annealing and high PEO content on dynamic mechanical properties, and techniques for determining compatibility above and below the glass transition temperatures of the blends are needed. If blends are annealed, then recrystallization should not interfere with the melting behavior and perhaps the glass transition of the amorphous intersticial melt could be identified.

There are at least three areas in which blend crystallization kinetics require further investigation. (1) The effect of depletion of crystallizable polymer from the melt on the growth rates is not understood. Does long range diffusion determine the crystallization kinetics at high PMMA concentrations or is the variation of T_∞ with removal of PEO from the melt responsible for the curvature of the growth rate at intermediate PEO concentrations? (2) Are the effects of adsorption and entanglement really responsible for the $\sigma\sigma_e$ variations with blend composition? (3) What are the pertinent parameters controlling primary nucleation as a function of blend composition? Clearly from comparision of optical spherulite growth rates and overall kinetics from DSC measurements, primary nucleation is dependent on composition. A theoretical basis for this dependence is not currently available in

the literature.

An old proverb says, "It is the glory of God to conceal a thing; but the honor of kings to search out the matter."[277] There is much honor yet to be gained searching out the matter of compatible crystallizable polymer blends.

APPENDIX I
RHEOVIBRON PROGRAM

```
      PROGRAM VIBRON(INPUT,OUTPUT,TAPE10)
C  LOG10(EPRIME) AND LOG10(EDOUBLEPRIME) ARE PLOTTED AS FUNCTIONS OF
C     THE TEMP. WITH OPTION TO PLOT LOG10(J) AS WELL
C     VARIOUS VALUES (VARIABLES) USED IN THE PROGRAM. THICK
C     IS THE THICKNESS (AVERAGE) IN MILS, WIDEO IS THE AVERAGE
C     WIDTH IN CM. ALO IS THE LENGTH AT ROOM TEMPERATURE WHICH IS USED
C     TEMP(J) IS OBVIOUS, GAGE IS THE INCREMENTAL VALUE OF THE CHANGE
C     IN LENGTH FROM WHATEVER THE BASE VALUE IS CHOOSEN AS.
C     D IS THE DYNAMIC FORCE VALUE, AF IS THE AMPLITUDE FACTOR VALUE.
C     DELTA IS THE VALUE OF TANGENT DELTA FROM THE VIBRON
C  DATA CARD SEQUENCE
C  NPLOT, WHERE NPLOT=1 TO PLOT AND 0 TO CALCULATE ONLY
C  TMAX,TMIN,EMAX,EMIN,AJMAX,AJMIN,TANMAX,PJT- MAX TEMP.-MIN TEMP.-
C  MAXLOG(E) ETC) -MAX LOSS TAN- PJT=1. TO SKIP J PLOTS, 2 TO INCLUDE
C  J PLOT
C  IDENT. CARD- TITLE DESIRED ON GRAPH MUST APPEAR IN FIRST 15 COLUMNS
C  THICKO,WIDEO,ALO
C  DATA CARDS FOR 110 HZ
C  BLANK
C  IDENT. CARD
C  THICKO,WIDEO,ALO
C  DATA FOR 11 HZ
C  BLANK
C  DATA FOR 3.5 HZ
C  AT THE END OF FINAL DATA CARD, -1 MUST APPEAR IN COL 22 AND 23
C  LAST CARD OF DECK MUST HAVE 6,7,8,9, MULT,PUNCHED IN FIRST COL
      DIMENSION DJ(300),PJ(300)
      DIMENSION REP(300)
      DIMENSION GG(300)
      DIMENSION SS(300)
      DIMENSION HEADING(8),TEMP(300), EPRIME(300),EDOUBLE(300),AAL(300)
      DIMENSION SLOPE(300),DELTA(300)
   82 FORMAT(1H ,*E PRIME -7    LOSS -7     TAN DELT*,
     1*    LOG EPRIME    LOG EDOUBLE*,
     2*   TEMP (C)      1/TEMP        LOG(J DO)    LOG(JP)*)
       READ 6000, NPLOT
6000   FORMAT(I1)
      READ 150,TMAX,TMIN,EMAX,EMIN,AJMAX,AJMIN,TANMAX,PJT
 150  FORMAT(8F5.0)
       IF(NPLOT .EQ. 0) GO TO 111
      CALL PLOTS(10)
      CALL PLOT(0.,-11.,-3)
      CALL PLOT(0.,.5,-3)
 111  DO 600I = 1,200
      TEMP(I) = 0.0
      GG(I) = 0.0
```

```
      DJ(I) = 0.0
      PJ(I) = 0.0
      AAL(I) = 0.0
      EPRIME(I) = 0.0
      REP(I) = 0.0
      SS(I) = 0.0
      DELTA(I) = 0.0
      SLOPE(I) = 0.0
 600  EDOUBLE(I) = 0.0
      PRINT 4000
4000  FORMAT(1H,//)
  22  READ 1, (HEADING(I), I=1,8)
   1  FORMAT(8A10)
   6  FORMAT(1H1,8A10)
      PRINT 6, (HEADING(I),I=1,8)
      PRINT 89
  89  FORMAT(1H ,///)
      PRINT 82
      J = 0
      K = 0
   7  READ 5, THICKO,WIDEO,ALO
   5  FORMAT(3F10.2)
      AREA = THICKO*WIDEO*0.00254
      VO = THICKO*WIDEO*ALO
   2  J = J + 1
      READ 10, TEMP(J),GAGE,D,DELTA(J),AF
  10  FORMAT(5F10.2)
      QT=.878*TEMP(J)-1.39
      TEMP(J)=QT
      IF(D)90,90,1000
C     THE VALUE OF -D- WILL BE THE TEST NUMBER
 1000 X=ATAN(DELTA(J))
      IF(AF - 2.)42,43,42
   43 AF=SORT(10.)
   42 Y=COS(X)
      AL = ALO +(GAGE* .001)
      SS(J) = GAGE
      AAL(J) = AL
      EPRIME(J) = ((200.*AL*Y)/(AREA*AF*D))
      EDOUBLE(J) = EPRIME(J)*DELTA(J)
      GG(J)=ALOG10(EPRIME(J)+7.
      REP(J) = 1./(TEMP(J) + 273.)
      DJ(J) = EDOUBLE(J)/((EPRIME(J)**2.)+(EDOUBLE(J)**2.))
      PJ(J) = EPRIME(J)/((EPRIME(J)**2.) + (EDOUBLE(J)**2.))
      PJ(J)=ALOG10()J(J))-7
      TF(DELTA(J).LT.1.E-4) GO TO 70
      DJ(J)=ALOG10(DJ(J))-7
      SLOPE(J)=ALOG10(EDOUBLE(J))+7.
      GO TO 78
```

```
 70 DJ(J)=1. $ SLOPE(J)=1
 78 B=REP(J)
    K = K + 1
    IF(K - 1)9,100,9
100 PRINT 18,EPRIME(J),EDOUBLE(J),DELTA(J),GG(J),SLOPE(J),TEMP(J),8,
   1 DJ(J),PJ(J)
 18 FORMAT(2F12.3,3X,F9.3,5X,F8.3,4X,F9.3,4X,F9.1,5X,F10.5,4X,2=10.3)
    GO TO 2
  9 CONTINUE
    PRINT 18, EPRIME(J),EDOUBLE(J),DELTA(J),GG(J),SLOPE(J),TEMP(J),8,
   1DJ(J),PJ(J)
    GO TO 2
90  CONTINUE
    IF(NPLOT.EQ.1) CALL PIC(DELTA,GG,SLOPE,TEMP,DJ,PJ,HEADING,J-1,
   1 TMAX,TMIN,FMAX,EMIN,AJMAX,AJMIN,TANMAX,PJT)
532 IF (D .GE. 0.0) GO TO 22
 80 IF (NPLOT.NE.0) CALL PLOT(0.,0.,999)
    STOP
    END
```

APPENDIX II

TABLE OF ISOTHERMAL GROWTH RATES FOR PEO/PMMA BLENDS

100 percent WSR-N-3000

T^oC	G_r mm/min
58	7.2×10^{-5}
52	$3.5 \pm 1 \times 10^{-3}$
51	$1.4 \pm .02 \times 10^{-2}$
50	$1.4 \pm 1 \times 10^{-2}$
49	$4.4 \pm .5 \times 10^{-2}$
48	$3.7 \pm .2 \times 10^{-2}$
46	$5.01 \pm .01 \times 10^{-2}$
45	3.37×10^{-1}
40	$5.8 \pm .1 \times 10^{-1}$
35	1.47
15	2.36
10	2.26

90/10: WSR/H$\overline{M}$

T^oC	G_r mm/min
58	$5.1 \pm .1 \times 10^{-5}$
56	$5.3 \pm .2 \times 10^{-4}$
52	1.3×10^{-4}
50	$1.6 \pm .4 \times 10^{-2}$
48	3.24×10^{-2}
46	3.85×10^{-2}
45	7.4×10^{-2}
44	5.5×10^{-2}
42	1.64×10^{-1}
40	$2.7 \pm .5 \times 10^{-1}$
35	4.5×10^{-1}
30	7.8×10^{-1}
25	1.06
22	$1.28 \pm .05$
20	1.34
17	$1.40 \pm .05$
15	1.52
10	1.74
5	1.96
3	1.87
0	1.95
-3	1.80

80/20: WSR/$H\overline{M}$

$T^{o}C$	G mm/min
42	7.71×10^{-2}
40	1.36×10^{-1}
38	1.67×10^{-1}
36	2.03×10^{-1}
35	2.52×10^{-1}
33	3.27×10^{-1}
30	3.12×10^{-1}
25	4.98×10^{-1}
24	5.22×10^{-1}
23	5.37×10^{-1}
21	5.88×10^{-1}
18	4.83×10^{-1}
16	6.11×10^{-1}
14	6.78×10^{-1}
10	6.55×10^{-1}
6	5.43×10^{-1}
2	5.13×10^{-2}

70/30: WSR/HM̄

T^oC	G mm/min
45	$2.1 \pm 1 \times 10^{-2}$
40	5.9×10^{-2}
35	$1.01 \pm .1 \times 10^{-1}$
25	1.00×10^{-1}
20	1.41×10^{-1}
15	$1.40 \pm .01 \times 10^{-1}$
10	$1.3 \pm .1 \times 10^{-1}$
5	0.64×10^{-1}

60/40: WSR/HM̄

T^oC	$G_r \times 10^{-3}$ mm/min
45	1.21
40	3.1
35	3.53
30	3.78
25	$8.75 \pm .05$
20	7.9
15	7.3
10	6.6
0	$1.86 \pm .03$
-5	1.53

APPENDIX III

TABLES OF AVRAMI CRYSTALLIZATION KINETICS

100 PERCENT AVRAMI CALCULATIONS

T^oC	n	ln K	Corr coef	G_r cm/min	N nuclei/cm^2
51	2.23 (2.21)	-2.88 (-2.90)	.99886	6.4×10^{-4}	4.31×10^4
50	2.10 (2.08)	-1.57 (-1.58)	.9992	1.09×10^{-3}	5.55×10^4
49	2.20 (2.16)	-0.45 (-0.48)	.9985	1.77×10^{-3}	6.46×10^4
48	2.16 (2.19)	0.33 (.33)	.9989	2.77×10^{-3}	5.79×10^4
47	2.10 (2.09)	1.41 (1.40)	.9986	4.17×10^{-3}	7.50×10^4
46	2.15 (2.14)	2.06 (2.03)	.9986	6.09×10^{-3}	6.73×10^4

<n> = 2.15 ± 0.06

90/10: WSR AVRAMI CALCULATIONS

T^oC	n	ln K	G_r cm/min	N nuclei/cm^2
47	2.07	-1.53	3.97×10^{-3}	4.37×10^3
45	2.10	-0.61	7.42×10^{-3}	3.14×10^3
43	2.10	0.13	1.26×10^{-2}	2.27×10^3
41	2.11	1.44	2.0×10^{-2}	3.38×10^3
39	2.03	1.93	2.95×10^{-2}	2.51×10^3

<n> + 2.08 ± 0.03

80/20: WSR/HM̄: AVRAMI CALCULATIONS

T^oC	n	ln K	G_r cm/min	N nuclei/cm^2
39	2.10	-2.33	1.46×10^{-2}	1.46×10^2
38	2.19	-1.78	1.73×10^{-2}	1.81×10^2
37	2.05	-1.40	2.02×10^{-2}	1.93×10^2
35	2.17	-0.50	2.66×10^{-2}	2.73×10^2
34	2.02	0.43	3.01×10^{-2}	5.41×10^2
33	1.95	0.25	3.36×10^{-2}	3.62×10^2
32	2.40	0.05	3.72×10^{-2}	2.41×10^2
31	2.11	0.96	4.08×10^{-2}	4.95×10^2
30	2.19	1.23	4.44×10^{-2}	5.51×10^2
29	2.14	1.73	4.80×10^{-2}	7.81×10^2
28	2.28	1.70	5.14×10^{-2}	6.61×10^2
27	2.19	2.10	5.46×10^{-2}	9.54×10^2

$\langle n \rangle = 2.16 \pm 0.12$

70/30: WSR/HM: AVRAMI CALCULATIONS

$T^{o}C$	n	ln K	Corr coef	G_r cm/min	N nuclei/cm^2
32	2.32	-2.56 (-2.58)	.998	1.23×10^{-2}	1.62×10^{2}
31	2.33	-1.68	.985	1.32×10^{-2}	3.43×10^{2}
29	2.23	-1.06		1.46×10^{-2}	5.17×10^{2}
28	2.45	-1.28 (-1.28)	.985	1.52×10^{-2}	3.83×10^{2}
26	2.17	-0.23		1.61×10^{-2}	9.74×10^{2}
24	2.08	0.08		1.66×10^{-2}	1.25×10^{3}
24	2.02	0.10			1.27×10^{3}
22	2.38	-0.042 (-.05)	.998	1.67×10^{-2}	1.10×10^{3}
21	2.13	0.95		1.66×10^{-2}	3.00×10^{3}
20	2.24	0.68	.999	1.63×10^{-2}	2.35×10^{3}
19	2.13	1.42		1.60×10^{-2}	5.14×10^{3}
17	1.98	1.287 (1.37)	.992	1.51×10^{-2}	5.05 (5.48) $\times 10^{3}$
16	2.19	1.93		1.46×10^{-2}	1.04×10^{4}
15	2.25	2.00		1.39×10^{-2}	1.21×10^{4}
13	2.17	2.36		1.26×10^{-2}	2.14×10^{4}
12	2.35	2.73		1.18×10^{-2}	3.49×10^{4}
12	2.21	2.445 (2.40)	.993		2.62×10^{4}
2	2.27	3.24 (3.27)	.997	4.65×10^{-3}	3.77×10^{5}
2	2.24	3.23	.996		3.73×10^{5}
-6	2.30	2.78		1.35×10^{-3}	2.81×10^{6}
-8	2.35	3.00		9.14×10^{-4}	7.64×10^{6}

60/40: WSR/HM̄: AVRAMI CALCULATIONS

T^oC	n	ln K	G_r cm/min	N nuclei/cm^2
32	2.23	-3.42	9.59×10^{-4}	1.13×10^4
29	2.08	-1.66	1.25×10^{-3}	3.88×10^4
27	2.08	-1.70	1.40×10^{-3}	2.95×10^4
25	2.01	-0.97	1.51×10^{-3}	5.39×10^4
22	2.01	-0.73	1.56×10^{-3}	6.32×10^4
22	2.25	-1.70		2.4×10^4
17	2.01	-0.80	1.35×10^{-3}	7.85×10^4
15	2.01	-0.66	1.19×10^{-3}	1.16×10^5
12	1.87	-0.40	9.21×10^{-4}	2.52×10^5
2	1.87	-0.13	1.97×10^{-4}	7.23×10^6
-3	2.01	-0.98	5.65×10^{-5}	3.74×10^7
-8	1.80	-0.83	1.06×10^{-5}	1.25×10^9

BIBLIOGRAPHY

1. J. W. Gibbs, The Collected Works of J. Willard Gibbs, Vol. I, Thermodynamics, pp. 56-352, Yale Press, New Haven, Connecticut (1948).

2. J. H. Hildebrand and R. L. Scott, The Solubility of Non-electrolytes, Reinhold, New York (1950).

3. J. H. Hildebrand, R. L. Scott and J. M. Prausnitz, Regular and Related Solutions, van Nostrand-Reinhold, Princeton, New Jersey (1970).

4. H. Tompa, Polymer Solutions, Academic Press, New York (1956).

5. H. Morawetz, Macromolecules in Solution, Wiley-Interscience, New York (1965).

6a. P. J. Flory, Principles of Polymer Chemistry, Cornell Univ. Press, Ithica, New York (1953).

b. P. J. Flory, J. Chem. Phys., 9, 660 (1941).

c. P. J. Flory, J. Chem. Phys., 10, 51 (1941).

d. P. J. Flory, J. Chem. Phys., 12, 425 (1944).

7a. M. L. Huggins, J. Chem. Phys., 9, 440 (1941).

b. M. L. Huggins, Ann. New York Acad. Sci., 43, 1 (1942).

8a. R. L. Scott and M. Magat, J. Chem. Phys., 13, 172 (1945).

b. R. L. Scott, J. Chem. Phys., 13, 178 (1945).

c. R. L. Scott, J. Chem. Phys., 17, 268, 279 (1949).

d. R. L. Scott, J. Polym. Sci., 4, 555 (1949).

e. R. L. Scott, J. Polym. Sci., 9, 423 (1953).

9. L. Rebenfeld, P. J. Makarewicz, H. D. Weigmann and G. L. Wilkes, J. Macromol. Sci., Rev. Macromol. Chem., C15, 279 (1976).

10. S. Krause, J. Macromol. Sci., Rev. Macromol. Chem., C11, 251 (1972).

11. A. F. M. Barton, Chem. Revs., 75, 731 (1975).

12. J. L. Gardon, Encycl. Polym. Sci. Technol., 3, 833 (1965).

13. F. W. Harris and R. B. Seymour, Eds., Structure-Solubility Relationships in Polymers, Academic Press, New York (1977).

14. G. Scatchard, Chem. Revs., 8, 321 (1931).

15. J. H. Hildebrand, J. Am. Chem. Soc., 51, 69 (1929).

16. C. Tanford, Physical Chemistry of Macromolecules, Chapter 3, pp. 180-274, John Wiley and Sons, New York (1961).

17. O. K. Rice, Statistical Mechanics, Thermodynamics, and Kinetics, Chapter 12, pp. 270-314, W. H. Freeman Co., San Francisco (1967).

18. P. A. Small, J. Appl. Chem., 3, 71 (1953).

19. K. L. Hoy, J. Paint Technol., 42, 76 (1970).

20. C. M. Hansen, J. Paint Technol., 39, 104 (1967).

21. J. L. Gardon, J. Paint Technol., 38, 43 (1968).

22. E. B. Bagley and J. M. Scigliano, in Solutions and Solubilities, Part II (M. R. J. Dack, Ed.), Chapter 16, pp. 437-485, John Wiley, New York (1976).

23. M. T. Shaw, J. Appl. Polym. Sci., 18, 449 (1974).

24a. R. S. Drago, L. B. Parr and C. S. Chamberlain, J. Am. Chem. Soc., 99, 3203 (1977).

b. R. S. Drago, G. C. Vogel and E. Needham, J. Am. Chem. Soc., 93, 6014 (1971).

25. F. M. Fowkes and M. A. Mostafa, Ind. Eng. Chem., 17, 3 (1978).

26. F. E. Bailey, R. D. Lundberg and R. W. Callard, J. Polym. Sci. Pt. A, 2, 845 (1964).

27. J. W. Schurer, A. de Boer and G. Challa, Polym., 16, 201 (1975).

28. J. V. Koleske and R. D. Lundberg, J. Polym. Sci. Pt. A, 7, 795 (1969).

29. J. S. Noland, N. N. Hsu, R. Saxton and J. M. Schmitt, Polym. Prepr., Amer. Chem. Soc., Div. Polym. Chem., 11, 355 (1970).

30. D. M. Koenhen and C. A. Smolders, J. Appl. Polym. Sci., 19, 1163 (1975).

31. J. S. Rowlinson and P. L. Freeman, Polym. 1, 20 (1960).

32. P. Ehrlich, J. Polym. Sci. Pt. A, 3, 131 (1965).

33a. A. A. Tager, Vysokomol. Soyed., A14, 3122 (1972), translated in Polym. Sci. (USSR), 14, 3129 (1972).

b. A. A. Tager, L. V. Adamova, V. V. Serpinskii and M. V. Tsilipotkina, Vysokomol. Soyed., A16, 203 (1974), translated in Polym. Sci. (USSR), 16, 240 (1974).

c. L. V. Andreyev, A. A. Tager, I. S. Fominykh and O. L. Zamayeva, Vysokomol. Soyed., A18, 286 (1976), translated in Polym. Sci. (USSR), 18, 328 (1976).

34a. M. Bank, J. Leffingwell and C. Thies, J. Polym. Sci. Pt. A, 10, 1097 (1972).

b. M. Bank, J. Leffingwell and C. Thies, Macromol., 4, 44 (1971).

35a. T. Nishi and T. K. Kwei, Polym., 16, 185 (1975).

b. T. Nishi, T. K. Kwei and R. F. Roberts, Macromol., 7, 60 (1974).

c. T. Nishi, T. K. Kwei and T. T. Wang, Macromol., 8, 227 (1975).

36a. P. J. Flory, J. Am. Chem. Soc., 87, 1833 (1965).

b. P. J. Flory, Trans. Faraday Soc., 49, 7 (1970).

c. P. J. Flory, J. L. Ellenson and B. F. Eishinger, Macromol., 1, 279 (1968).

d. P. J. Flory, H. Hocker and G. T. Blake, Trans. Faraday Soc., 67, 2251, 2275 (1971).

e. P. J. Flory and H. Shih, Macromol., 5, 758, 761 (1972).

37a. I. C. Sanchez, to be published.

b. I. C. Sanchez and R. H. Lacombe, Nature, 252, 381 (1974).

c. I. C. Sanchez and R. H. Lacombe, J. Chem. Phys., 80, 2352, 2568 (1976).

38. J. G. Curro, J. Macromol. Sci., Rev. Macromol. Chem., C11, 321 (1974).

39. J. C. Slater, Introduction to Chemical Physics, Dover, New York (1960).

40. T. H. Hill, Introduction to Statistical Thermodynamics, McGraw Hill, New York (1960).

41a. D. C. Bonner, J. Macromol. Sci., Rev. Macromol. Chem., C13, 263 (1973).

b. D. C. Bonner and J. M. Prausnitz, J. Polym. Sci., Polym. Phys. Ed., 12, 51 (1974).

c. D. C. Bonner, E. R. Bazcia and J. M. Prausnitz, Ind. Eng. Chem. Fund., 12, 254 (1973).

42a. L. P. McMasters, Macromol., 6, 760 (1973).

b. L. P. McMasters, Polym. Prepr., Amer. Chem. Soc., Div. Polym. Chem., 15, 254 (1974).

43a. D. Patterson, Macromol., 2, 672 (1969).

b. D. Patterson, J. Paint Technol., 45, 37 (1973).

44. S. Kanno, S. Saeki, N. Kuwahara, M. Nakata and M. Kaneko, Macromol., 8, 799 (1975).

45. R. E. Bernstein, C. A. Cruz, D. R. Paul and J. W. Barlow, Macromol., 10, 681 (1977).

46a. R. Becker and W. Doring, Ann. Phys., 24, 719 (1935).

b. R. Becker, Ann. Phys., 32, 128 (1938).

47a. M. Volmer, Z. Physik. Chem., 102, 267 (1922).

b. M. Volmer and A. Weber, Z. Physik. Chem., 119, 222 (1925).

48a. D. Turnbull and J. C. Fischer, J. Chem. Phys., 17, 71 (1949).

b. D. Turnbull, J. Chem. Phys., 18, 198 (1950).

49. P. H. Till, J. Polym. Sci., 24, 301 (1957).

50. A. Keller, Phil. Mag., 2, 1171 (1957).

51. E. W. Fischer, Z. Naturforsch., 12, 753 (1957).

52a. A. Peterlin, J. Appl. Phys., 31, 1934 (1960).

52b. A. Peterlin and E. W. Fischer, Zeit. fur Physik., 159, 272 (1960).

c. A. Peterlin and C. Reinhold, J. Chem. Phys., 37, 1403 (1962).

53. J. I. Lauritzen and J. D. Hoffman, J. Res. Nat. Bur. Std., 64A, 73 (1960).

54a. F. P. Price, J. Polym. Sci., 31, 1934 (1960).

b. F. P. Price, J. Chem. Phys., 35, 1884 (1961).

55. F. C. Frank and M. Tosi, Proc. Roy. Soc., 263A, 323 (1961).

56a. L. Mandelkern, Crystallization of Polymers, McGraw Hill, New York (1964).

b. L. Mandelkern, Chem. Revs., 56, 903 (1956).

c. L. Mandelkern, Prog. Polym. Sci., 2, 165 (1970).

57. J. W. Christianson, The Theory of Transformation in Metals and Alloys part I: Equalibrium and General Kinetic Theory, 2nd. Ed., Pergamon Press, New York (1975).

58. B. Wunderlich, Macromolecular Physics, Vol. II, Academic Press, New York (1976).

59. F. P. Price, in Nucleation (A. C. Zettlemoyer, Ed.), Chapter 7, p. 405, Marcell Dekker, New York (1969).

60a. J. D. Hoffman and J. I. Lauritzen, Jr., J. Res. Nat. Bur. Std., 65A, 297 (1961).

b. J. D. Hoffman, S.P.E. Trans., 4, 1 (1964).

c. F. Gornick and J. D. Hoffman, Ind. Eng. Chem., 58, 41 (1966).

d. J. D. Hoffman, J. I. Lauritzen, Jr., E. Pascaglia, G. S. Ross, L. J. Frolen and J. J. Weeks, Kolloid. Z.Z. Polym., 231, 564 (1969).

60e. J. D. Hoffman, G. T. Davis and J. I. Lauritzen, Jr., in Treatise on Solid State Chemistry (N. J. Hannay, Ed.), Vol. III, Chapter 7, Plenum Press, New York (1976).

f. J. D. Hoffman and J. I. Lauritzen, Jr., J. Appl. Phys., 44, 4340 (1973).

g. J. D. Hoffman, L. J. Frolen, G. S. Ross and J. I. Lauritzen, Jr., J. Res. Nat. Bur. Std., 79A, 671 (1975).

61a. P. H. Lindenmeyer, J. Polym. Sci. Pt. C, 1, 5 (1963).

b. P. H. Lindenmeyer, in Frontiers in Material Science (L. F. Murr and O. Stein, Eds.), Marcel Dekker, New York (1976).

62. R. L. Parker, Solid State Phys., 25, 151 (1970).

63. J. H. MaGill, in Treatise on Material Science and Technology (J. M. Schultz, Ed.), Vol. 10A, Chapter 1, p. 1, Academic Press, New York (1977).

64a. I. C. Sanchez, J. Macromol. Sci., Rev. Macromol. Chem., C10, 113 (1974).

b. I. C. Sanchez, J. Polym. Sci. Symposium, 59, 1 (1977).

65a. E. A. DiMarzio, J. Chem. Phys., 47, 3451 (1967).

b. J. I. Lauritzen, Jr., E. A. DiMarzio and E. Passaglia, J. Chem. Phys., 45, 4444 (1966).

c. J. I. Lauritzen, Jr., E. A. DiMarzio and E. Passaglia, J. Res. Nat. Bur. Std., 71A, 245, 261 (1967).

66a. F. L. Binsbergin, Kolloid. Z.Z. Polym., 237, 3, 289 (1970).

b. F. L. Binsbergin, Kolloid. Z.Z. Polym., 238, 389 (1970).

c. F. L. Binsbergin, Thesis, University of Groningen (1969).

67a. H. G. Zachmann, Kolloid Z.Z. Polym., 189, 67 (1963).

b. H. G. Zachmann, Kolloid Z.Z. Polym., 231, 504 (1969).

c. H. G. Zachmann, Faserforschung u. Textiltechnik, 18, 95 (1967).

d. H. G. Zachmann, Pure Appl. Chem., 38, 79 (1974).

e. H. G. Zachmann, Angew. Makromol. Chem., 60-61, 249 (1977).

68. B. Wunderlich and A. Mehta, J. Polym. Sci. Polym. Phys. Ed., 12, 255 (1974).

69. S. Ahroni, J. Appl. Polym. Sci., 19, 1103 (1975).

70a. I. C. Sanchez and E. A. DiMarzio, J. Chem. Phys., 55, 893 (1971).

b. I. C. Sanchez and E. A. DiMarzio, Macromol., 6, 677 (1971).

c. I. C. Sanchez and E. A. DiMarzio, J. Res. Nat. Bur. Std., 76A, 213 (1972).

71. S. Glasstone, K. J. Laidler and H. Eyring, The Theory of Rate Processes, McGraw-Hill, New York (1941).

72. J. I. Lauritzen, Jr., J. Appl. Phys., 44, 4353 (1973).

73a. T. Nishi and T. T. Wang, Macromol., 10, 421 (1977).

b. T. K. Kwei, G. D. Patterson and T. T. Wang, Macromol., 9, 780 (1976).

74. P. J. Flory, J. Chem. Phys., 17, 223 (1949).

75. P. J. Flory, L. Mandelkern and H. K. Hall, J. Am. Chem. Soc., 73, 2532 (1951).

76. A. M. Bueche, J. Am. Chem. Soc., 74, 65 (1952).

77a. D. R. Paul and J. D. Altamirano, Am. Chem. Soc. Adv. Chem. Ser., 142, 37 (1975).

77b. F. L. Imken, D. R. Paul and J. W. Barlow, Polym. Eng. Sci., 16, 504 (1976).

78. H. Bergmans and N. Overberger, J. Polym. Sci. Polym. Phys. Ed., 15, 1757 (1977).

79. M. Takayanagi, Pure Appl. Chem., 23, 151 (1970).

80a. W. Wenig, F. E. Karasz and W. J. MacKnight, J. Appl. Phys., 46, 4194 (1975).

b. R. Hammel, W. J. MacKnight and F. E. Karasz, J. Appl. Phys., 46, 4199 (1975).

81. E. Ergoz and L. Mandelkern, J. Polym. Sci. Polym. Letts. Ed., 11, 73 (1973).

82. M. Inoue, J. Polym. Sci., 51, Issue 156, S18 (1961).

83. E. Riande and J. M. G. Gatou, Polym., 17, 795 (1976).

84. J. D. Hoffman and J. J. Weeks, J. Res. Nat. Bur. Stds., 66A, 13 (1962).

85. J. Boon and J. M. Azoue, J. Polym. Sci., 6, 885 (1968).

86. L. M. Robeson, J. Appl. Polym. Sci., 17, 3607 (1973).

87. D. J. Blundell and A. Keller, J. Polym. Sci. Pt. B., 6, 433 (1968).

88a. M. Cooper and R. St. J. Manley, Macromol., 8, 219 (1975).

b. M. Cooper and R. St. J. Manley, Colloid Polym. Sci., 254, 542 (1976).

89a. H. D. Keith and F. J. Padden, Jr., J. Appl. Phys., 34, 2409 (1963).

89b. H. D. Keith and F. J. Padden, Jr., J. Appl. Phys., 35, 1270, 1286 (1964).

90. G. S. Y. Yeh and S. L. Lambert, J. Polym. Sci. Pt. A2, 10, 1183 (1972).

91. T. G. Gox, S. Gratch and S. Loshaek, in Rheology Theory and Applications (F. R. Eirich, Ed.), Vol. I, Chapter 12, p. 431, Academic Press, New York (1956).

92. M. Shen and A. Eisenberg, Rubb. Chem. Technol., 43, 95, 156 (1970).

93a. J. H. MaGill and R. J. Greet, J. Phys. Chem., 71, 1649 (1967).

b. J. H. MaGill and D. J. Plazek, J. Chem. Phys., 46, 3757 (1967).

c. J. H. MaGill and A. Gandica, Polym., 13, 595 (1972).

d. J. H. MaGill, A. Gandica and H. M. Li, Jr. Crystal Growth, 19, 361 (1973).

94. G. S. Ross and L. J. Frolen, J. Res. Nat. Bur. Std., 79A, 701 (1975).

95. T. Suzuki and A. J. Kovacs, Polym. J., 1, 82 (1970).

96. M. Gordon and J. D. Taylor, J. Appl. Chem., 2, 1 (1952).

97. N. Johnston, J. Macromol. Sci., Rev. Macromol. Chem., C14, 215 (1976).

98. F. N. Kelley and F. Bueche, J. Polym. Sci., 50, 549 (1961).

99. W. M. Prest and R. S. Porter, J. Polym. Sci. Polym. Phys. Ed., 10, 1639 (1972).

100a. M. Avrami, J. Chem. Phys., 7, 1103 (1939).

b. M. Avrami, J. Chem. Phys., 8, 212 (1940).

100c. M. Avrami, J. Chem. Phys., 9, 177 (1941).

101. U. R. Evans, Trans. Faraday Soc., 41, 365 (1945).

102a. L. Mandelkern, F. A. Quinn and P. J. Flory, J. Appl. Phys., 25, 830 (1954).

b. L. Mandelkern, J. Appl. Phys., 26, 443 (1955).

c. F. Gornick and L. Mandelkern, J. Appl. Phys., 33, 907 (1962).

103. L. B. Morgan, Proc. Roy. Soc., A247, 13 (1954).

104a. F. P. Price, Encycl. Polym. Sci. Technol., 3, 63 (1965).

b. F. P. Price, J. Appl. Phys., 36, 3014 (1965).

105a. W. Banks, A. Sharples and N. J. Hay, J. Polym. Sci. Pt. A., 2, 4059 (1964).

b. W. Banks, A. Sharples and N. J. Hay, Makromol. Chem., 59, 233 (1963).

106. R. S. Stein and J. Powers, O.N.R. Technical Report #31.

107a. Yu. K. Godovskii, N. M. Garbar and G. L. Slominskii, Vysokomol. Soyed., A14, 1833 (1972), translated in Polym. Sci. (USSR), 14, 1108 (1972).

b. Yu. K. Godovskii, N. M. Garbar and G. L. Slominskii, J. Polym. Sci. Polym. Phys. Ed., 12, 1053 (1974).

108. I. H. Hillier, J. Polym. Sci. Pt. A2, 4, 1 (1966).

109. N. J. Hay, J. Polym. Sci. Polym. Letts. Ed., 14, 549 (1976).

110a. M. C. Tobin, J. Polym. Sci. Polym. Phys. Ed., 12, 399 (1974).

b. M. C. Tobin, J. Polym. Sci. Polym. Phys. Ed., 14, 2253 (1976).

111a. A. Keller, M. T. P. International Revs. of Science, Macromol. Sci., Physical Chem. Series I, Vol. 8, 105 (1972).

111b. A. Keller, Kolloid Z.Z. Polym., 197, 98 (1964) and 231, 386 (1969).

c. A. Keller, Repts. Prog. in Phys., 31, 623 (1968).

112. R. Fava, J. Polym. Sci. Pt. D, Macromol. Rev., 5, 1 (1971).

113. F. P. Price, Records Chem. Prog., 22, 115 (1961).

114. D. A. Blackadder, J. Macromol. Sci., Rev. Macromol. Chem., C1, 297 (1967).

115. H. K. Livingston, Macromol., 2, 98 (1970).

116. F. Khoury and E. Passaglia, in Treatise on Solid State Chemistry (N. J. Hannay, Ed.), Vol. III, Chapter 6, Plenum Press, New York (1976).

117. B. Wunderlich, Macromolecular Physics, Vol. I, Academic Press, New York (1973).

118. P. H. Geil, Polymer Single Crystals, John Wiley and Sons, New York (1963).

119. H. D. Keith, in Physics and Chemistry of the Organic Solid State (D. Fox, M. M. Labes and A. Weissberger, Eds.), Chapter 8, Wiley-Interscience, New York (1963).

120. R. L. Miller, in Crystalline Olefin Polymers Pt. I (R. A. V. Raff and K. W. Doak, Eds.), Chapter 12, Wiley-Interscience, New York (1965).

121. T. Naono, J. Science Hiroshima Univ., 23A, 653 (1960).

122a. M. J. Nardini and F. P. Price, in Crystal Growth, the Proceedings of an International Conference, Pergamon Press, New York (1967).

122b. F. P. Price and R. W. Kilb, J. Polym. Sci., 57, 395 (1962).

123. A. J. Kovacs, B. Lotz and A. Keller, J. Macromol. Sci. Phys., B3, 385 (1969).

124. E. R. Walter and F. P. Reding, Abstracts of 133rd Mtng. of Am. Chem. Soc., San Francisco, p. 14R (1958).

125a. H. Tadokoro, Y. Chatani, T. Yoshiharo, S. Tahara and S. Murahashi, Makromol. Chem., 73, 109 (1964).

b. H. Tadokoro, J. Polym. Sci. Sumposium, 15, 1 (1966).

c. H. Tadokoro and Y. Takahashi, Macromol., 6, 672 (1973).

126. R. L. Miller, in Polymer Handbook (J. Brandrup and E. H. Immergut, Eds.), Wiley-Interscience, New York (1975).

127a. F. J. Balta-Calleja and A. Keller, J. Polym. Sci. Pt. A, 2, 2171 (1964).

b. F. J. Balta-Calleja, I. L. Hay and A. Keller, Kolloid Z.Z. Polym., 209, 128 (1966).

128. B. Lotz, A. J. Kovacs, G. A. Bassett and A. Keller, Kolloid Z.Z. Polym., 209, 115 (1966).

129a. A. J. Kovacs and A. Gonthier, Kolloid Z.Z. Polym., 250, 530 (1972).

b. A. J. Kovacs, A. Gonthier and C. Straupe, J. Polym. Sci. Symposium, 50, 283 (1975).

c. A. J. Kovacs, A. Gonthier and C. Straupe, J. Polym. Sci. Symposium, 59, 31 (1977).

130a. C. Booth, J. M. Bruce and M. Buggy, Polym., 13, 472 (1972).

b. M. J. Fraser, A. Marshall and C. Booth, Polym., 18, 93 (1977).

131. A. Keller, in Growth and Perfection of Crystals (R. H. Doremus, B. W. Roberts and D. Turnbull, Eds.), John Wiley and Sons, New York (1958).

132a. F. Khoury, J. Res. Nat. Bur. Std., 70A, 29 (1966).

b. F. Khoury and J. D. Barnes, J. Res. Nat. Bur. Std., 76A, 255 (1972).

c. F. Khoury and J. D. Barnes, J. Res. Nat. Bur. Std., 78A, 95, 363 (1974).

133. R. Eppe, E. W. Fischer and H. A. Stuart, J. Polym. Sci., 34, 721 (1959).

134. W. J. Barnes and F. P. Price, Polym., 5, 283 (1964).

135. B. Wunderlich and P. Sullivan, J. Polym. Sci., 61, 195 (1962).

136a. S. Mitsuhashi and A. Keller, Polym., 2, 109 (1961).

b. D. C. Bassett, A. Keller and S. Mitsuhashi, J. Polym. Sci. Pt. A1, 1, 763 (1963).

137. B. Lotz, A. J. Kovacs and J. C. Whittmann, J. Polym. Sci. Polym. Phys. Ed., 13, 909 (1975).

138. H. Staudinger and R. Signer, Z. Krist., 70, 193 (1929).

139. A. Keller, J. Polym. Sci., 39, 151 (1959).

140. J. D. Keith and F. J. Padden, Jr., J. Polym. Sci., 39, 101 (1959).

141. F. P. Price, J. Polym. Sci., 39, 139 (1959).

142a. H. D. Keith, F. J. Padden, Jr. and R. G. Vadimsky, J. Appl. Phys., 42, 4585 (1971).

142b. H. D. Keith, F. J. Padden, Jr. and R. G. Vadimsky, J. Polym. Sci. Pt. A2, 4, 267 (1967).

143. Y. Shimura and T. Hatakeyama, J. Polym. Sci. Polym. Phys. Ed., 13, 653 (1975).

144. A. E. Skoulios, in Block and Graft Copolymers (J. J. Burke and V. Weiss, Eds.), Chapter 7, p. 121, Syracuse Univ. Press, Syracuse, New York (1973).

145. R. G. Crystal, J. J. O'Malley and P. F. Erhardt, in Block Copolymers (S. L. Aggerwal, Ed.), pp. 163-195, Plenum Press, New York (1970).

146. A. Thierry and A. Skoulios, Makromol. Chem., 177, 319, 567 (1976).

147. M. Tomoi, Y. Shibayama and H. Katiuchi, Polym. J., 8, 190 (1976).

148. N. J. Burlant and A. S. Hoffman, Block and Graft Polymers, Reinhold, New York (1960).

149. H. W. Steinman, Polym. Prepr., Amer. Chem. Soc., Div. Polym. Chem., 11, 285 (1970).

150. G. M. Estes, S. L. Cooper and A. V. Tobolski, J. Macromol. Sci., Rev. Macromol. Chem., C4, 313 (1970).

151. E. Cuddihy, J. Moacanin and A. Rembaum, J. Appl. Polym. Sci., 9, 1285 (1965).

152. D. Margerison and G. C. East, Introduction to Polymer Chemistry, Chapter 2, pp. 101-118, Pergamon Press, New York (1967).

153. M. L. Huggins, J. Am. Chem. Soc., 64, 2716 (1942).

154. E. O. Kraemer, Ind. Eng. Chem., 30, 1200 (1938).

155. W. S. Dorn and D. D. McCracken, Numerical Methods with Fortran IV Case Studies, Chapter 7, pp. 310-352, John Wiley and Sons, New York (1972).

156. N. Hetherington, private communication.

157. M. Kurata and W. H. Stockmayer, Fortschr. Hochpolym. Forsch., 3, 196 (1963).

158. F. E. Bailey, J. L. Kucera and L. G. Imhof, J. Polym. Sci., 32, 517 (1958).

159. L. Mandelkern and P. J. Flory, J. Chem. Phys., 20, 212 (1952).

160. M. Kurata, Y. Tsunashima, M. Iwama and K. Kamada, in Polymer Handbook (J. Brandrup and E. H. Immergut, Eds.), Wiley-Interscience, New York (1975).

161. G. J. Johnstone, Masters Thesis, University of Waterlou (1972).

162. R. W. Lenz, Organic Chemistry of Synthetic High Polymers, Interscience, New York (1967).

163. W. A. Pryor, Introduction to Free Radical Chemistry, Chapters 3 and 9, Prentice-Hall, Englewood Cliffs, New Jersey (1966).

164. G. J. Howard, Kolloid Z.Z. Polym., 244, 213 (1971).

165. E. M. Chamot and C. W. Mason, Handbook of Chemical Microscopy, 3rd Ed., John Wiley and Sons, New York (1966).

166. E. E. Wahlstrom, Optical Crystallography, 4th Ed., Chapters 7 and 8, John Wiley and Sons, New York (1967).

167a. R. C. Jones, J. Opt. Soc. Am., 31, 488, 500 (1941).

b. H. Hurwitz, Jr. and R. C. Jones, J. Opt. Soc. Am., 31, 494 (1971).

168. W. A. Shurcliff and S. S. Ballard, Polarized Light, van Nostrand, Princeton, New Jersey (1964).

169. B. J. Abbs, Masters Thesis, University of Massachusetts (1974).

170. A. M. Chatterjee, Ph.D. Thesis, University of Massachusetts (1974).

171. O. W. Wells, Scanning Electron Microscopy, McGraw-Hill, New York (1974).

172a. S. Kimoto, JOEL News, 10e, 2 (1972).

b. S. Kimoto and J. C. Russ, Materials Res. and Stde., 9, 8 (1969).

173. J. V. Koleske and F. E. Bailey, Poly(ethylene oxide), Academic Press, New York (1976).

174. D. H. Kay, Ed., Techniques for Electron Microscopy, 2nd Ed., Blackwell Scientific Publications, Philadelphia, Pennsylvania (1965).

175. E. Thomas, notes from lectures presented at the University of Massachusetts (1976).

176. V. D. Philips, Modern Metallographic Techniques and Their Application, John Wiley and Sons, New York (1971).

177. R. S. Stein, in Newer Methods of Polymer Characterization (B. Ke, Ed.), Chapter 4, Interscience, New York (1964).

178. R. S. Stein, Rubber Chem. Technol., 49, 458 (1976).

179. M. B. Rhodes and R. S. Stein, Special Technical Publication #348 ASTM (1963).

180. R. S. Stein, to be published.

181. P. Debye and A. M. Bueche, J. Appl. Phys., 20, 378 (1949).

182. M. Goldstein and E. R. Michalik, J. Appl. Phys., 26, 1450 (1955).

183. R. S. Stein and P. R. Wilson, J. Appl. Phys., 33, 1914 (1962).

184. R. J. Clark, R. L. Miller, R. S. Stein and P. R. Wilson, J. Polymer. Sci., 42, 275 (1960).

185. R. S. Stein and G. L. Wilkes, in Structure and Properties of Oriented Polymers (I. M. Ward, Ed.), Chapter 3, Halsted Press, London (1975).

186. M. B. Rhodes, D. A. Keedy and R. S. Stein, J. Polym. Sci., 62, S73 (1962).

187. R. S. Stein and S. B. Clough, ONR Technical Rept. #67 (1963) and #75 (1965).

188. M. B. Rhodes and R. S. Stein, J. Polym. Sci. Pt. A2, 7, 1539 (1969).

189. A. Misra and R. S. Stein, J. Polym. Sci. Polym. Phys. Ed., 11, 109 (1973).

190. C. Picot and R. S. Stein, J. Polym. Sci. Pt. A2, 8, 1955, 2115 (1972).

191a. R. J. Samuels, J. Polym. Sci. Pt. A2, 9, 2165 (1971).

b. R. J. Samuels, J. Polym. Sci. Polym. Phys. Ed., 12, 1417 (1974).

192. C. J. Ong, Ph.D. Thesis, University of Massachusetts (1973).

193. A. Excala, E. Balazer and R. S. Stein, unpublished results.

194. R. S. Porter and J. F. Johnson, Eds., Analytical Calorimetry, Vol. 1-4, Plenum Press, New York (1976).

195. E. P. Manche and B. Carrol, in Physical Methods in Macromolecular Chemistry (B. Carrol, Ed.), Vol. 2, Chapter 4, Marcell Dekker, New York (1972).

196. W. W. Wendlandt, Thermal Methods of Analysis, Wiley-Interscience, New York (1974).

197. W. Wrasidlo, Adv. in Polym. Sci., 13, 1 (1974).

198. M. Dole, Fortschr. Hochpolym. Forsch., 2, 221 (1960).

199. Perkin-Elmer D.S.C. Instruction Manual, Norwalk, Connecticut (1972).

200. E. M. Barrall and J. F. Johnson, in Techniques and Methods of Polymer Evaluation (P. E. Slade and L. I. Jenkins, Eds.), Vol. 2, Chapter 2, Marcell Dekker, New York (1966).

201. J. H. Flynn, Thermochem. Acta., 8, 69 (1974).

202. C. M. Guttman and J. H. Flynn, Anal. Chem., 45, 408 (1973).

203. L. Mandelkern in ref. 56b.

204. D. R. Beech and C. Booth, Polym. Letts., 8, 731 (1970).

205. N. J. Hay, Macromol. Chem., 177, 2559 (1976).

206. J. J. Aklonis, W. J. MacKnight and M. Shen, Introduction to Polymer Viscoelasticity, Wiley-Interscience, New York (1972).

207. M. L. Miller, The Structure of Polymers, Chapter 6, Reinhold, New York (1968).

208. A. M. North, M.T.P. International Revs. of Science, Macromol. Sci., Physical Chem. Series II, Vol. 8, 136 (1975).

209. G. P. Koo, Plast. Eng., 30, 33 (1974).

210. L. E. Nielson, Mechanical Properties of Polymers and Composites, Vols. 1 and 2, Marcell Dekker, New York (1974).

211. J. D. Ferry, Viscoelastic Properties of Polymers, 2nd Ed., John Wiley and Sons, New York (1970).

212. R. Christensen, Notes from viscoelasticity lectures presented at Lawrence Livermore Laboratories, Livermore, California (1976).

213. N. G. McCrum, B. E. Read and G. Williams, Anaelastic and Dielectric Effects in Polymeric Solids, John Wiley and Sons, New York (1967).

214. F. Bueche, J. Chem. Phys., 30, 748 (1959).

215. P. E. Rouse, J. Chem. Phys., 21, 1272 (1953).

216. B. H. Zimm, J. Chem. Phys., 24, 269 (1956).

217. M. C. Williams, A.I.Ch. E. J., 21, 1 (1975).

218. Rheovibron Instruction Manual #17, Toyo Measuring Instruments Co., Tokyo, Japan (1969).

219. A. F. Yee and M. T. Takemori, J. Appl. Polym. Sci., 21, 2597 (1977).

220. M. L. Williams, R. F. Landel and J. D. Ferry, J. Am. Chem. Soc., 77, 3701 (1955).

221. T. G. Fox, Bull. Am. Phys. Soc., 1, 123 (1956).

222. S. L. Rosen, Polym. Eng. Sci., 7, 115 (1967).

223. T. Pakula, M. Kryszewski, J. Grebowicz and A. Galeski, Polym. J., 6, 94 (1974).

224a. M. Takayanagi, Pure Appl. Chem., 15, 555 (1967).

b. M. Takayanagi, Manuscript from general lecture presented at the International Symposium on Macromolecular Chemistry, Tokyo and Kyoto, Japan (1966).

225. R. G. C. Arridge, Mechanics of Polymers, Clarendon Press, Oxford (1975).

226. R. S. Stein, F. B. Khambatta, F. B. Warner and T. Russell, J. Polym. Sci. Polym. Phys. Ed., 14, 1391 (1976).

227. R. Nira, Ph.D. Thesis, University of Massachusetts (1975).

228. J. Barton and J. Rak, J. Appl. Polym. Sci., 11, 499 (1967).

229. M. Natov, L. Peeva and E. Djagarov, J. Polym. Sci. Pt. C, 16, 4197 (1968).

230a. L. Bohn, in Polymer Handbook (J. Brandrup and E. M. Immergut, Eds.), John Wiley and Sons, New York (1975).

b. L. Bohn, Rubb. Chem. Technol., 41, 495 (1968).

231. S. Tolansky, Multiple-Beam Interferometry of Surfaces and Films, Dover, New York (1970).

232. P. H. Geil and D. H. Reneker, J. Polym. Sci., 51, 569 (1961).

233. S. Matsuoka, J. Appl. Phys., 32, 2334 (1961).

234. E. Jenckel and H. U. Herwig, Kolloid Z.Z. Polym., 148, 57 (1956).

235a. R. F. Boyer, J. Polym. Sci. Symposium, 50, 189 (1975).

b. R. F. Boyer, Polym., 17, 996 (1976).

236. G. T. Davis and R. K. Eby, J. Appl. Phys., 44, 4274 (1973).

237. K. Sanni, W. J. MacKnight and R. W. Lenz, Macromol., 7, 101 (1974).

238. Yu. K. Godovski, G. L. Slonimskii and N. M. Garbar, Vysokomol. Soedin., A15, 813 (1973), translated in Polym. Sci. (USSR), 15, 914 (1973).

239. E. Alfthan and A. de Ruvo, Polym., 16, 692 (1975).

240a. N. G. McCrum, B. E. Read and G. Williams, Chapter 14 in ref. 213.

b. N. G. McCrum, J. Polym. Sci., 54, 561 (1961).

c. B. E. Read, Polym., 3, 529 (1962).

d. T. M. Connor, B. E. Read and G. Williams, J. Appl. Chem., 14, 74 (1964).

241. J. A. Faucher, J. V. Koleske, E. R. Santee, Jr., J. J. Statta and C. W. Wilson, J. Appl. Phys., 37, 3962 (1966).

242. K. Anisawa, K. Tsuge and Y. Wada, Jap. J. Appl. Phys., 4, 138 (1965).

243. C. H. Porter and R. H. Boyd, Macromol., 4, 589 (1971).

244. R. W. Wetton and G. Allen, Polym., 7, 331 (1966).

245. M. C. Lang, C. Noël and A. P. Legrand, J. Polym. Sci. Polym. Phys. Ed., 15, 1319, 1329 (1977).

246. J. B. Enns and R. Simha, J. Macromol. Sci. Phys., 13, 25 (1977).

247. F. P. Price, Short communication 1 B2, Symposium IUPAC, Wiesbaden, Germany (1959), in ref. 129a.

248. L. Mandelkern, J. Polym. Sci. Symposium, 50, 457 (1977).

249. S. S. Rogers and L. Mandelkern, J. Am. Chem. Soc., 61, 985 (1957).

250. K. Deutsch, E. A. W. Hoff and W. Reddish, J. Polym. Sci., 13, 565 (1954).

251. N. G. McCrum, B. E. Read and G. Williams, Chapter 8 in ref. 213.

252. Y. Ishida, M. Matsuo and M. Takayanagi, J. Polym. Sci. Pt. B, 3, 321 (1965).

253. W. J. MacKnight and A. V. Tobolsky, Polymeric Sulfur and Related Polymers, Chapter 3, pp. 35-51, Interscience, New York (1965).

254. V. K. Schmieder and K. Wolf, Kolloid Z.Z. Polym., 134, 149 (1953).

255a. J. Heijboer, Intern. J. Polymeric Mater., 6, 11 (1977).

b. J. Heijboer, Ann. New York Acad. Sci., 279, 104 (1976).

256. T. G. Fox and P. J. Flory, J. Appl. Phys., 21, 581 (1950).

257. E. B. Wilusz, Ph.D. Thesis, University of Massachusetts (1976).

258. T. Murayama, Dynamic Mechanical Analysis of Polymeric Materials, Elsevier, New York (1978).

259a. T. Nishi and T. T. Wang, Macromol., 8, 909 (1975).

b. T. Nishi, T. K. Kwei and T. T. Wang, J. Appl. Phys., 46, 4157 (1975).

260. I. C. Sanchez, A. Peterlin, R. K. Eby and F. L. McCrakin, J. Appl. Phys., 4216 (1974).

261a. E. W. Fischer, H. Goddar and G. F. Schmidt, J. Polym. Sci. Pt. B, 5, 619 (1967).

b. E. W. Fischer, Pure Appl. Chem., 31, 113 (1972).

262. B. Lotz and A. J. Kovacs, Polym. Prepr., Amer. Chem. Soc., Div. Polym. Chem., 10, 821 (1969).

263. F. C. Frank, Proc. Roy. Soc., A201, 586 (1950).

264. E. Martuscelli and E. Scafora, La Chimica e. L'Industria (Milan), 58, 601 (1976).

265. F. P. Price, W. J. Barnes and W. G. Leutzel, J. Chem. Phys., 65, 1742 (1961).

266a. N. J. Jain and F. L. Swinton, Eur. Polym. J., 3, 371, 379 (1967).

b. N. J. Jain, Indian J. Technol., 7, 123 (1969).

267a. N. J. Hay, M. Sabir and R. L. T. Steven, Polym., 10, 187 (1969).

b. N. J. Hay and M. Sabir, Polym., 10, 203 (1969).

268. M. A. Asaubekov, N. P. Krasikova and V. A. Kargin, Vysokomol. Soedin., A14, 30 (1972).

269. P. K. Seow, Y. Gallot and A. Skoulios, Makromol. Chem., 177, 177 (1976).

270. C. Decker, J. Polym. Sci. Polym. Chem. Ed., 15, 781, 799 (1977).

271. A. M. Afifi-Effat and N. J. Hay, Eur. Polym. J., 8, 289 (1972).

272. L. Reich and S. S. Stivala, J. Appl. Polym. Sci., 13, 977 (1969).

273. J. D. Hoffman and J. J. Weeks, J. Chem. Phys., 37, 1723 (1962).

274. Y. Yamashita, P. Yokoyama and K. Monobe, Memoirs School of Eng., Okayama Univ., 1, 59 (1966).

275. J. D. Hoffman and G. T. Davis, J. Res. Nat. Bur. Std., 79A, 613 (1975).

276. P. Meares, Polymer Structure and Bulk Properties, Chapters 4 and 5, D. van Nostrand, New York (1965).

277. Proverbs 25:2.

FIGURE CAPTIONS

Figure 1 The Gibbs' free energy of mixing calculated from equation (5) with the degree of polymerization, $x_1 = x_2$, taken as 10^5 and allowing χ_{12} to increase from zero to 5×10^{-5} exhibits one minimum up until χ_{12} reaches its critical value. As χ_{12} increases above its critical value, two mimima develop indicating phase separation. For $\chi_{12} \geq 5 \times 10^{-5}$ the Gibbs' free energy is almost entirely concave upward and positive indicating that two polymers with this very small positive interaction would be almost totally immiscible.

Figure 2 A temperature-composition diagram can be calculated from the equilibrium conditions, equation (8), if the temperature dependence of χ_{12} is known. Assuming $x_1 = x_2$ the binodal equation is $\chi_{12} = 1/(1 - 2\phi_1) \ln (\phi_1/1 - \phi_1)$ and the spinodal equation is $1/\chi_{12}x = 2\phi_1\phi_2$. For the same conditions as in figure 1, these equations are plotted as $1/\chi_{12}$ versus ϕ_1. If the solubility parameters and the reference volume are independent of temperature, equation (4) implies an inverse temperature dependence of χ_{12}. We have arbitrarily assumed $\Delta\delta^2 = 0.0012$ cal/cc and $V_r = 1$.

Figure 3 Equation of state theories of mixtures are capable of predicting both upper (UCST) and lower (LCST) critical solution temperatures in liquid-liquid phase diagrams (after reference 37c).

Figure 4 The theoretical melting point depression for PEO equilibrium crystals in high molecular weight $X_2 = 10^5$, (—•—•) and low molecular weight, $X_2 = 1$, diluent (—) with different interaction parameters calculated from equation (39). Values of T_m^o and ΔH_f were taken from Table III of Chapter III. When phase separation occurs in the liquid, the melting point does not increase but remains constant over the immiscible composition range as indicated by the dashed lines.

Figure 5 The theoretical growth rates for blends with $\chi_{12} = 0$ (—) and $\chi_{12} = -3.0$ (—•—•—•—) remain experimentally distinguishable only at high diluent concentrations. The growth rates for PEO/high molecular weight diluent mixtures were calculated from equation (45) using the values in Table III of Chapter III; assuming T_∞ followed Fox's equation (44) and replacing T_m^o with T_d^o from equation (40) when χ_{12} is negative. The percent PEO in the blend is indicated at the upper left of every other set of G_r curves.

Figure 6 The unit cell of PEO based on references 125 and 127.

Figure 7 (a) Schematic of the stages of spherulitic growth: single crystals become multilayered lamellae which then fibrillate and become sheaf-like and finally close on themselves to form a spherulite.
(b) Transmission electron micrograph of a surface replica of a PEO spherulite reveals lamellar fine structure when the specimen is shadowed with chromium at a 5 degree angle. The bar length is 1μ.

Figure 8 Determination of the viscosity average molecular weight from intrinsic viscosity measurements by extrapolation of the relative and specific viscosities to zero concentration of WSR-N-3000 PEO in water at $30^{o}C$. $[\eta] = 2.98$; Mol. wt. = 4.1×10^{5}; concentration in grams per deciliter.

Figure 9 Determination of the viscosity average molecular weight from intrinsic viscosity measurements of Carbowax 6000 in water at $30^{o}C$. $[\eta] = 0.16$; Mol.wt. = 9.63×10^{3}.

Figure 10 Determination of the viscosity average molecular weight from intrinsic viscosity measurements of poly (methyl-methacrylate) obtained from Cellomer Associations in acetone at $25^{o}C$. $[\eta] = 0.575$; Mol.wt. = 3.34×10^{5}.

Figure 11 A schematic diagram of the polymerization set up for free radical polmerization of methyl metacrylate monomer mixed with Carbowax C-6000. The mixture is frozen in liquid nitrogen, sealed under vacuum, and then heated to $80^{o}C$ to activate the free radical initiator and polymerize the monomer.

Figure 12 The optical microscopic set up used for isothermal spherulite growth rate measurements consisted of: (a) the Mettler FP-2 hot stage, (b) Zeiss optical microscope, (c) automatic shutter and motorized film back, (d) "Robot" 35 mm camera, (e) 200 foot film cassette, (f) Mettler FP-2 hot stage controller, (g) Sorvall low temperature controller, (h) liquid nitrogen dewar, and (i) low temperature sensor position.

Figure 13 Calibration curve for the Mettler FP-2 hot stage. A plot of melting point of standard birefringent crystals versus observed loss of birefringence extrapolated to zero heating rate showed that the observed melting point was consistently 1 degree below the melting temperature of the standards.

Figure 14 Schematic representation of the small angle light scattering apparatus used in these experiments showing the scattering angles θ and μ. (After Samuels in reference 191.)

Figure 15 (a) Schematic representation of the Rheovibron sample including the stresses and strains involved.
(b) Diagram of Takayanagi's series model for crystalline and two-phase polymer after references 224 and 225.
(c) Diagram of Takayanagi's parallel model.

Figure 16 (a) The dynamic mechanical properties of different compositions of two glassy polymers calculated from equations (73) and (74) allowing T_g to vary according to equation (44). This hypothetical case demonstrates the variation in T_g with composition for a compatible blend without the influence of crystallization. (For further discussion, see text.)
(b) The dynamic mechanical properties of different compositions of an incompatible blend of two glassy polymers calculated from Takayanagi's series model (equation 76) with $\lambda = \phi$ = the weight fraction of lower T_g polymer (solid lines) or higher T_g polymer (dotted lines). This hypothetical case demonstrates that incompatible blends can be identified by the presence of two glass transition

temperatures that are independent of composition. (For further discussion, see text.)

Figure 17 The dynamic mechanical behavior of a compatible blend in which the low T_g component is capable of crystallizing. The degree of crystallinity affects the temperature at which T_g occurs and the relaxation strength because of the change in amorphous composition on crystallization. Based on DSC data from figures 25 and 43, the T_g of the amorphous phase in the crystalline blend goes through a maximum at 60 percent crystallizable polymer then a minimum at 50 percent then increases steadily with decreasing concentration of crystallizable material. The concentration of amorphous blend decreases continuously as the crystallinity increases. Depending on the percent crystallinity chosen for the 30 percent crystallizable polymer concentration, the glass transition shifts over a $35^{o}C$ temperature range as indicated by the arrows in the figure. (For further discussion, see text.)

Figure 18 Micrographs of glassy blends of PEO/PMMA 18/82: C6K/MMA. (a) Transmission electron micrograph (TEM); bar length 1μ; (b) scanning electron micrograph (SEM); bar length 10μ. Micrographs of non-impinging spherulites of PEO/PMMA 33/67: C6K/MMA blends; (c) SEM; bar length 10μ; (d) opti-

cal micrograph (OM); bar length 100μ; (e) Normarski interference micrograph showing refractive index or thickness variation around the spherulites.

Figure 19 Micrographs of rod-like crystals of PEO/PMMA 45/55: C6K/MMA. (a) SEM with bar length of 10μ crystallized at 45°C; (b) OM with bar length of 100μ crystallized at 40°C with a small angle light scattering pattern inserted in the lower right hand corner. Optical micrographs of a PEO/PMMA 50/50: WSR/HM blends; (c) between crossed polars annealed at 45°C for 6 weeks (d-k) using oblique illumination just after melting of the sample in figure 19c. These micrographs were taken once a minute as the temperature was increased at 10°C/min. Figure 19d was taken at approximately 70°C and so on until figure 19k at 140°C where the two polymers had completely coalesced. Redissolution of the two components is discussed in the text.

Figure 20 Micrographs of 100 percent WSR-N-3000 PEO crystallized at different temperatures.

	$T^{o}C$	Bar Length	Magnification	Type Micrograph
a.	$20^{o}C$	100μ	100X	SEM
b.	$15^{o}C$	100μ	100X	SEM
c.	$15^{o}C$	10μ	600X	SEM
d.	$10^{o}C$	10μ	300X	SEM
e.	$5^{o}C$	100μ	120X	SEM
f.	$0^{o}C$	100μ	50X	SEM

Figure 21 Micrographs of PEO/PMMA: 90/10: WSR/H$\bar{M}$ blends crystallized at different temperatures.

	$T^{o}C$	Bar Length	Magnification	Type Micrograph
a.	$45^{o}C$	100μ	30X	SEM
b.	$30^{o}C$	100μ	50X	OM
c.	$25^{o}C$	100μ	60X	SEM
d.	$20^{o}C$	100μ	110X	SEM
e.	$10^{o}C$	10μ	800X	SEM
f.	$5^{o}C$	100μ	80X	OM
g.	$0^{o}C$	10μ	1200X	SEM
h.	$-5^{o}C$	100μ	80X	OM

Figure 22 Micrographs of PEO/PMMA:80/20: WSR/HM blends crystallized at different temperatures.

	T°C	Bar Length	Magnification	Type Micrograph
a.	30°C	100μ	50X	OM
b.	20°C	10μ	300X	SEM
c.	15°C	100μ	80X	OM
d.	10°C	100μ	210X	SEM
e.	5°C	100μ	70X	SEM
f.	0°C	100μ	80X	OM
g.	-5°C	100μ	120X	SEM

Figure 23 Micrographs of PEO/PMMA:70/30: WSR/HM blends crystallized at different temperatures.

	T°C	Bar Length	Magnification	Type Micrograph
a.	25°C	100μ	50X	OM
b.	20°C	10μ	100X	SEM
c.	15°C	100μ	50X	OM
d.	10°C	100μ	210X	SEM
e.	5°C	100μ	80X	OM
f.	0°C	100μ	50X	OM
g.	-5°C	100μ	50X	OM

Figure 24 Micrographs of PEO/PMMA: 60/40: WSR/$H\bar{M}$ blends crystallized at different temperatures.

	$T^{o}C$	Bar Length	Magnification	Type Micrograph
a.	$40^{o}C$	100μ	150X	SEM
b.‡	$35^{o}C$	100μ	80X	SEM
c.‡	$30^{o}C$	10μ	100X	SEM
d.	$25^{o}C$	100μ	100X	SEM
e.*	$25^{o}C$	10μ	300X	SEM
f.‡	$5^{o}C$	10μ	700X	SEM
g.	$-5^{o}C$	100μ	80X	OM

Figure 25 The percent crystallinity of PEO in the blend versus the weight fraction of PEO. The percent crystallinity of the PEO was determined from the integral of the DSC melting endotherms of annealed blends using equation (66).

Figure 26 Plots of the melting point (T_m) of annealed PEO/PMMA blends, the onset of crystallization (T_c) in the DSC at a cooling rate of $20^{o}C$/min., and the glass transition (T_g) of the blends as a function of the weight fraction of PMMA.

Figure 27 The spherulite growth rate curves for PEO/PMMA: 90/10: WSR/H$\overline{M}$ blends at three different temperatures.

Figure 28 The spherulite growth rate curves for PEO/PMMA: 45/55: C6K/MMA blends at three different temperatures.

Figure 29 Spherulite growth rate curves from several polymerized samples of PEO/PMMA: 40/60: C6K/MMA blends crystallized isothermally at $40^{o}C$ and $30^{o}C$. Different samples are indicated by the various shapes of data points.

Figure 30 The spherulite growth rates of blends from 100 to 50 percent PEO in mm/min. versus $1/T\Delta T \times 10^{5o}K^{2}$ decrease with increasing high molecular weight diluent concentration.

Figure 31 The determination of K_g and ln G_o according to equation (45) from plots of ln $G_r + U/R(T-T_\infty)$ versus $1/T\Delta T$ for blends of (a) 100 percent PEO; (b) PEO/PMMA: 90/10: WSR/H$\overline{M}$; (c) PEO/PMMA: 80/20: WSR/H$\overline{M}$; (d) PEO/PMMA: 70/30: WSR/H$\overline{M}$; (e) PEO/PMMA: 60/40: WSR/H$\overline{M}$. All blends were solvent cast from warm acetone.

Figure 32 The determination of U and T_∞ from plots of $-[\ln(G/G_o) + K_g/T\Delta T]^{-1} \times 10^2$ versus T. The slope of the plot is U/R and the x-intercept is T_∞ according to equation (45).

Figure 33 Isothermal crystallization exotherms from DSC traces of blends of (a) 4.893 mg of 100 percent WSR-N-3000 PEO, (b) 4.71 mg of PEO/PMMA: 90/10: WSR/H$\overline{M}$, and (c) 3.203 mg of PEO/PMMA: 80/20: WSR/H$\overline{M}$ at different temperatures. The crystallization temperature is shown to the right of the corresponding exotherm.

Figure 34 Isothermal crystallization exotherms from DSC traces of blends of (a), (b) 5.463 mg of PEO/PMMA: 70/30: WSR/H$\overline{M}$ and (c), (d) 9.035 mg of PEO/PMMA: 60/40: WSR/H$\overline{M}$ at different temperatures. The crystallization temperature is shown to the right of the corresponding exotherm.

Figure 35 Avrami plots, the double log of the untransformed fraction of PEO as a function of the log of the time for blends of (a) 100 percent WSR-N-3000 PEO and (b) PEO/PMMA: 90/10: WSR/H$\overline{M}$ calculated from the DSC curves in figure 33.

Figure 36 Avrami plots, the double log of the untransformed fraction of PEO as a function of the log of the time for blends of (a) PEO/PMMA: 80/20: WSR/H$\overline{M}$ and (b) PEO/PMMA: 70/30: WSR/H$\overline{M}$ from the DSC curves in figures 33 and 34.

Figure 37 Avrami plots, the double log of the untransformed fraction of PEO as a function of the log of the time for blends of (a) PEO/PMMA: 70/30: WSR/H$\overline{M}$ and (b) PEO/PMMA: 60/40: WSR/H$\overline{M}$ from the DSC scans in figure 34.

Figure 38 The overall crystallization equivalent to the Fischer-Turnbull equation (45). The log of the crystallization half-time versus $1/T\Delta T \times 10^{5} {}^{o}K^{2}$.

Figure 39 The apparent number of nuclei calculated from the Avrami k value and the Fischer-Turnbull growth rate equation is plotted against $1/T\Delta T \times 10^{5}$. The nucleation density increased dramatically at high supercoolings in the 60 and 70 percent PEO blends. (For further discussion see text.)

Figure 40 DSC traces of the same PEO/PMMA: 60/40: WSR/H$\overline{M}$ with various thermal histories: (a) annealed at 45^{o}C for six weeks; brackets indicate change in sensitivity to

20 mCal/sec as the blend melting point is approached, (b) isothermally crystallized at 22°C prior to being scanned, and (c) quenched at 320°C/min to -100°C then scanned. All samples were scanned at 80°C/min and at a range of 5 mCal/sec.

Figure 41 (a) Model of quenched blends modified from that proposed by Mandelkern in reference 248. The modification allows atactic PMMA (—O—O—O—O—) to become entangled in the fold surface but remain mainly in the interzonal phase between crystals. (b) Model of annealed and isothermally crystallized blends based on a regular fold surface. Most PMMA is not entrapped in the folds but may adsorb on the crystal fold surface.

Figure 42 DSC traces of PEO/PMMA blends quenched at 320°C/min: (a) 100 percent PEO, (b) 90/10:PEO/PMMA, (c) 80/20: PEO/PMMA, (d) 70/30:PEO/PMMA. Arrows indicate the apparent glass transition for each blend. The heating rate was 80°C/min and sensitivity was 5 mCal/sec.

Figure 43 The variation in the glass transition of the amorphous phase of the PEO/PMMA blends with different degrees of crystallinity calculated from equation (78). The solid

line was calculated from the Fox equation (44) which is equivalent to equation (78) with $X_c = 0$, the $- + \text{——} + -$ line was calculated using X_c values from quenched blends, and the $-0-0-$ line using X_c values for annealed blends.

Figure 44 The tensile storage modulus in dynes/cm^2 for six blends of PEO/PMMA from 40/60 to 100 percent PMMA measured at 3.5 Hz over the temperature range from -150 to 150^{o}C. Arrows indicate the calculated T_g for the blends. The PEO/PMMA 40/60: WSR/H$\overline{M}$ blend (O) was shifted down 1 unit on the y axis, the PEO/PMMA:50/50: WSR/H$\overline{M}$ blend (□) was shifted down 2 units, and the PEO/PMMA:60/40: WSR/H$\overline{M}$ blend (▷) down 3 units.

Figure 45 The loss modulus in dynes/cm^2 for five blends from 60 to 20 percent PEO measured at 3.5 Hz over the temperature range from -150 to 100^{o}C. Arrows indicate the calculated T_g for the blends. The PEO/PMMA:20/80: WSR/H$\overline{M}$ blend was shifted up 2 units on the y-axis, the PEO/PMMA:30/70: WSR/H$\overline{M}$ blend was shifted up 1 unit, the PEO/PMMA:40/60: WSR/H$\overline{M}$ and PEO/PMMA:50/50: WSR/H$\overline{M}$ blends were not shifted and the PEO/PMMA:60/40: WSR/H$\overline{M}$ blend was shifted down 1 unit.

Figure 46 The tangent delta behavior for six blends from 40 to 100 percent PMMA measured at 3.5 Hz over the temperature range from -150 to 150^{o}C.

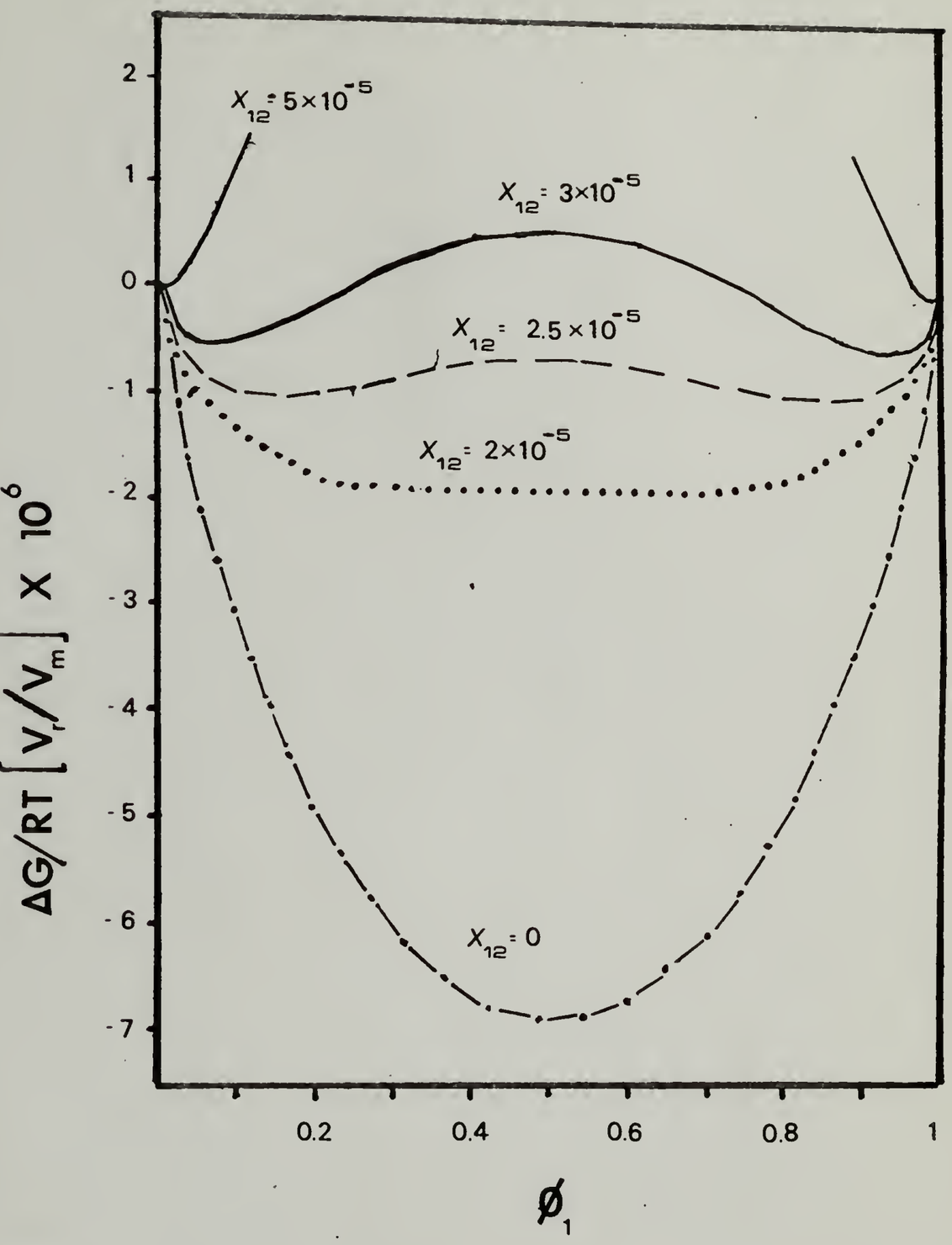
$X_{12} = 5\times10^{-5}$
$X_{12} = 3\times10^{-5}$
$X_{12} = 2.5\times10^{-5}$
$X_{12} = 2\times10^{-5}$
$X_{12} = 0$
2
1
0
-1
-2
-3
-4
-5
-6
-7
0.2
0.4
0.6
0.8
1
$\Delta G/RT \left[V_r/V_m\right] \times 10^6$
ϕ_1

figure 1

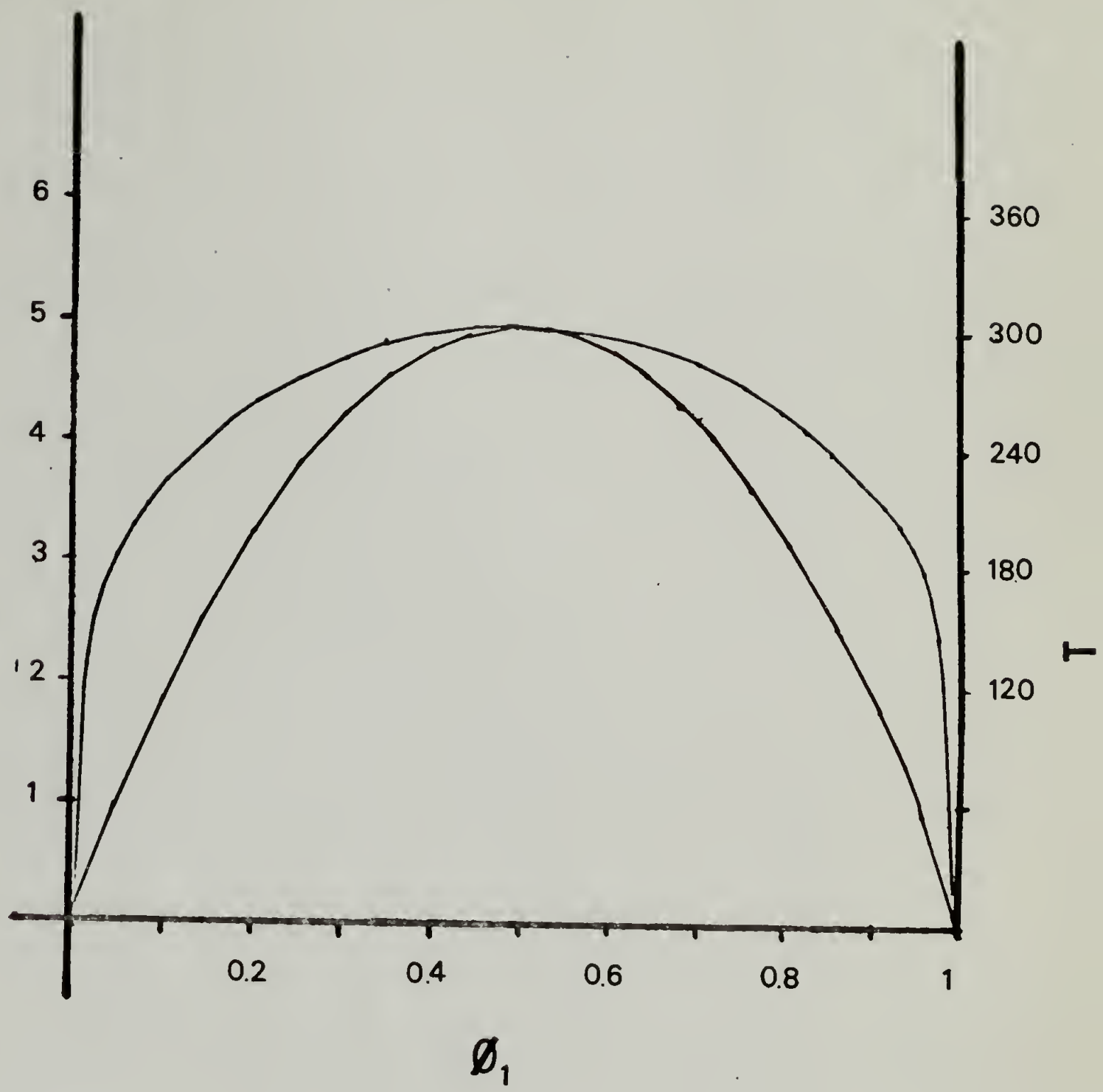

figure 2

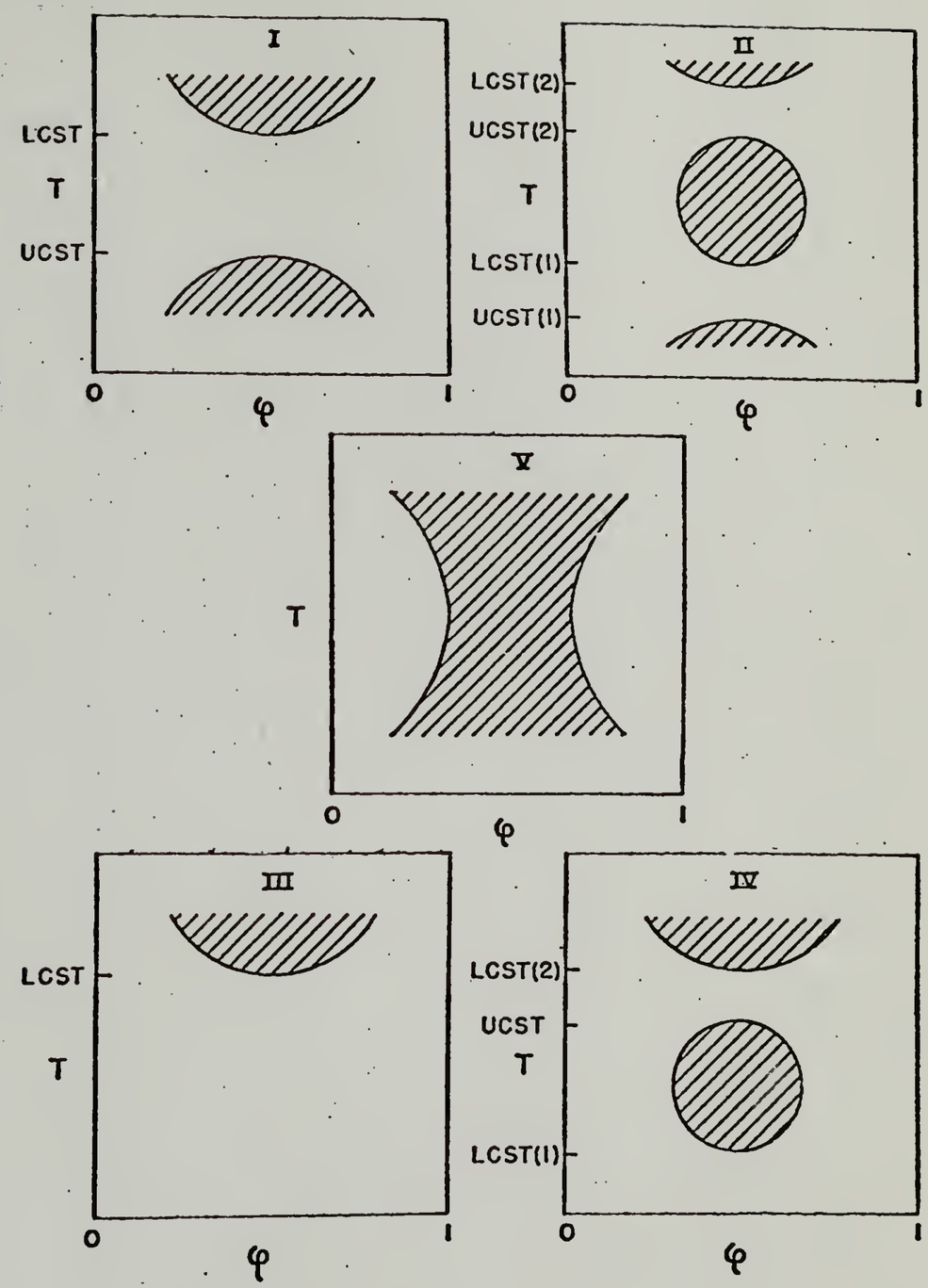
I
LCST
T
UCST
0
φ
1
II
LCST(2)
UCST(2)
T
LCST(1)
UCST(1)
0
φ
1
V
T
0
φ
1
III
LCST
T
0
φ
1
IV
LCST(2)
UCST
T
LCST(1)
0
φ
1

figure 3

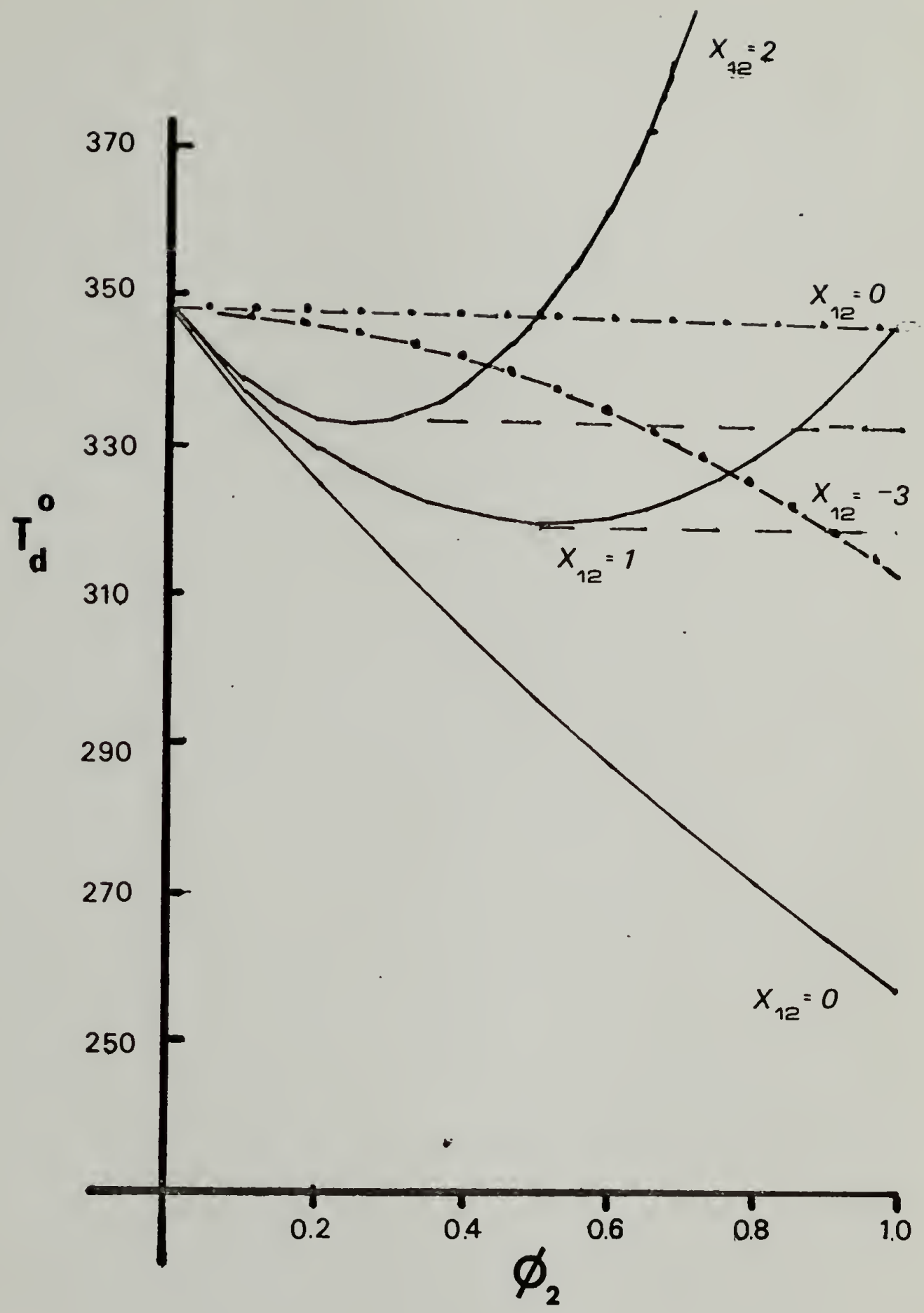
$X_{12} = 2$
$X_{12} = 0$
$X_{12} = -3$
$X_{12} = 1$
$X_{12} = 0$
370
350
330
310
290
270
250
T_d^o
0.2
0.4
0.6
0.8
1.0
ϕ_2

figure 4

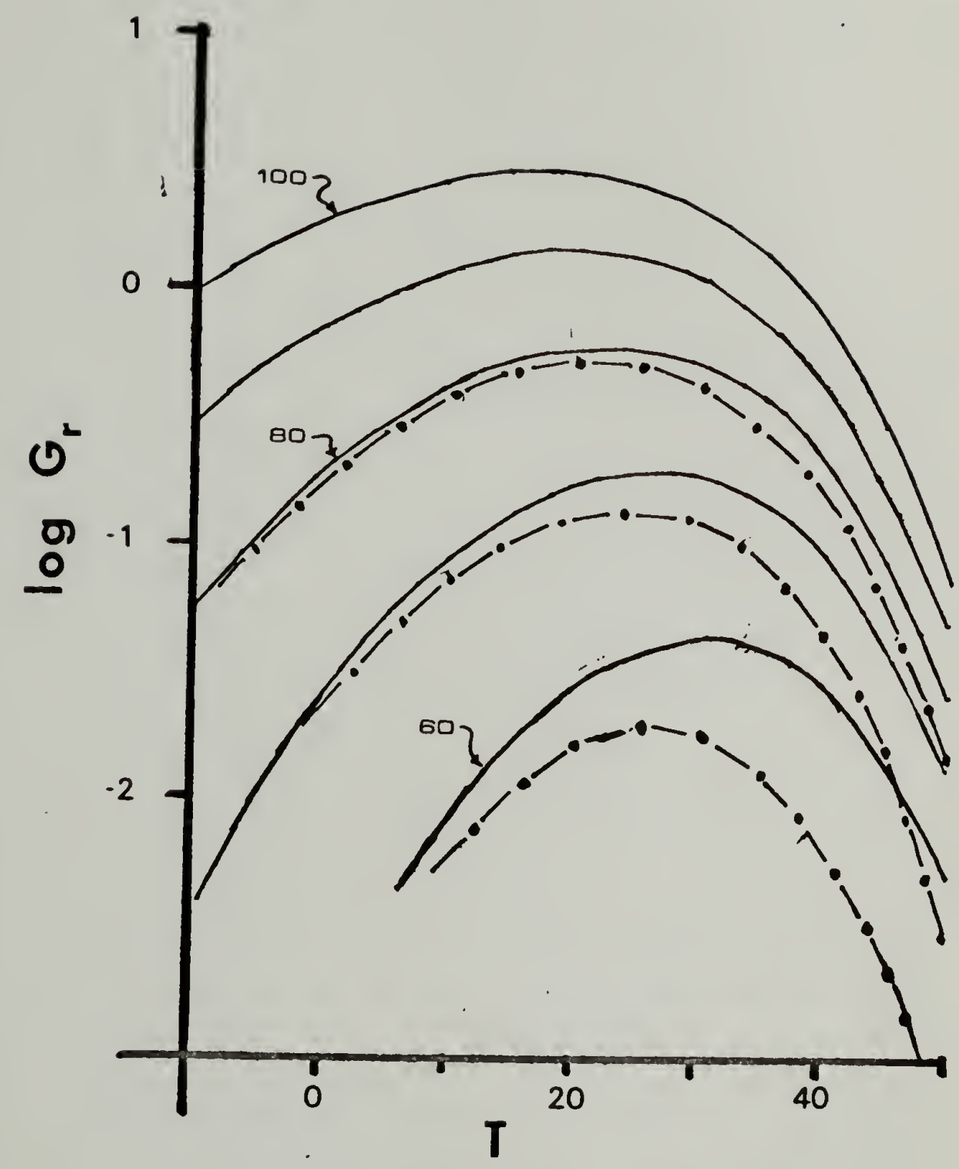

figure 5

figure 6

PEO 7/2
helix

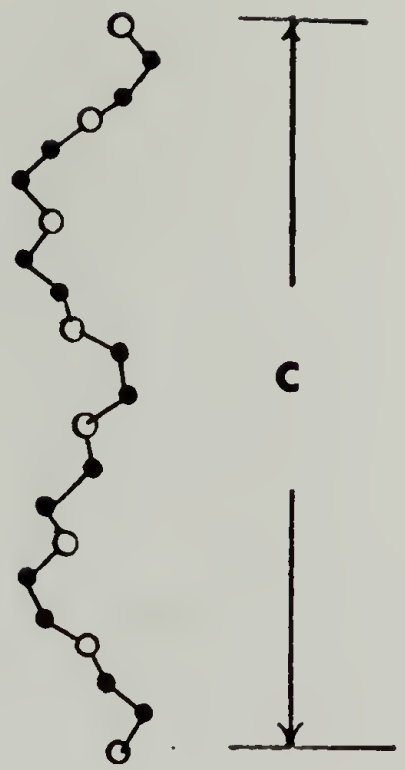

(a)

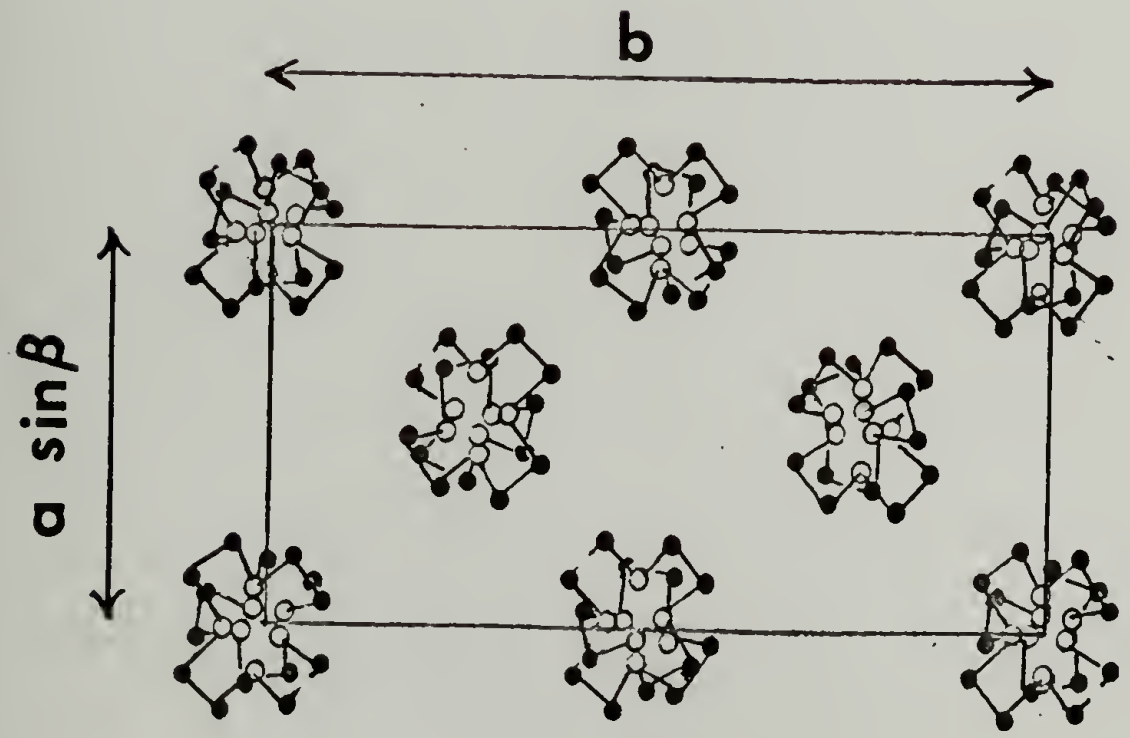

(b)

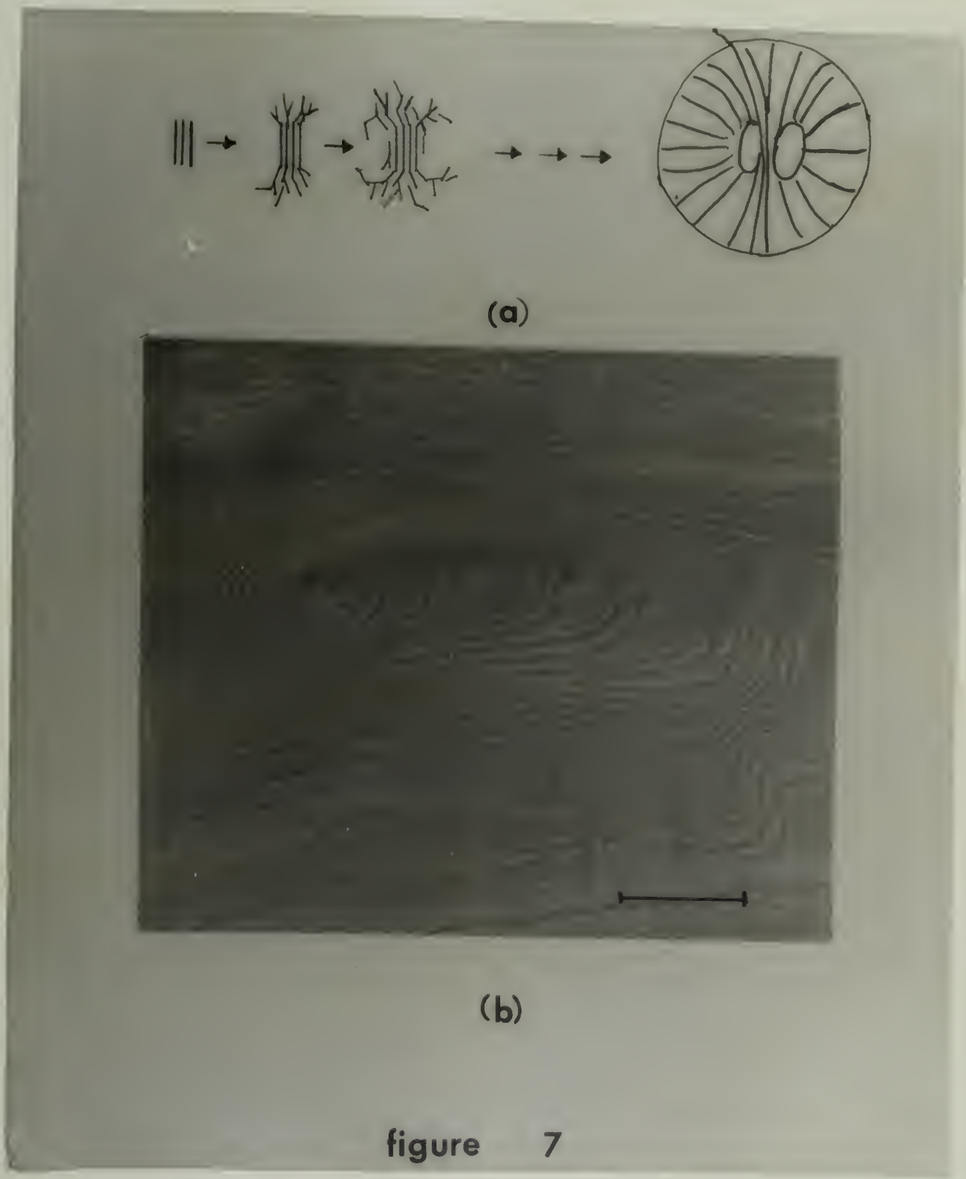

(a)

(b)

figure 7

figure 8

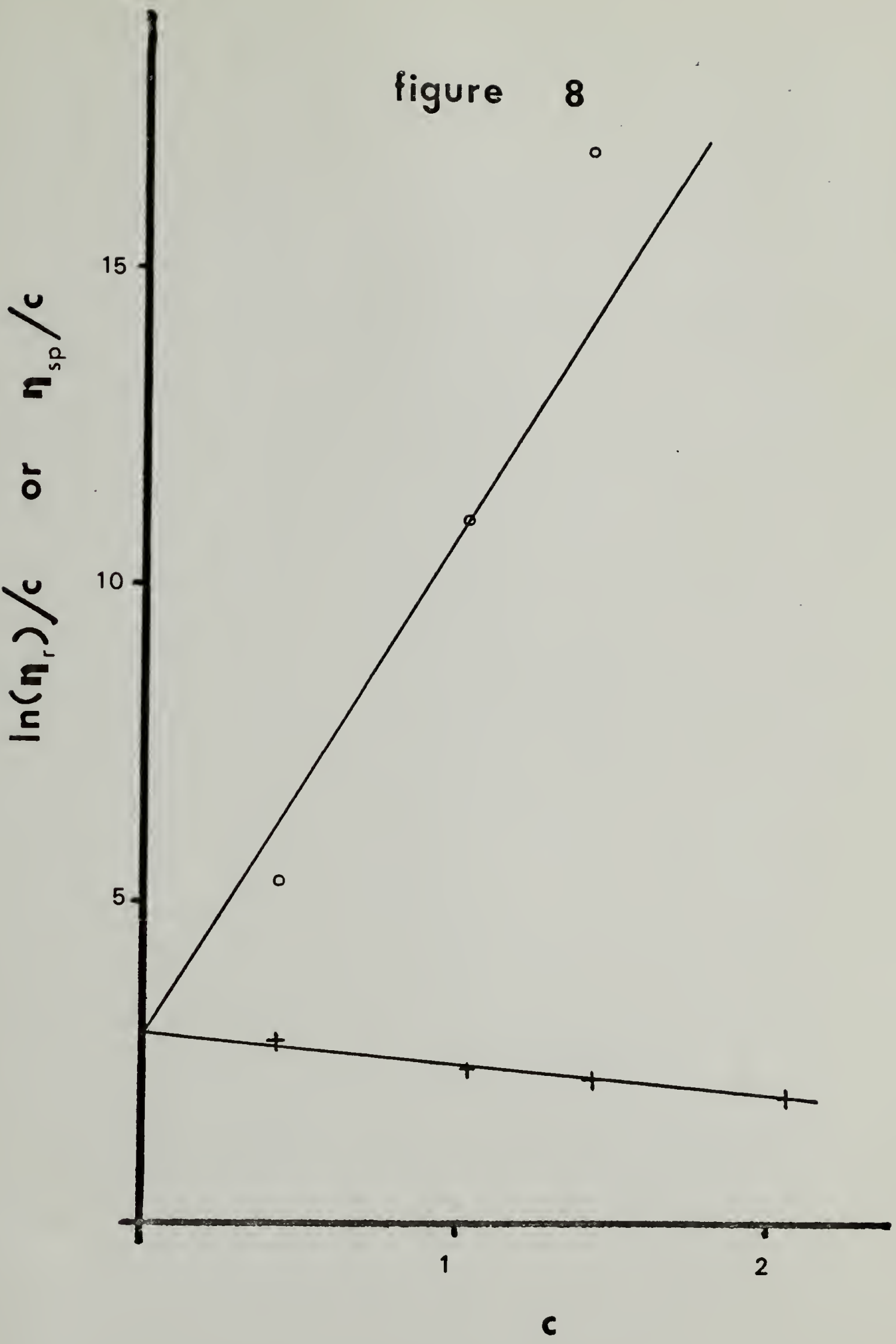

figure 9

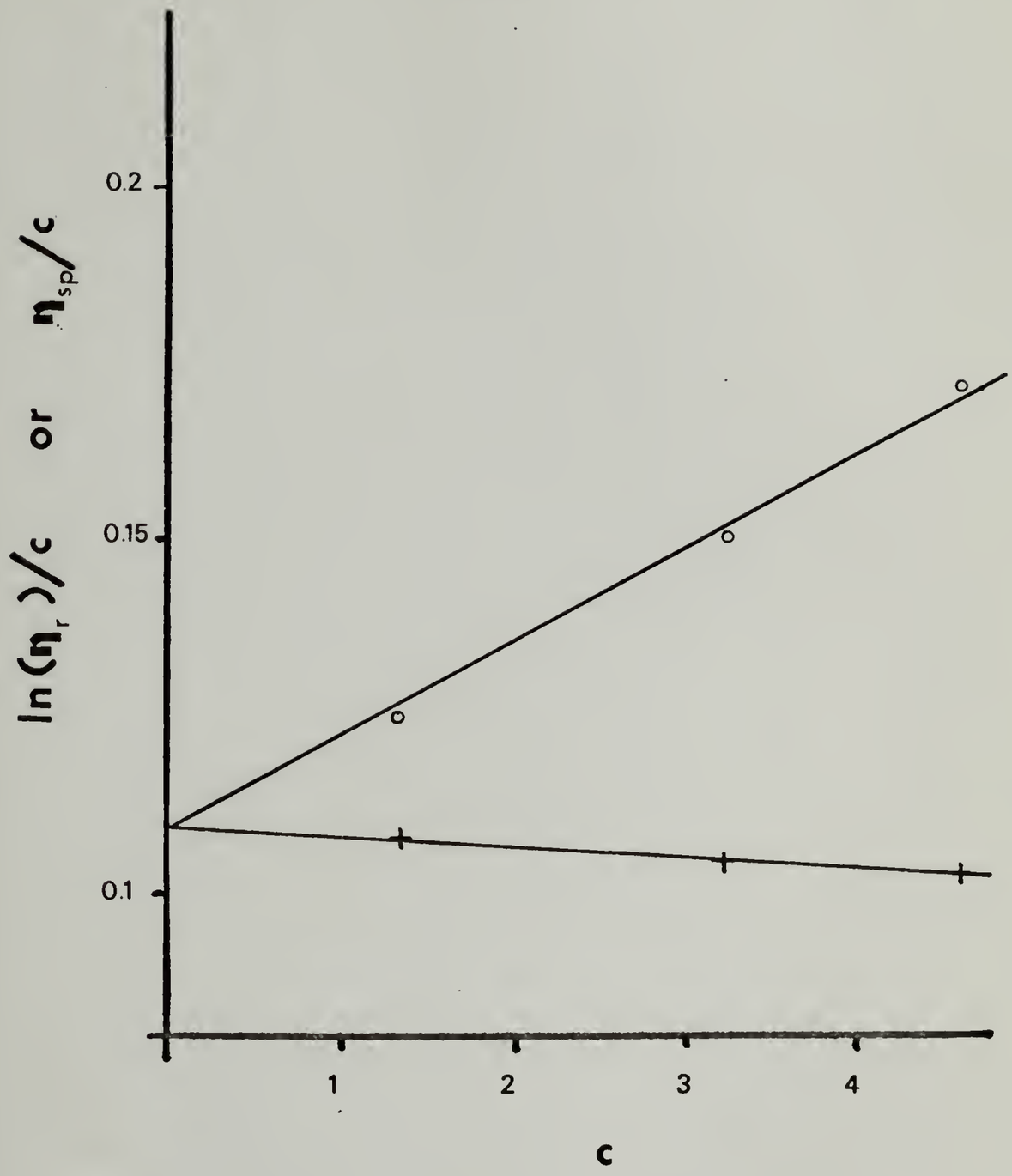

figure 10

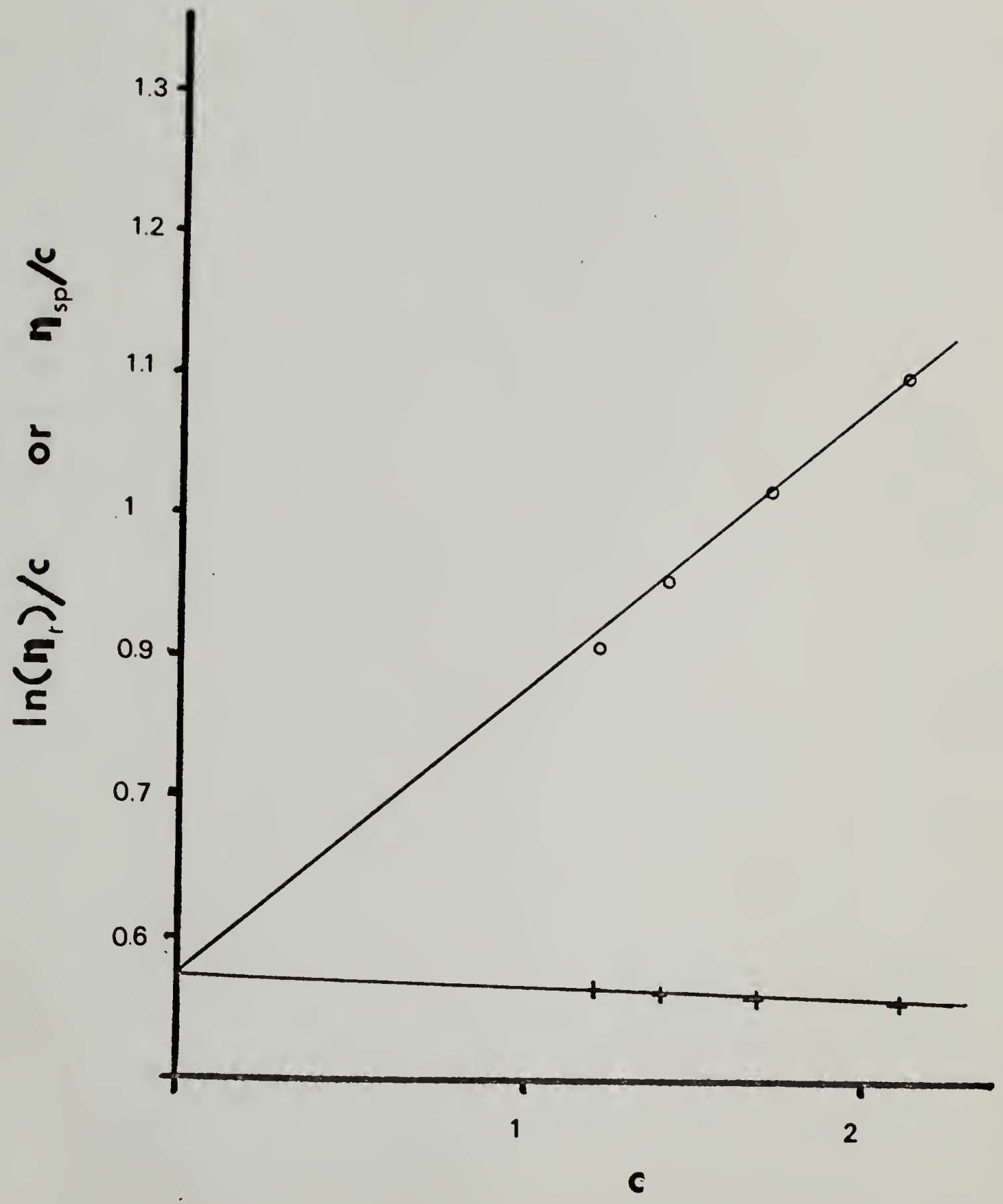

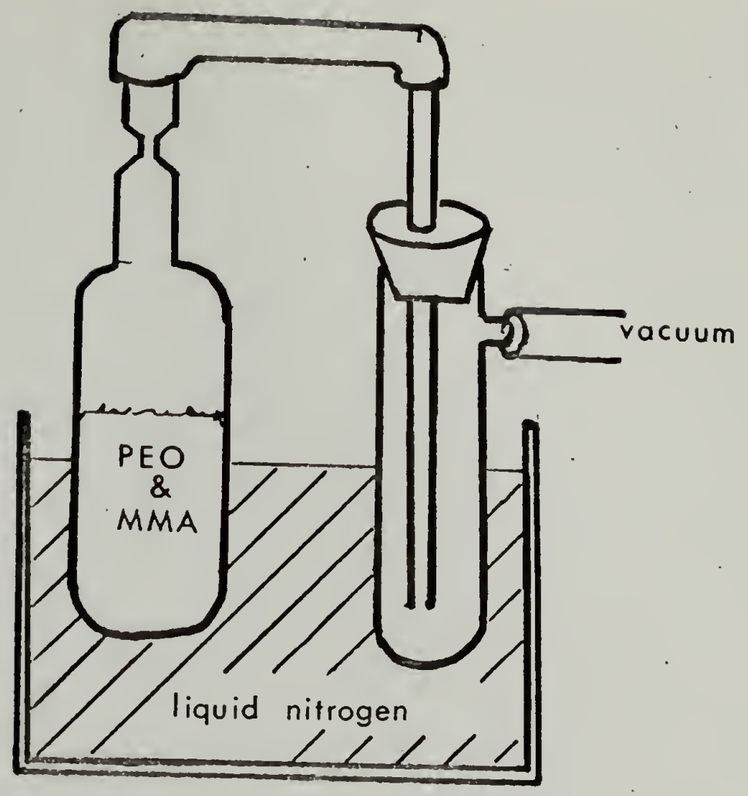

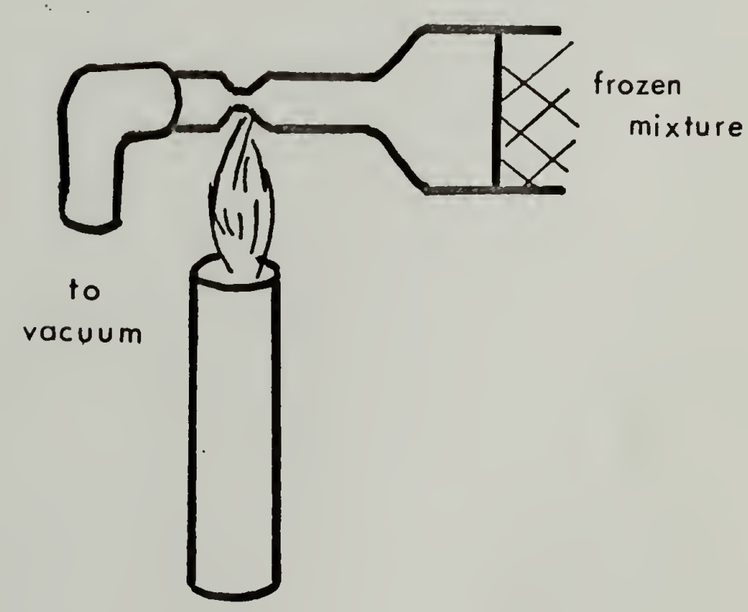

figure 11

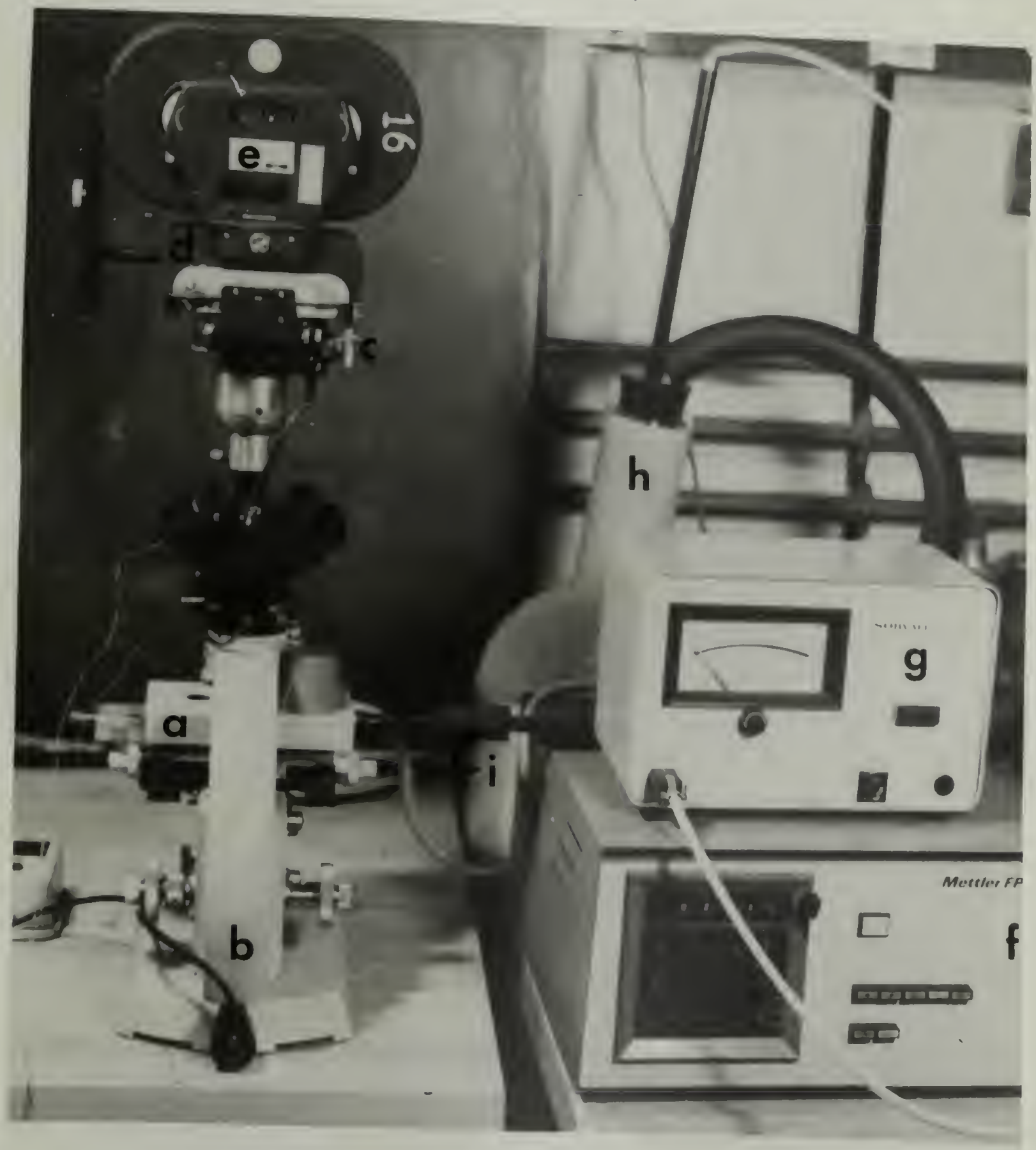

figure 12

figure 13

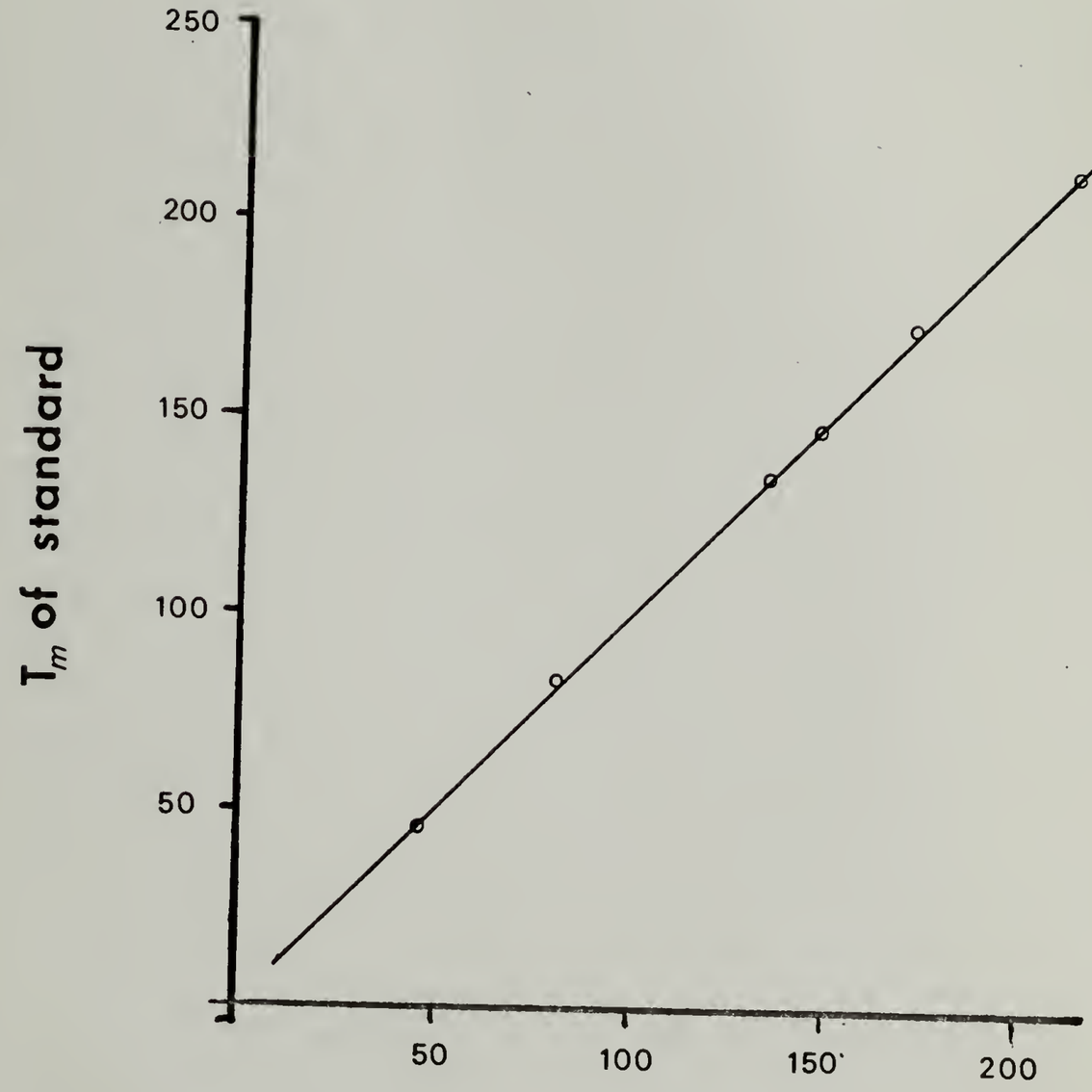

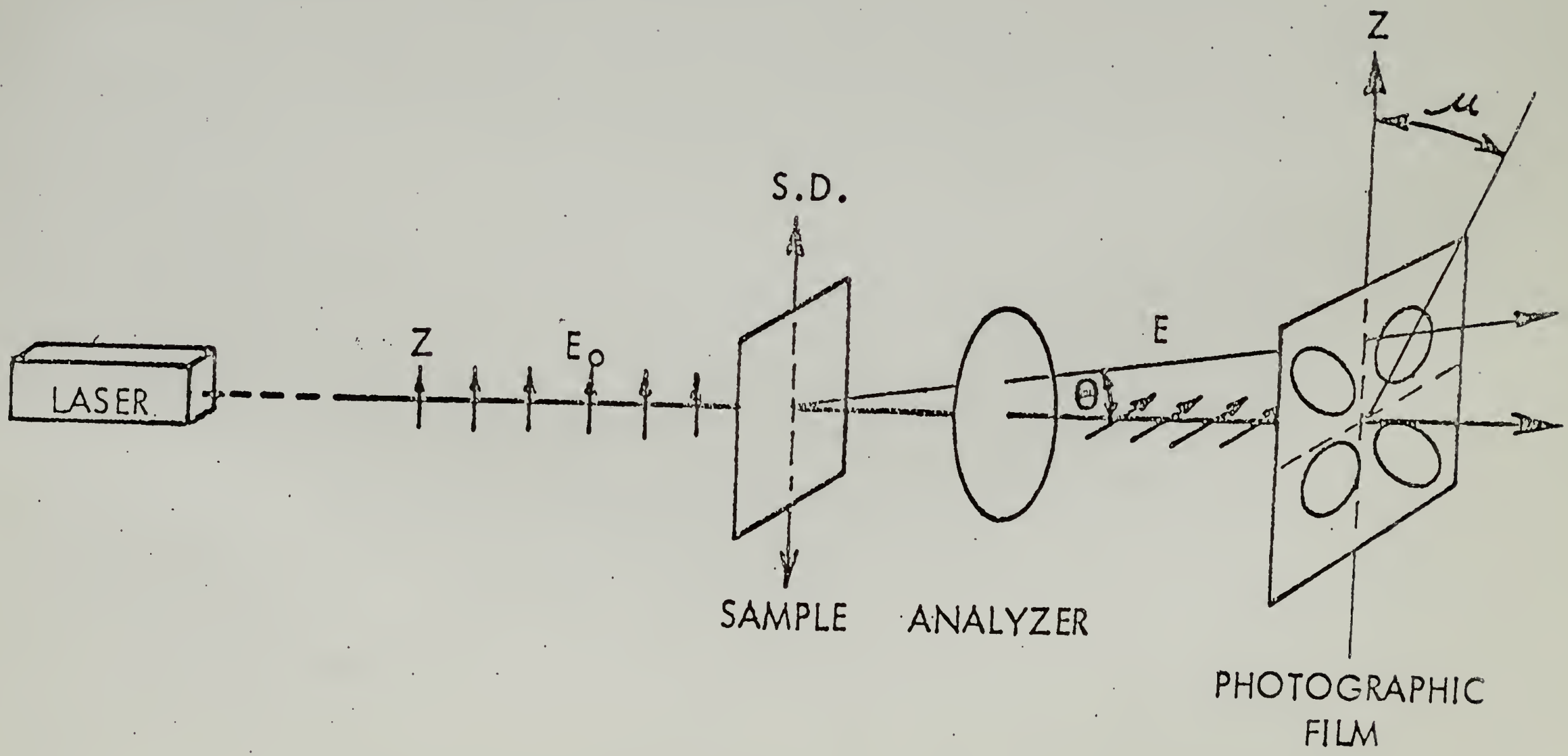

figure 14

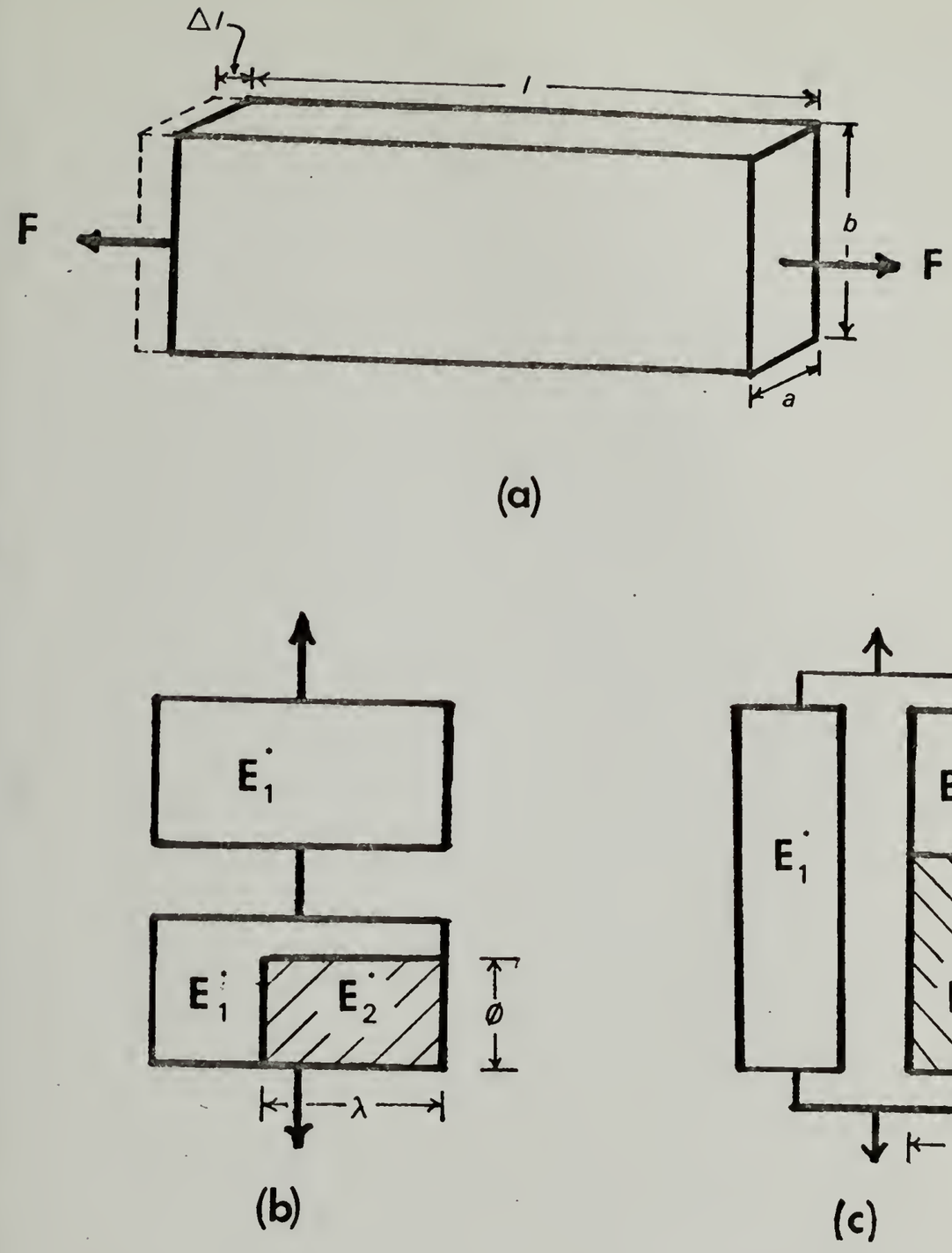

figure 15

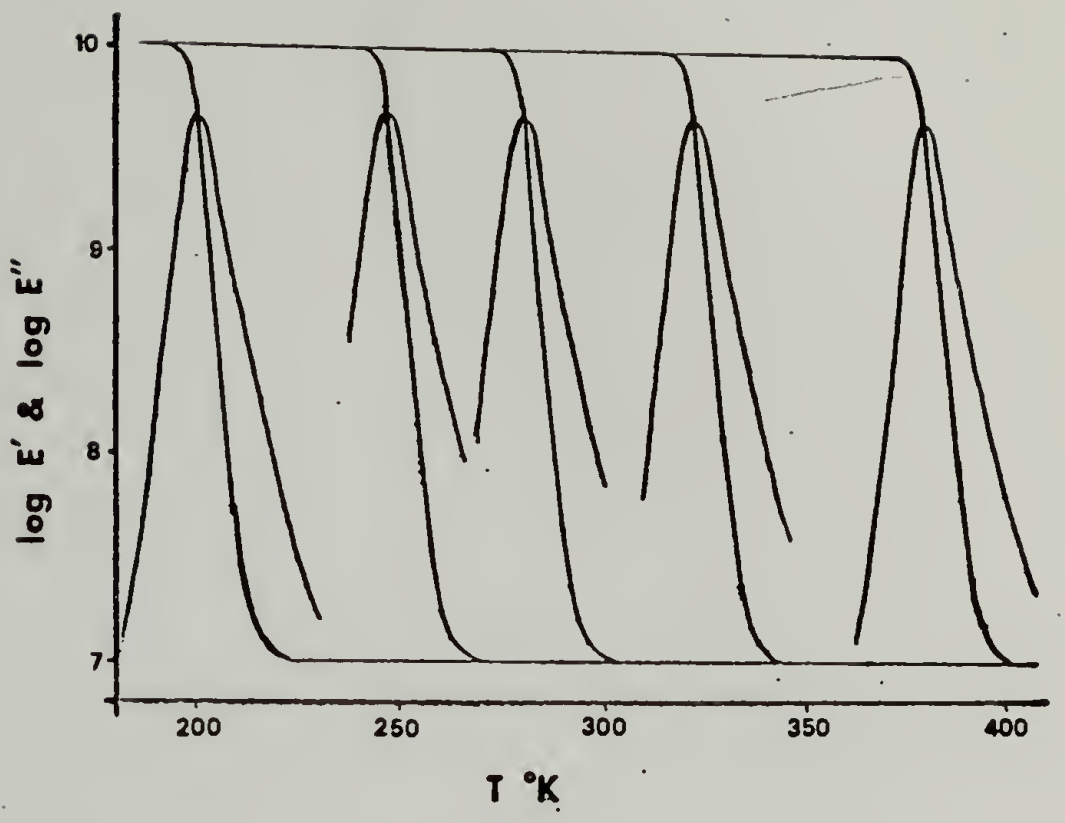
10
9
8
7
log E' & log E''
200
250
300
350
400
T °K

a

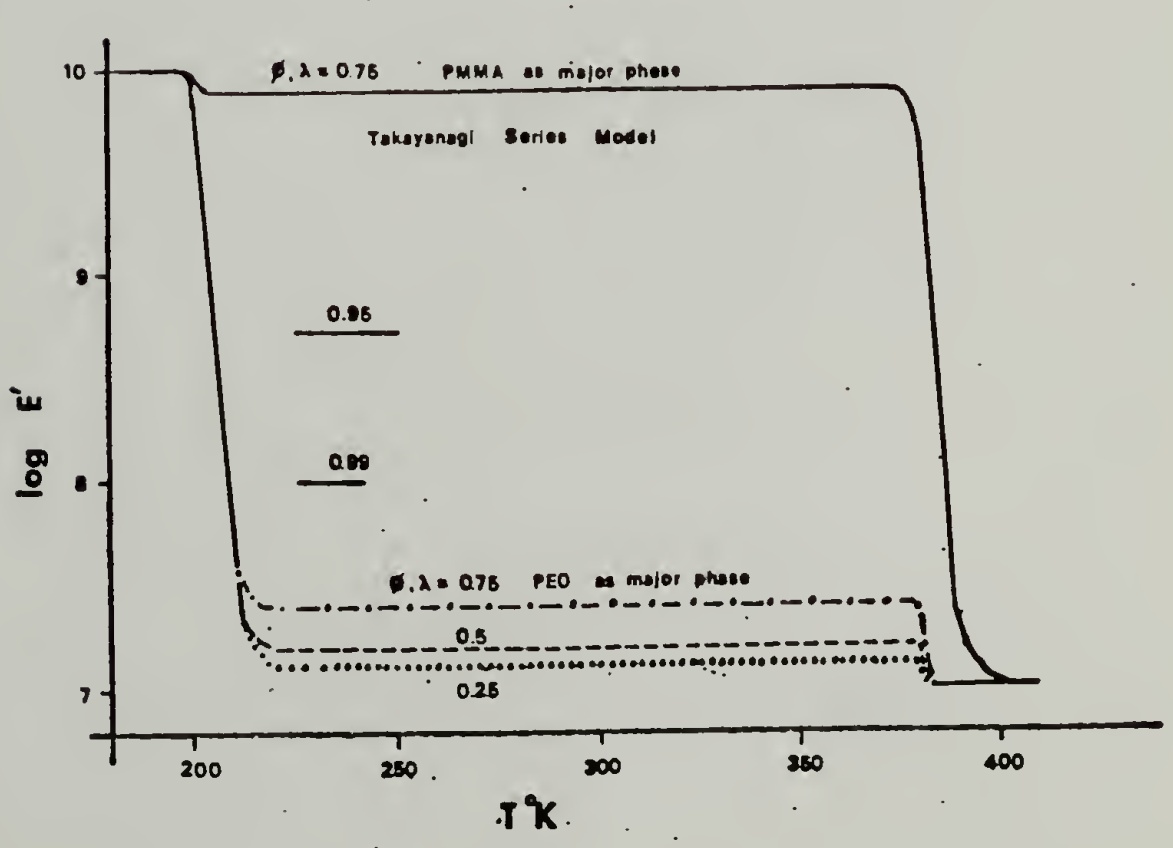
10
9
8
7
log E'
ϕ, λ = 0.75 PMMA as major phase
Takayanagi Series Model
0.95
0.99
ϕ, λ = 0.75 PEO as major phase
0.5
0.25
200
250
300
350
400
T °K

b

figure 16

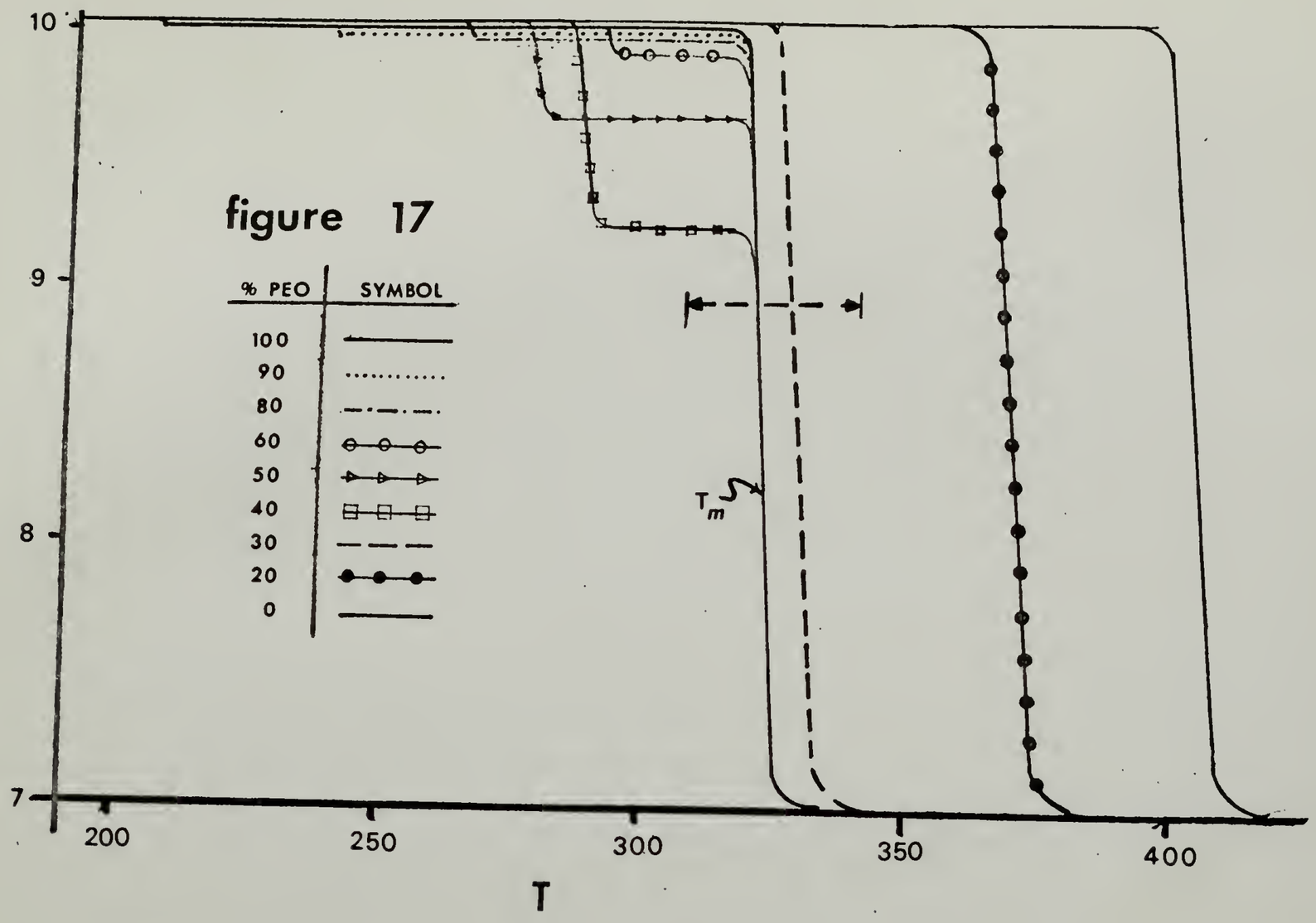
figure 17
% PEO
SYMBOL
100
90
80
60
50
40
30
20
0
log G'
10
9
8
7
200
250
300
350
400
T
T_m

PEO/ PMMA 18/82: C6K/MMA

figure 18

a

b

PEO/PMMA 33/67: C6K/MMA

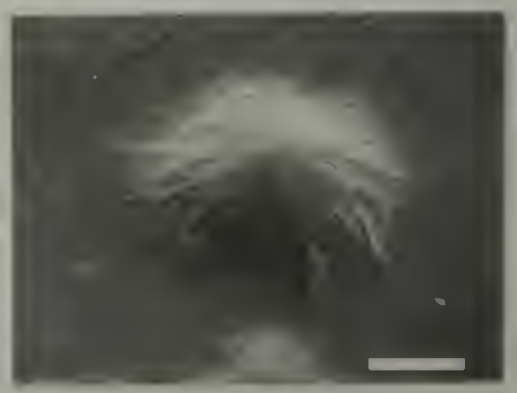

c

d

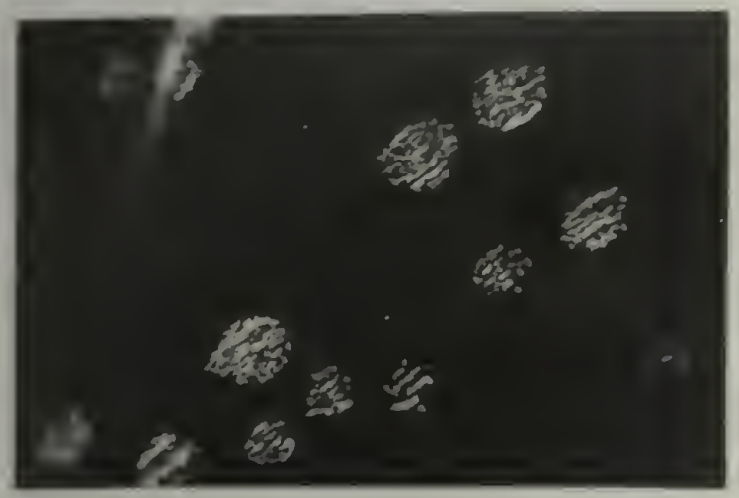

e

PEO/PMMA 50/50-WSR HM
figure 19
a
b
c
d
e
f
g
h
i
j
k

PEO WSR-N-3000

figure 20

a

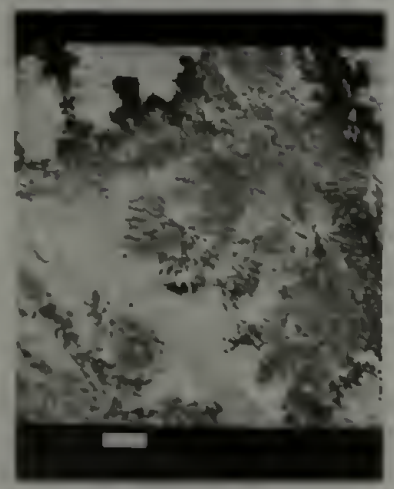

b

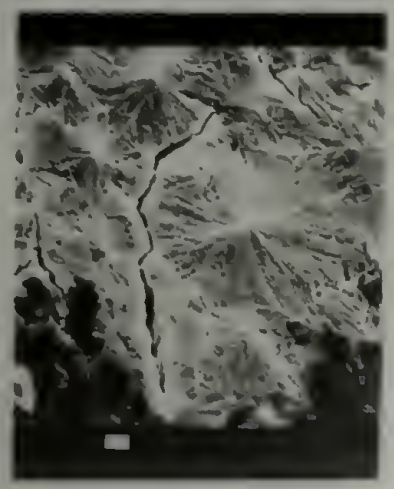

c

d

e

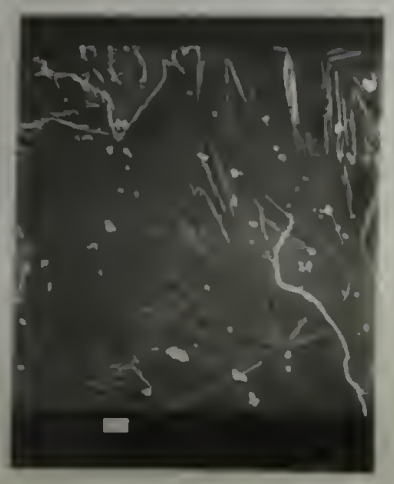

f

PEO/PMMA 90/10:WSR, HM

figure 21

PEO/ PMMA 80/20:WSR/ HM

figure 22

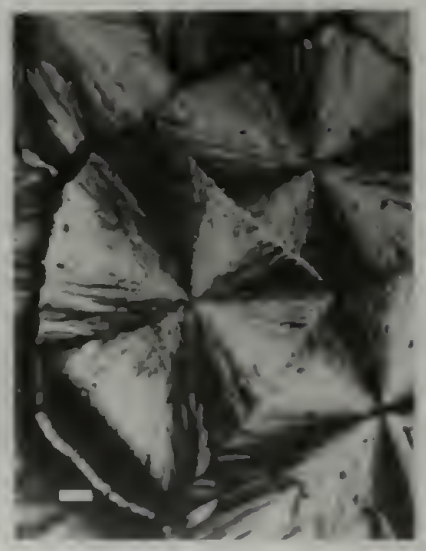

a

b

c

d

e

f

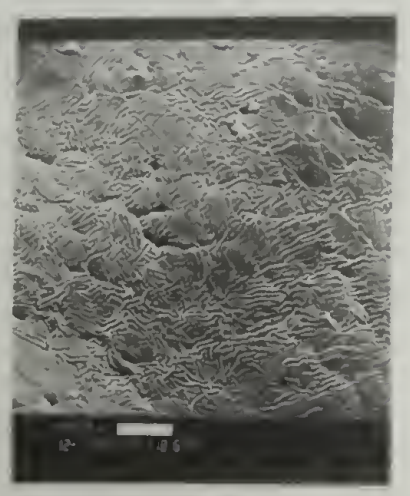

g

PEO / PMMA 70/30:WSR / HM

figure 23

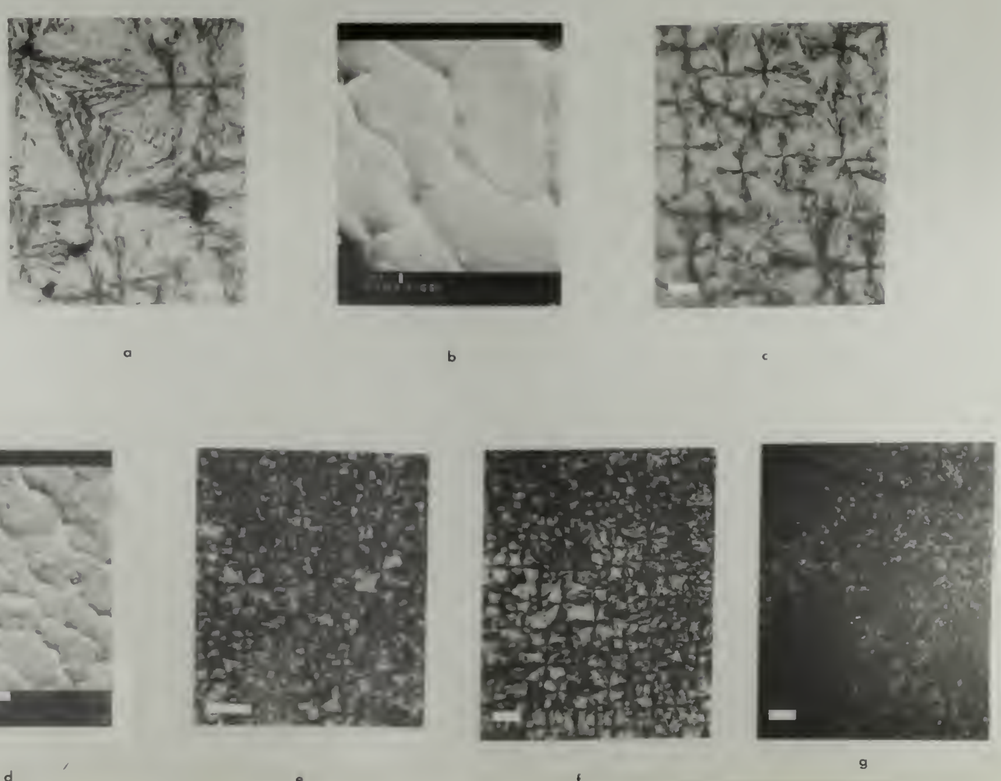

a b c

d e f g

PEO/ PMMA 60/40:WSR/HM

figure 24

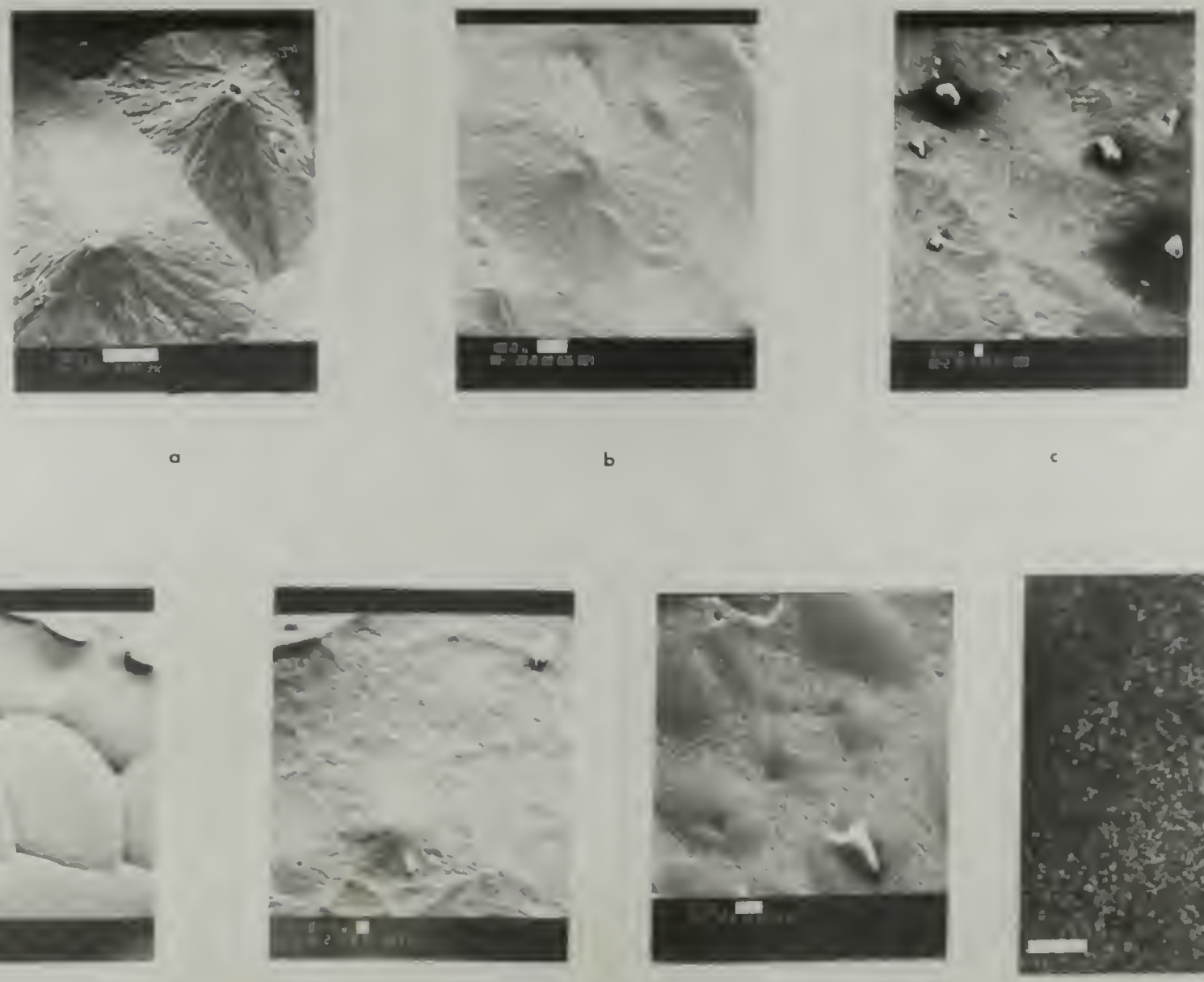

a b c

d e f g

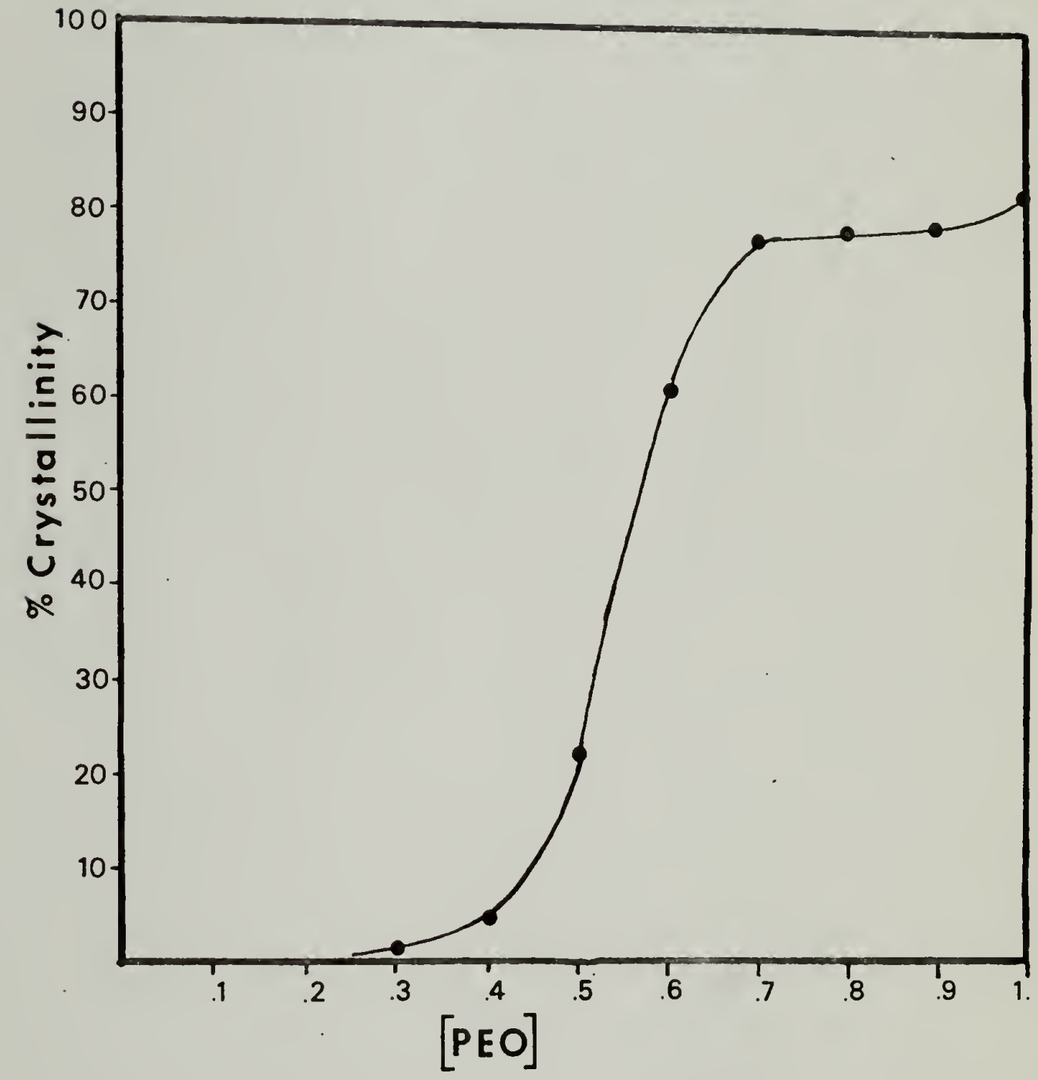

figure 25

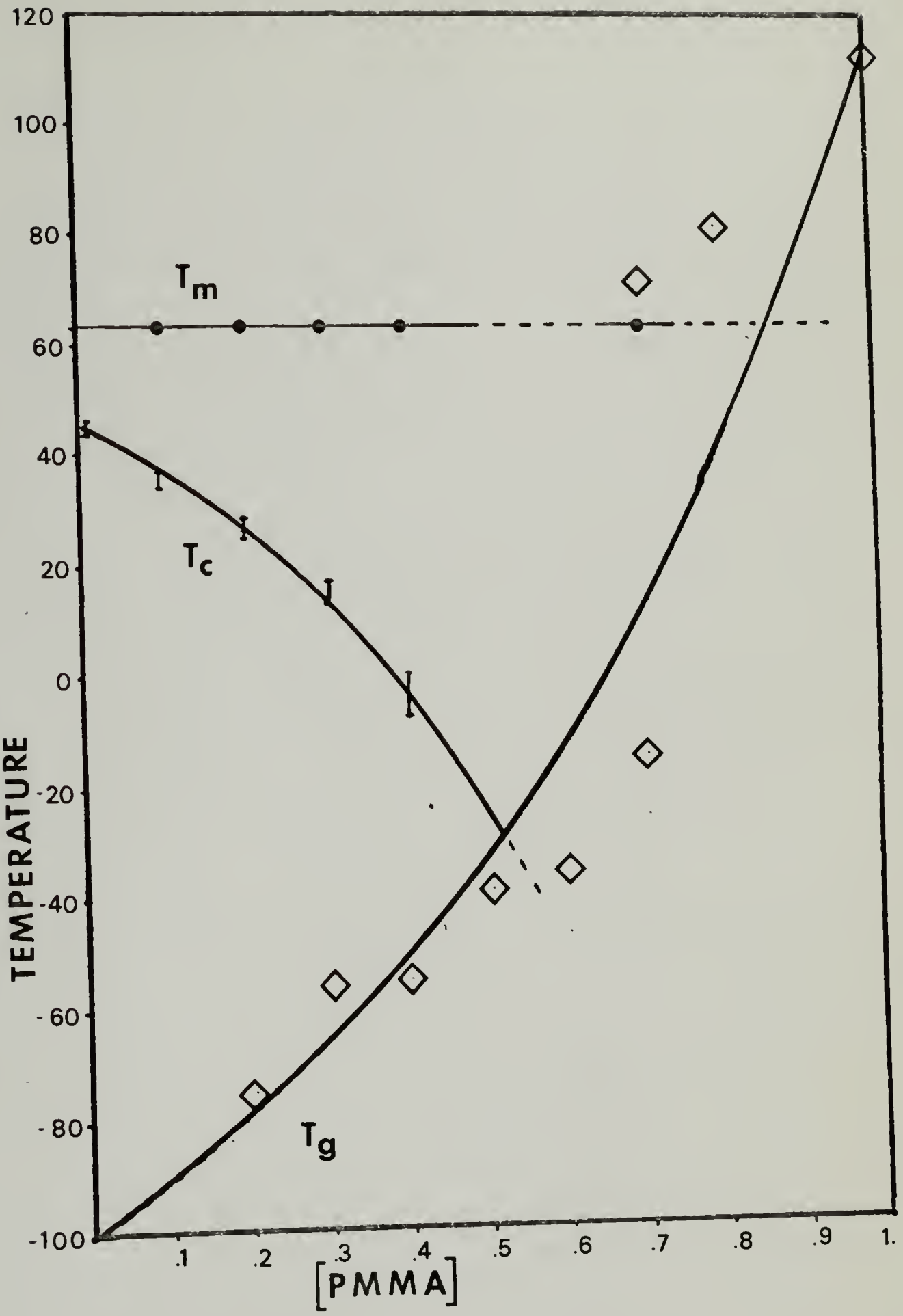
120
100
80
60
40
20
0
-20
-40
-60
-80
-100
TEMPERATURE
T_m
T_c
T_g
.1
.2
.3
.4
.5
.6
.7
.8
.9
1.
[PMMA]

figure 26

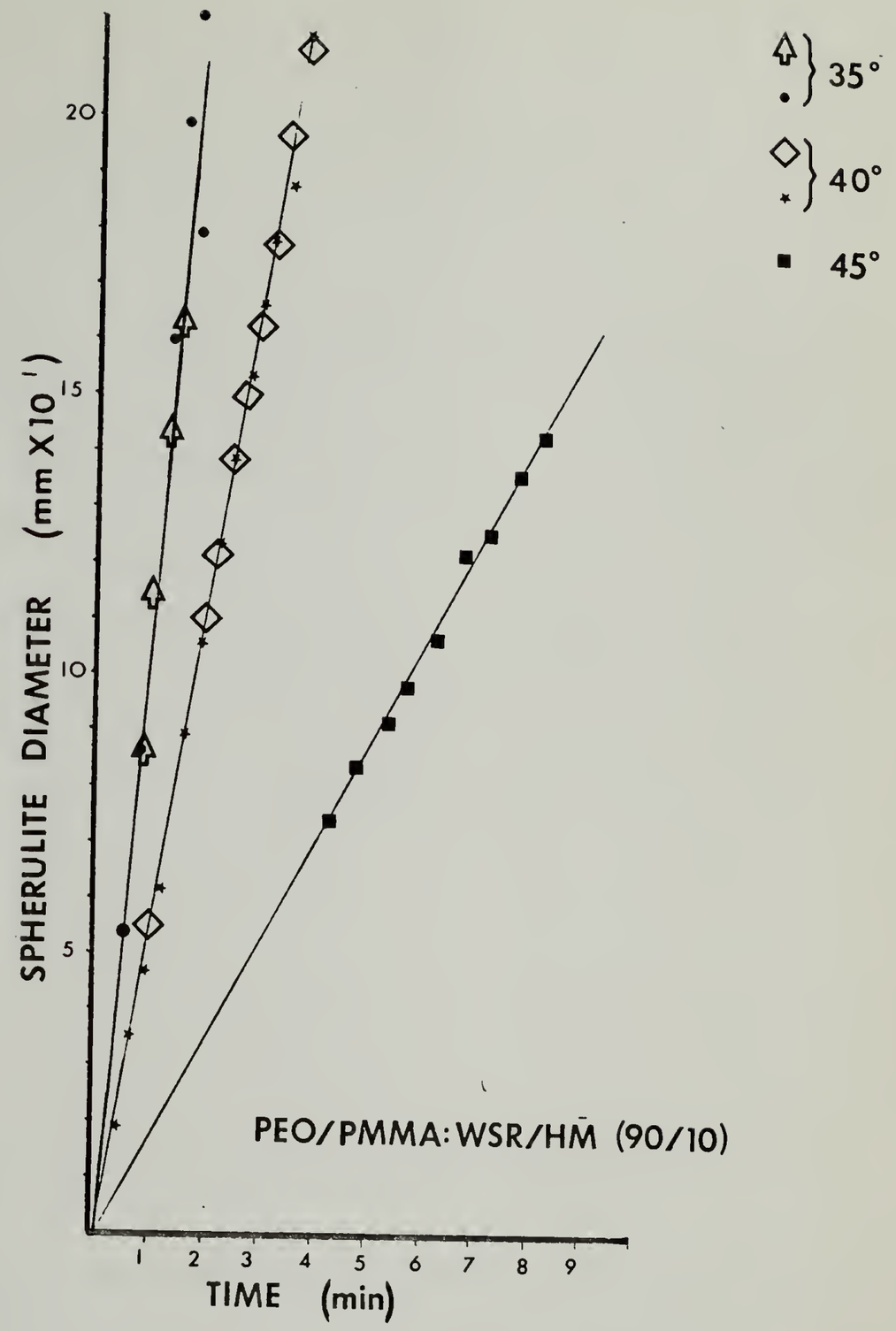
35°
40°
45°
SPHERULITE DIAMETER (mm X10⁻¹)
5
10
15
20
1
2
3
4
5
6
7
8
9
TIME (min)
PEO/PMMA: WSR/HM (90/10)

figure 27

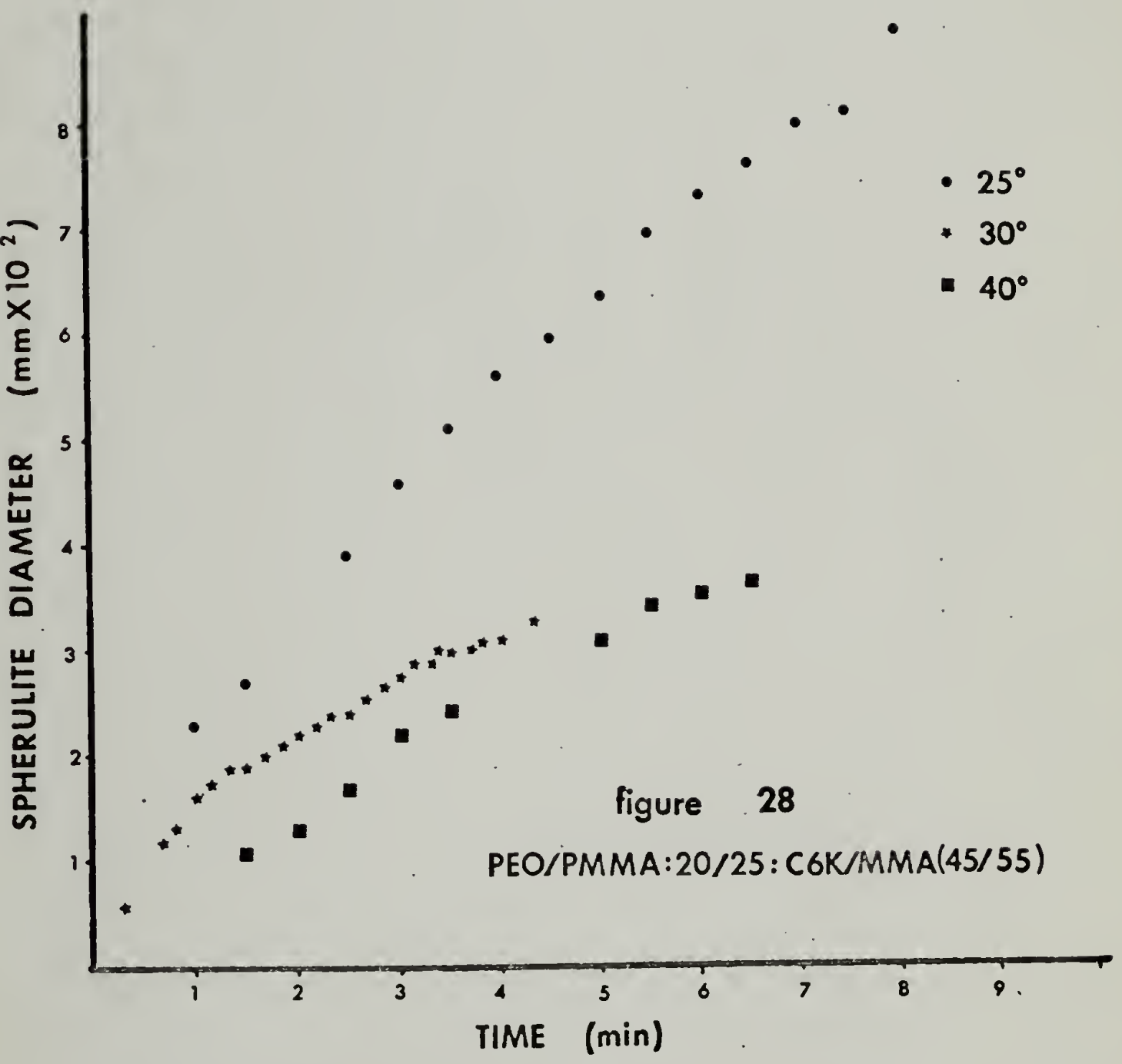

figure 28

PEO/PMMA:20/25:C6K/MMA(45/55)

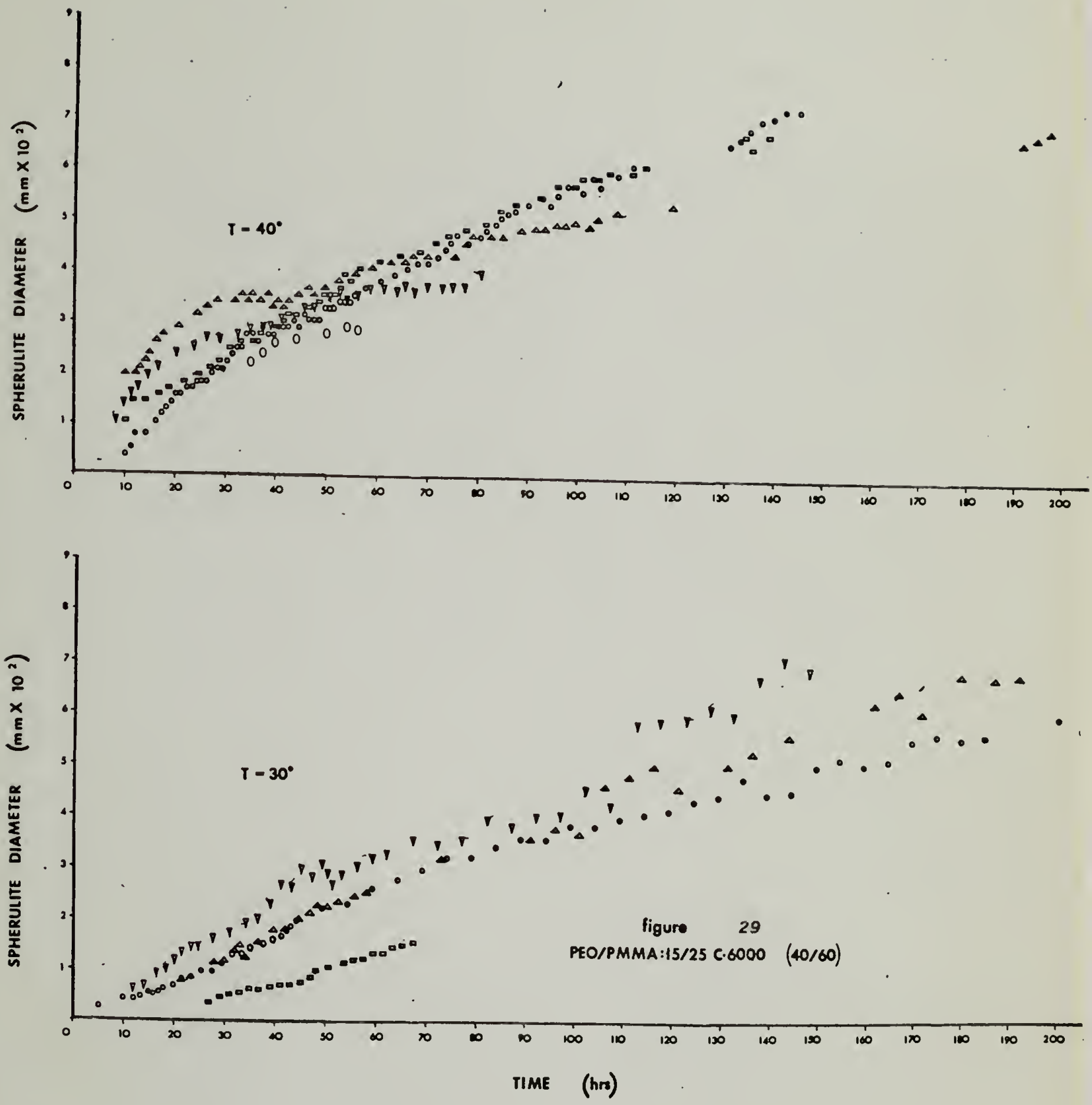

figure 29

PEO/PMMA:15/25 C·6000 (40/60)

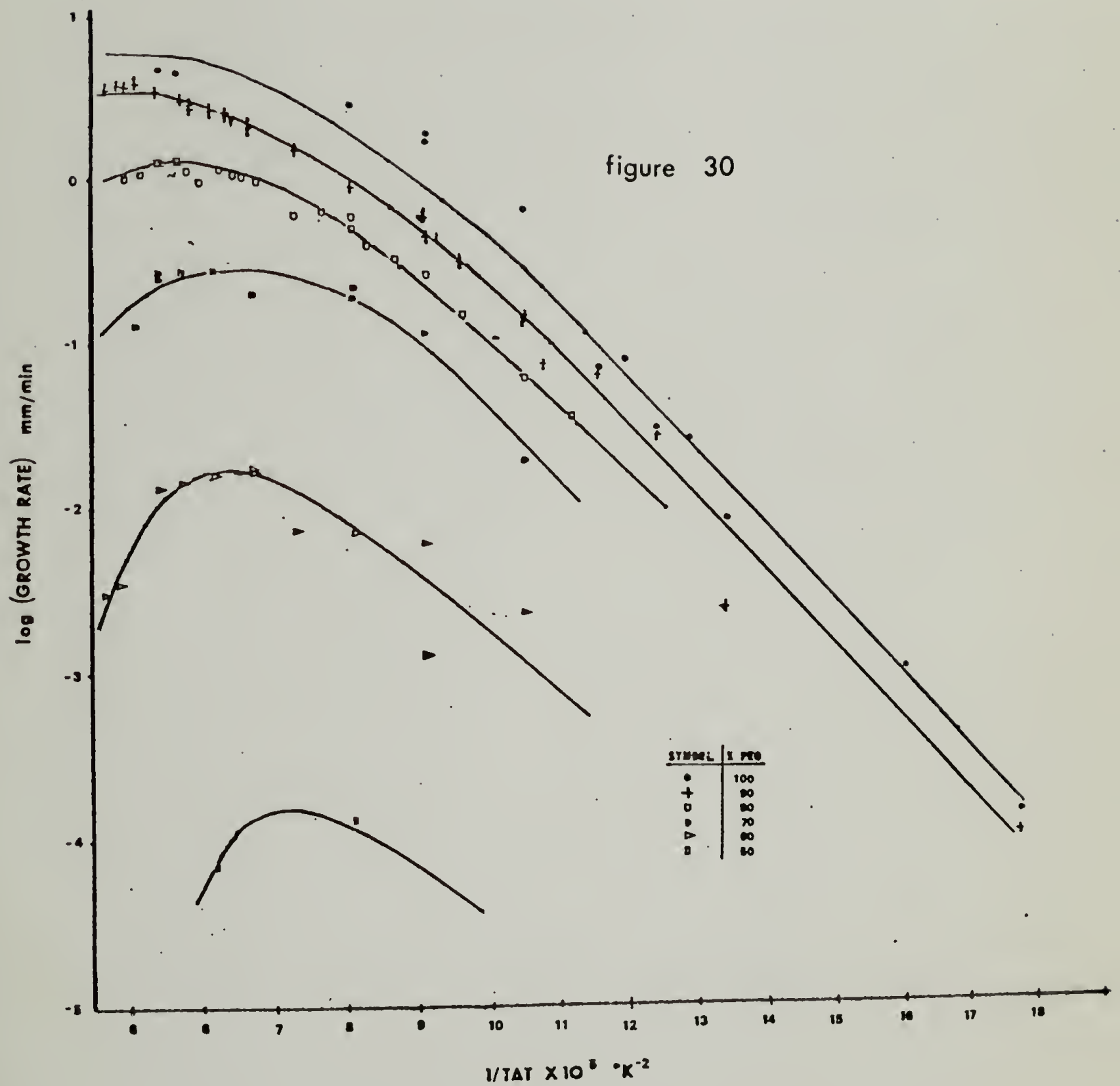
log (GROWTH RATE) mm/min
1
0
-1
-2
-3
-4
-5
6
7
8
9
10
11
12
13
14
15
16
17
18
1/TΔT X 10⁵ °K⁻²
SYMBOL
% PEG
100
80
60
40
30
20

figure 30

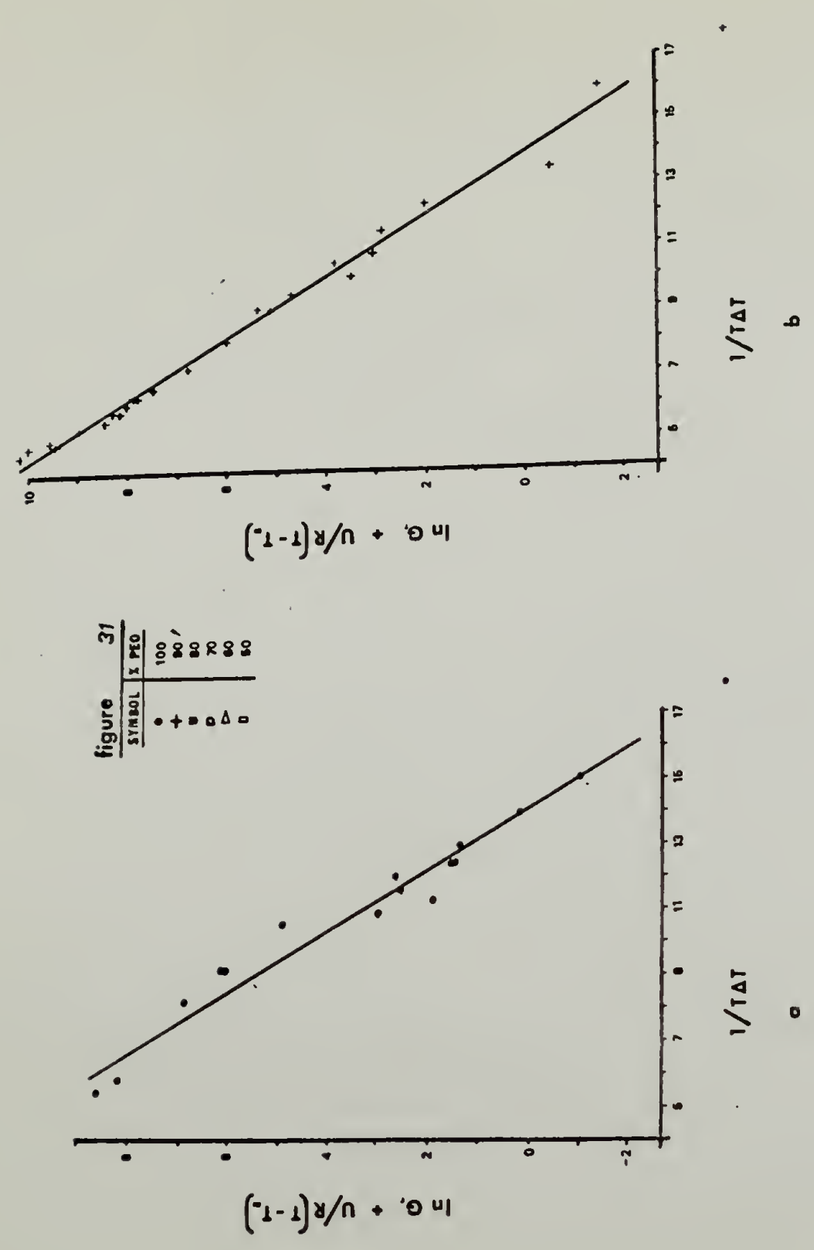

figure 31

SYMBOL	% PEO
●	100
+	80
■	80
▽	80
□	80
△	80

figure 32

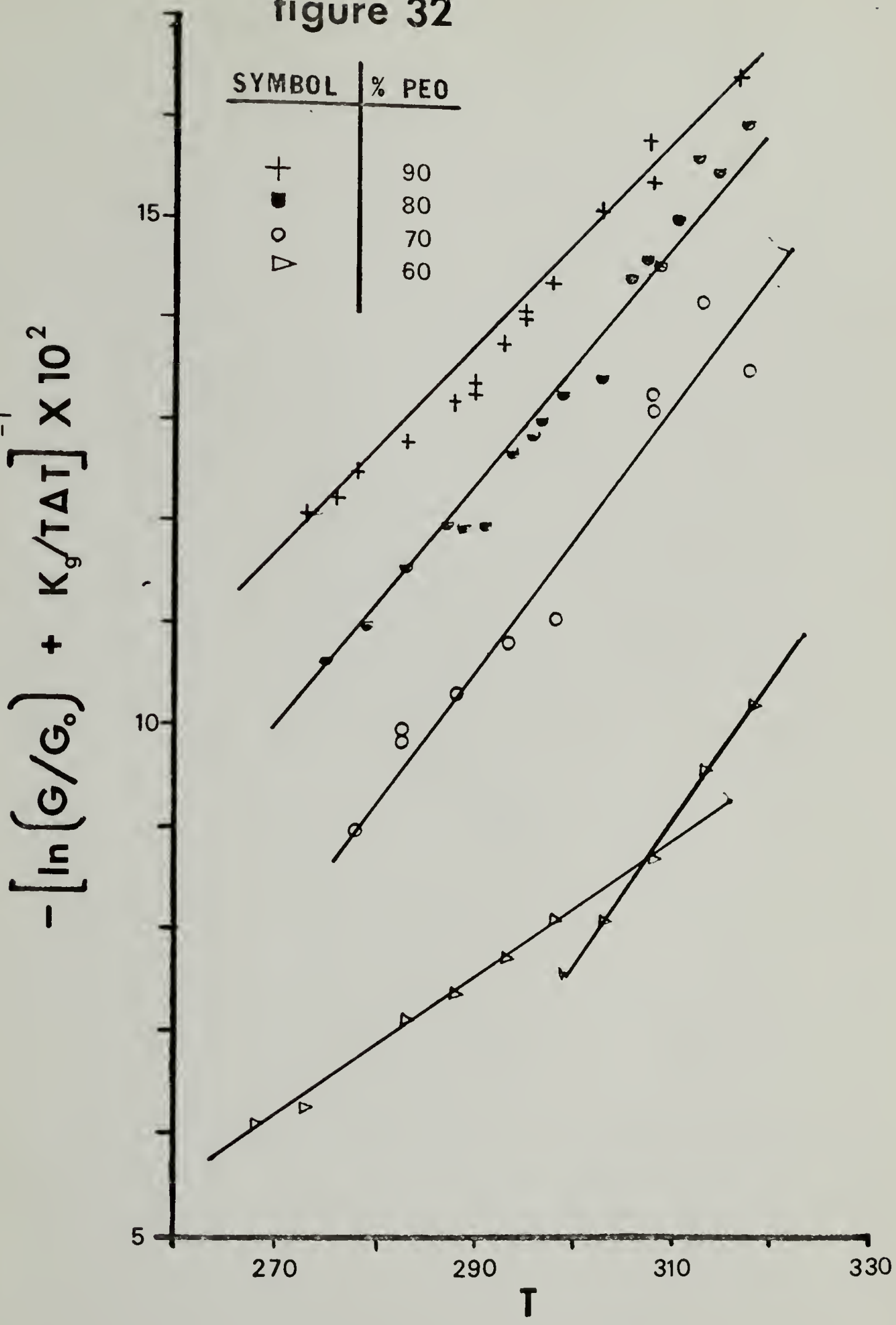
SYMBOL
% PEO
90
80
70
60
15
10
5
270
290
310
330
T
$-\left[\ln\left(G/G_o\right) + K_g/T\Delta T\right]^{-1} \times 10^2$

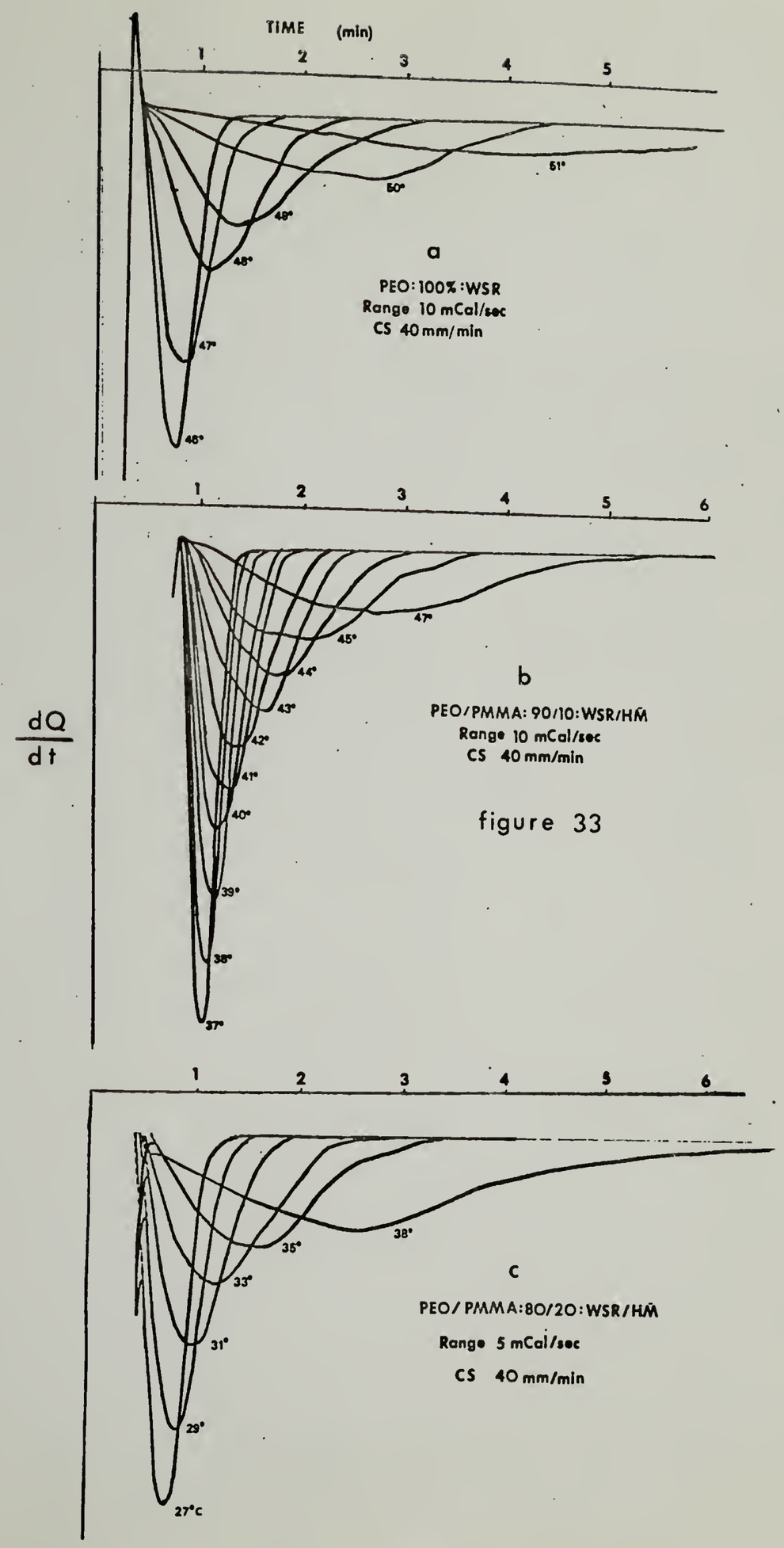
TIME (min)
1
2
3
4
5
6
51°
50°
49°
48°
47°
46°
a
PEO: 100% :WSR
Range 10 mCal/sec
CS 40 mm/min
45°
44°
43°
42°
41°
40°
39°
38°
37°
b
PEO/PMMA: 90/10: WSR/HM
Range 10 mCal/sec
CS 40 mm/min
dQ/dt
38°
35°
33°
31°
29°
27°c
C
PEO/ PMMA:80/20: WSR/HM
Range 5 mCal/sec
CS 40 mm/min

figure 33

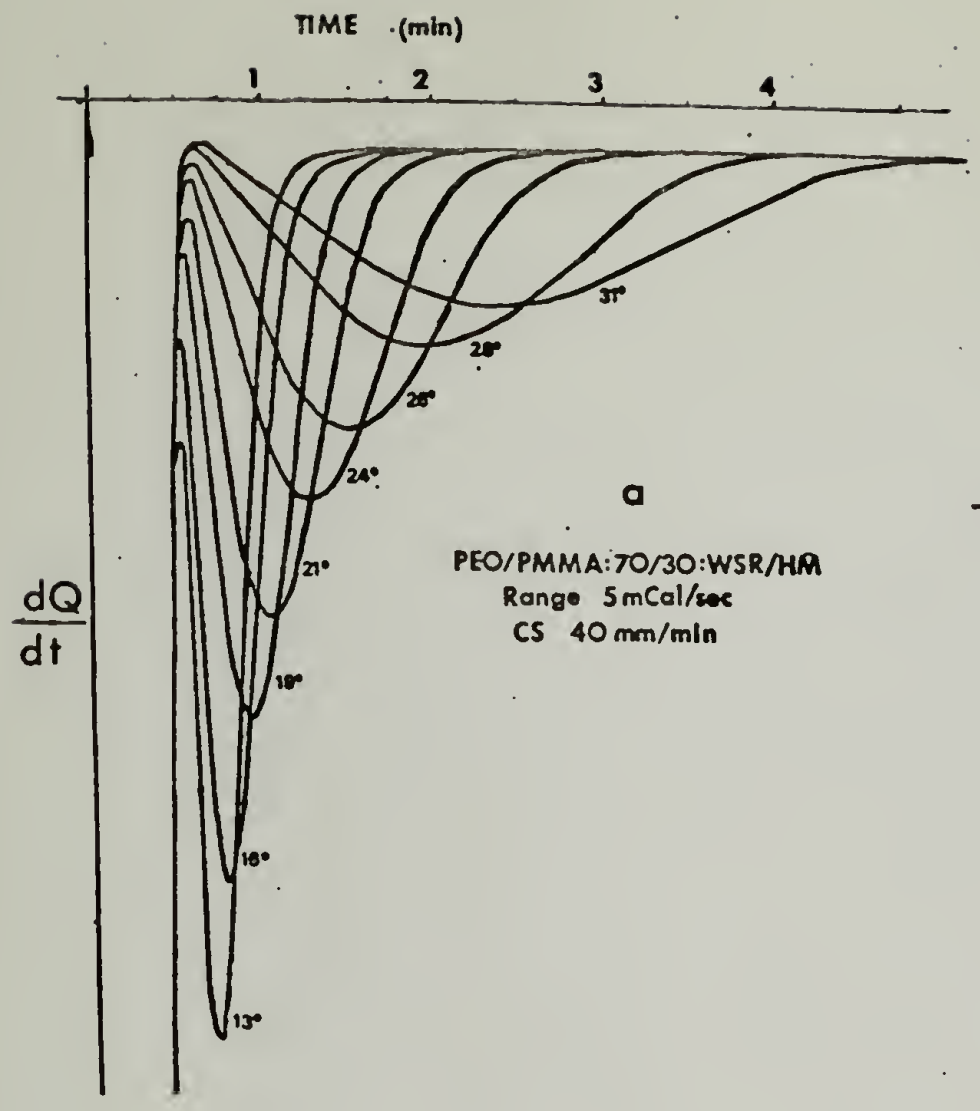
TIME (min)
1
2
3
4
dQ/dt
37°
28°
26°
24°
21°
19°
18°
13°
a
PEO/PMMA:70/30:WSR/HM
Range 5 mCal/sec
CS 40 mm/min

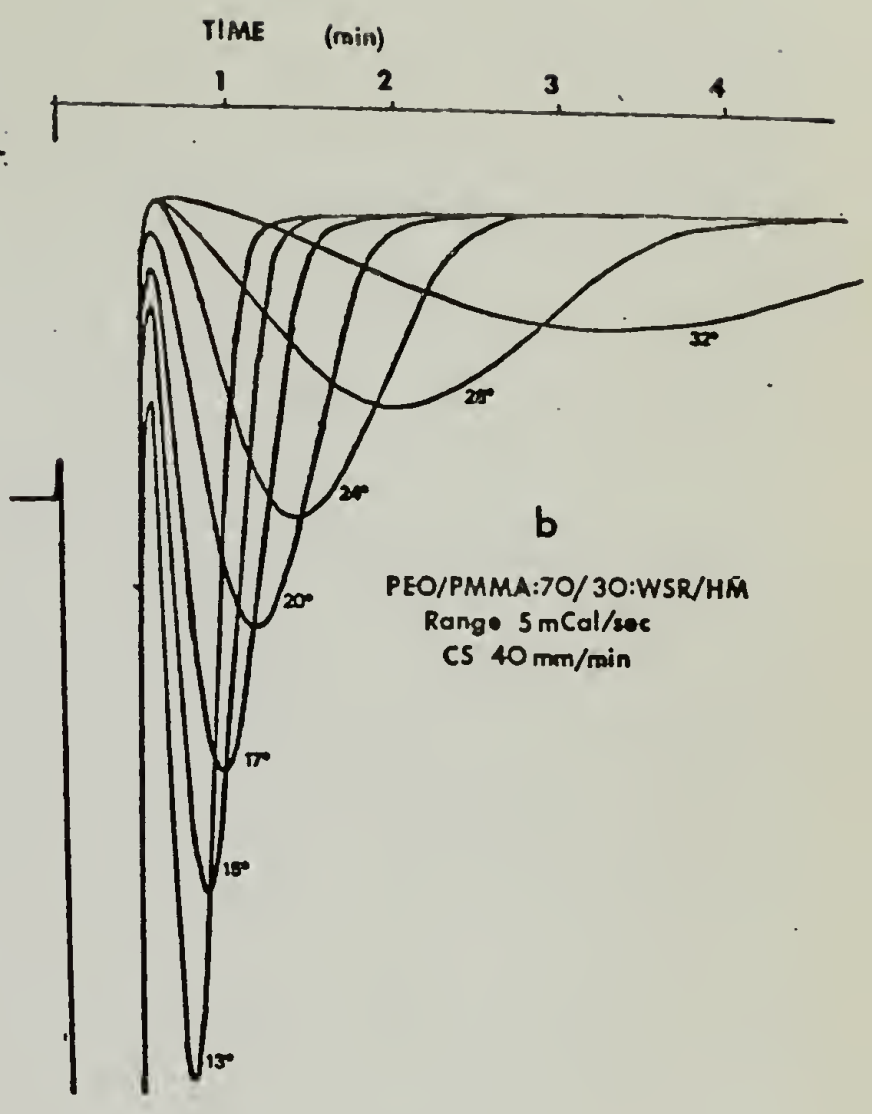
TIME (min)
1
2
3
4
32°
28°
24°
20°
17°
15°
13°
b
PEO/PMMA:70/30:WSR/HM
Range 5 mCal/sec
CS 40 mm/min

figure 34

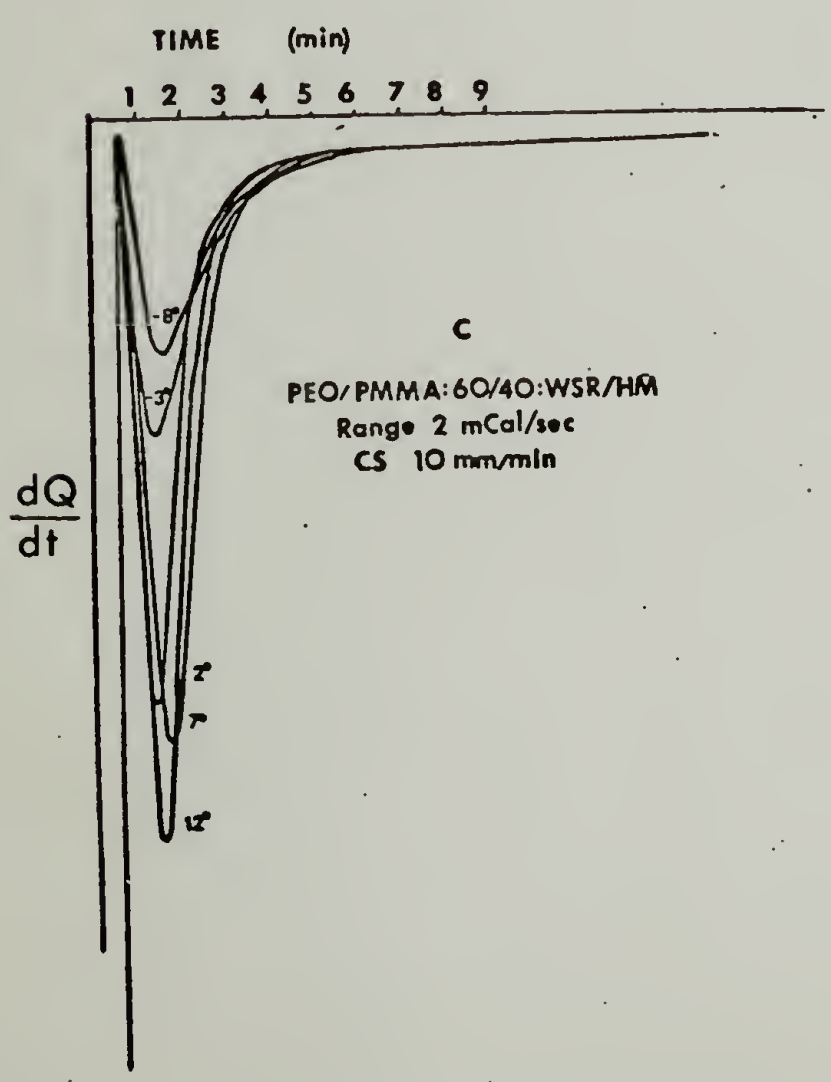
TIME (min)
1 2 3 4 5 6 7 8 9
dQ/dt
8°
3°
2°
7°
12°
c
PEO/PMMA:60/40:WSR/HM
Range 2 mCal/sec
CS 10 mm/min

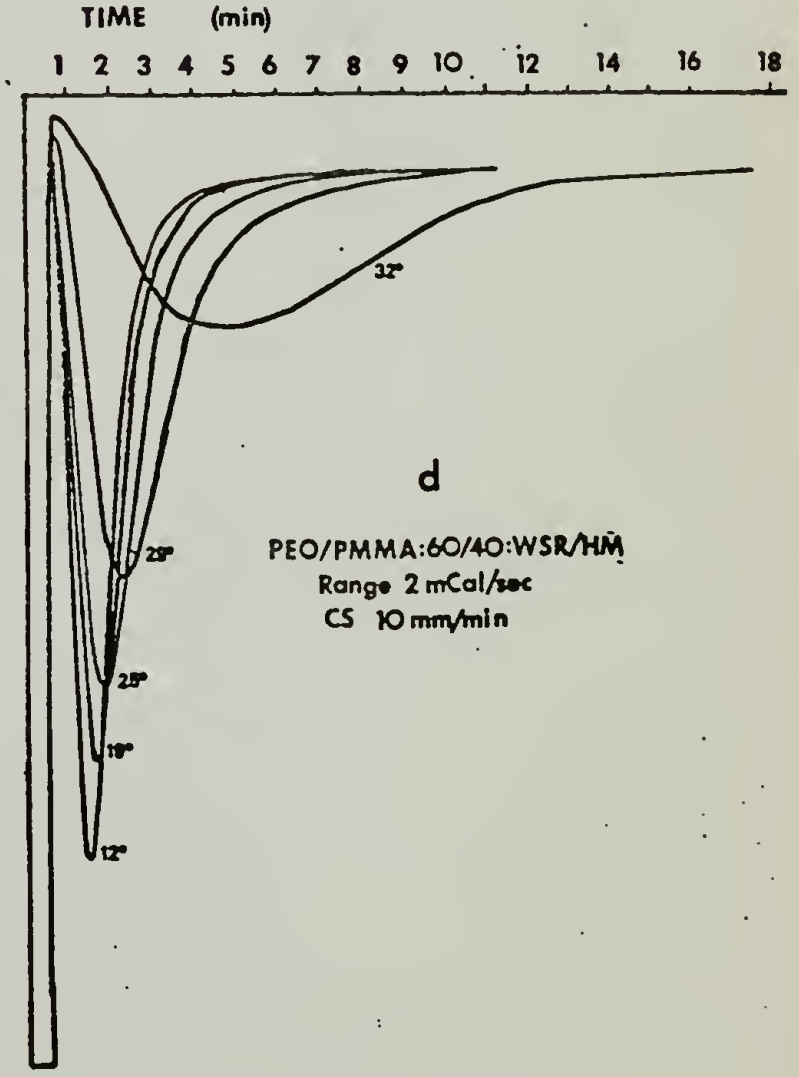
TIME (min)
1 2 3 4 5 6 7 8 9 10 12 14 16 18
32°
28°
25°
19°
12°
d
PEO/PMMA:60/40:WSR/HM
Range 2 mCal/sec
CS 10 mm/min

figure 35

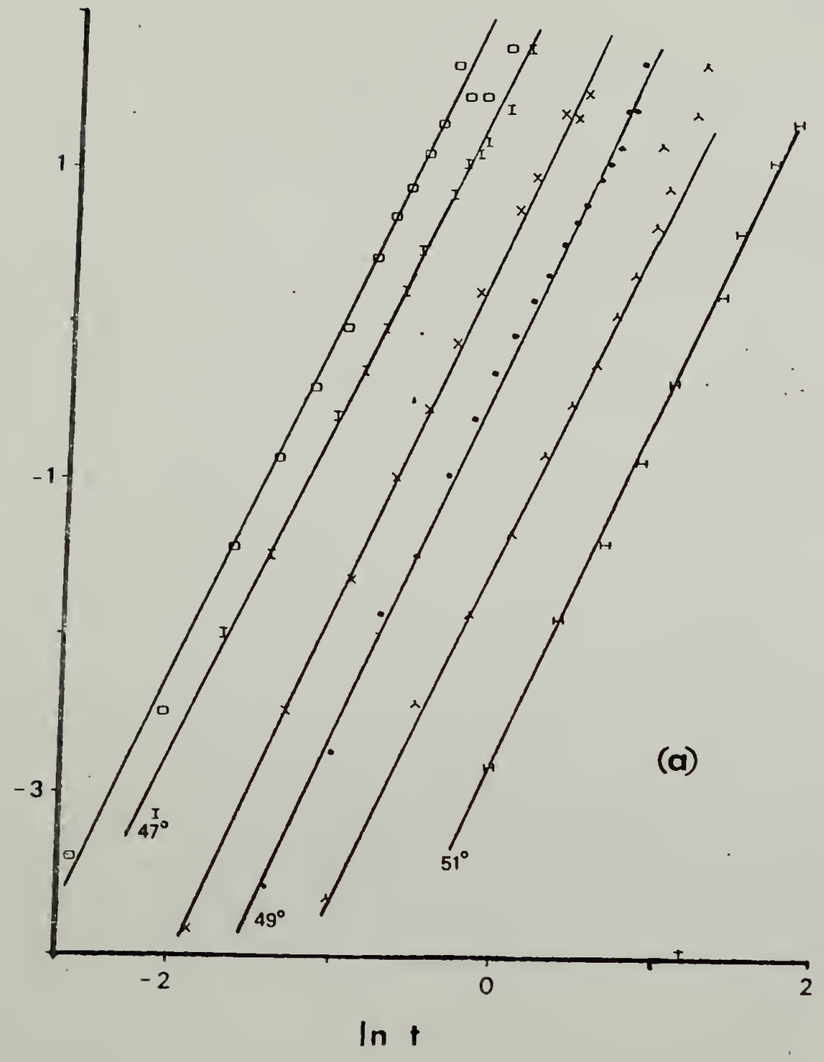
ln ln Θ
1
-1
-3
47°
49°
51°
-2
0
2
ln t
(a)

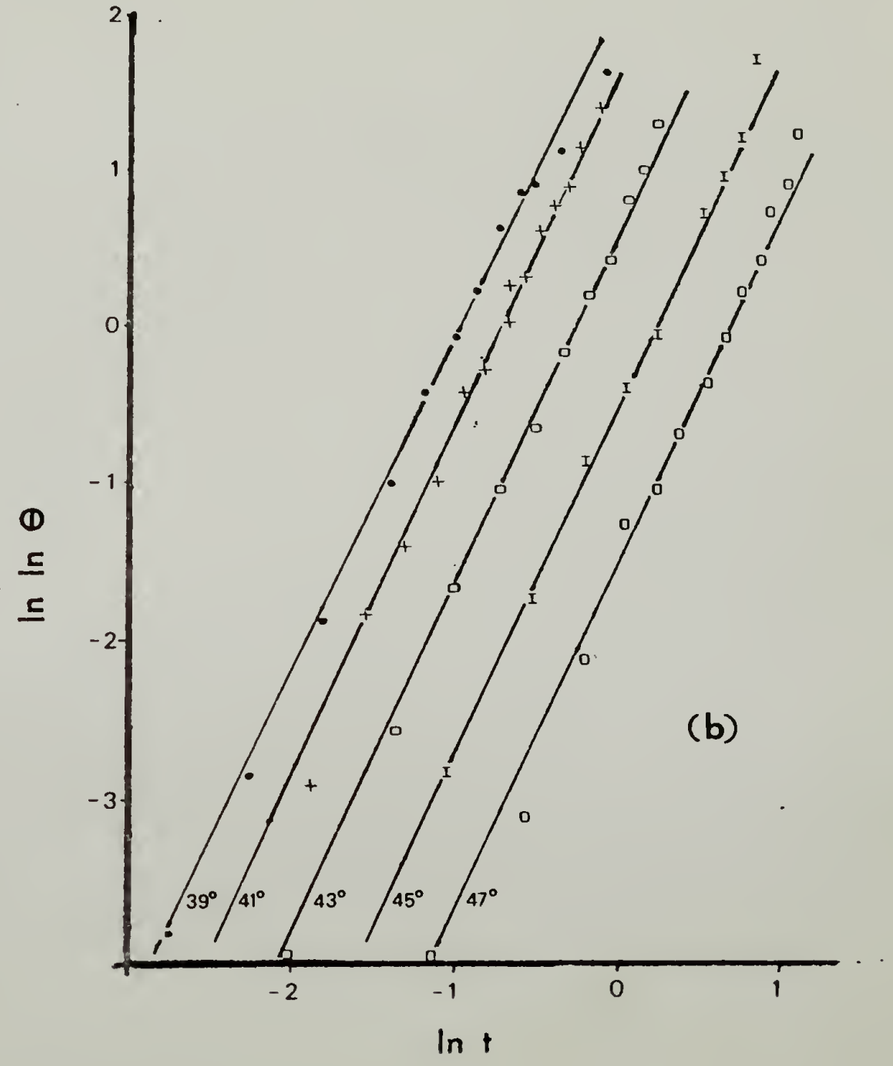
ln ln Θ
2
1
0
-1
-2
-3
39°
41°
43°
45°
47°
-2
-1
0
1
ln t
(b)

figure 36

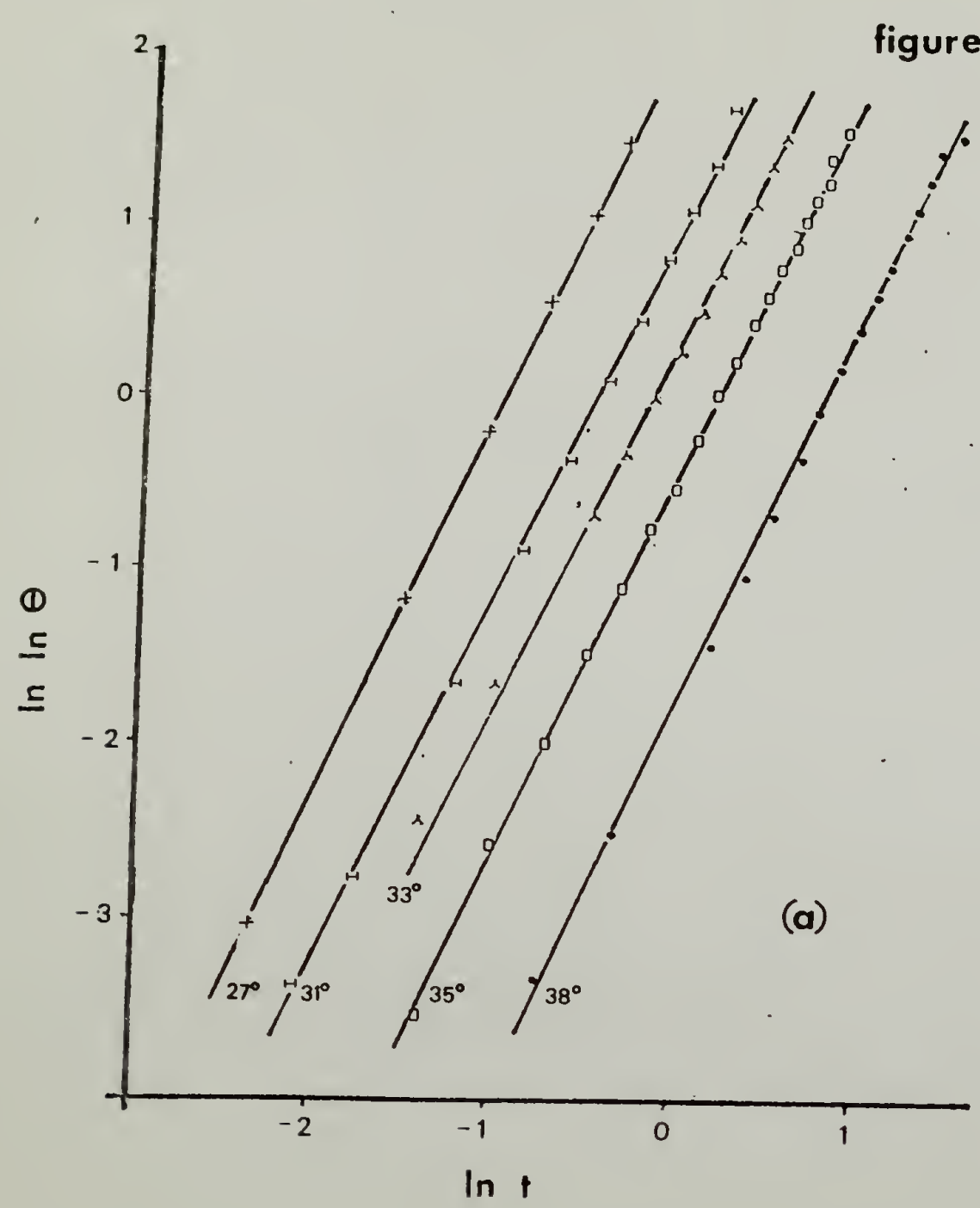
2
1
0
-1
-2
-3
ln ln Θ
-2
-1
0
1
ln t
27°
31°
33°
35°
38°
(a)

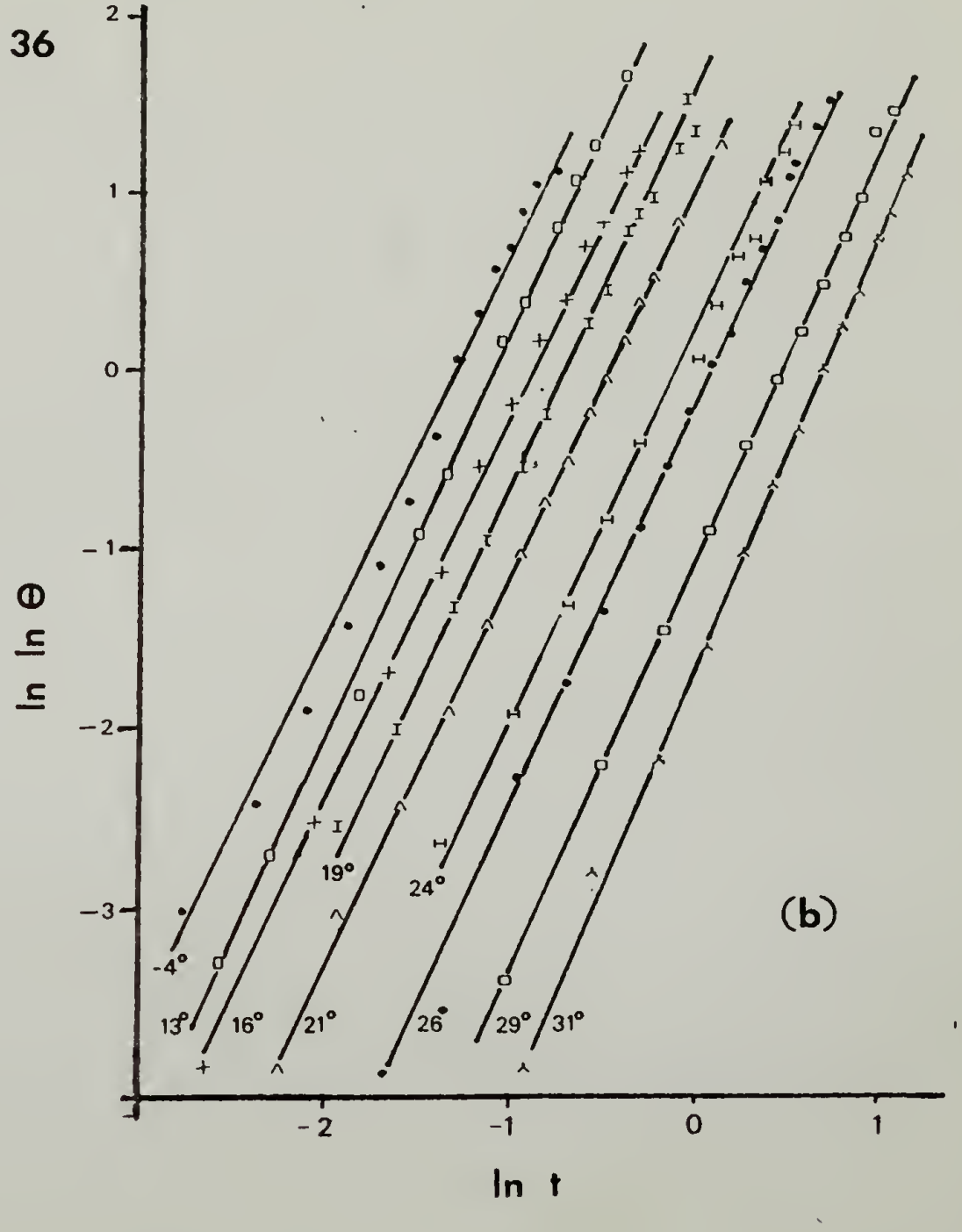
2
1
0
-1
-2
-3
ln ln Θ
-2
-1
0
1
ln t
-4°
13°
16°
19°
21°
24°
26°
29°
31°
(b)

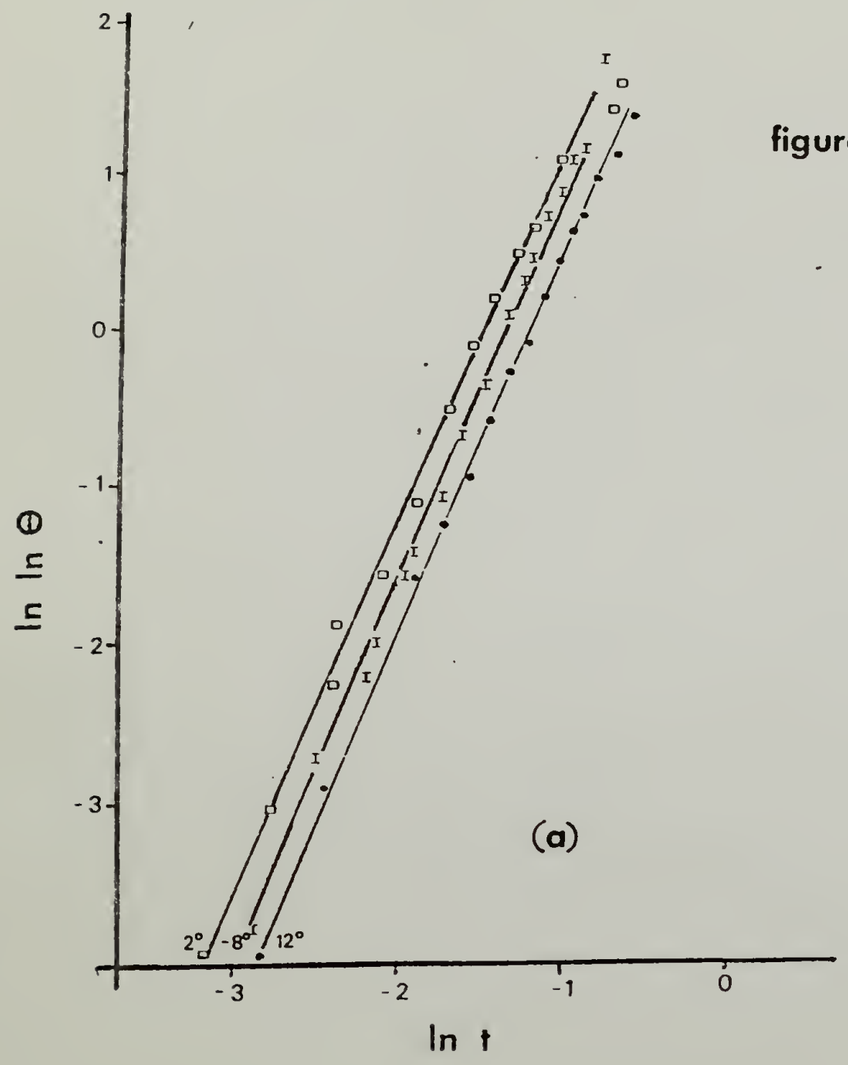

figure 37

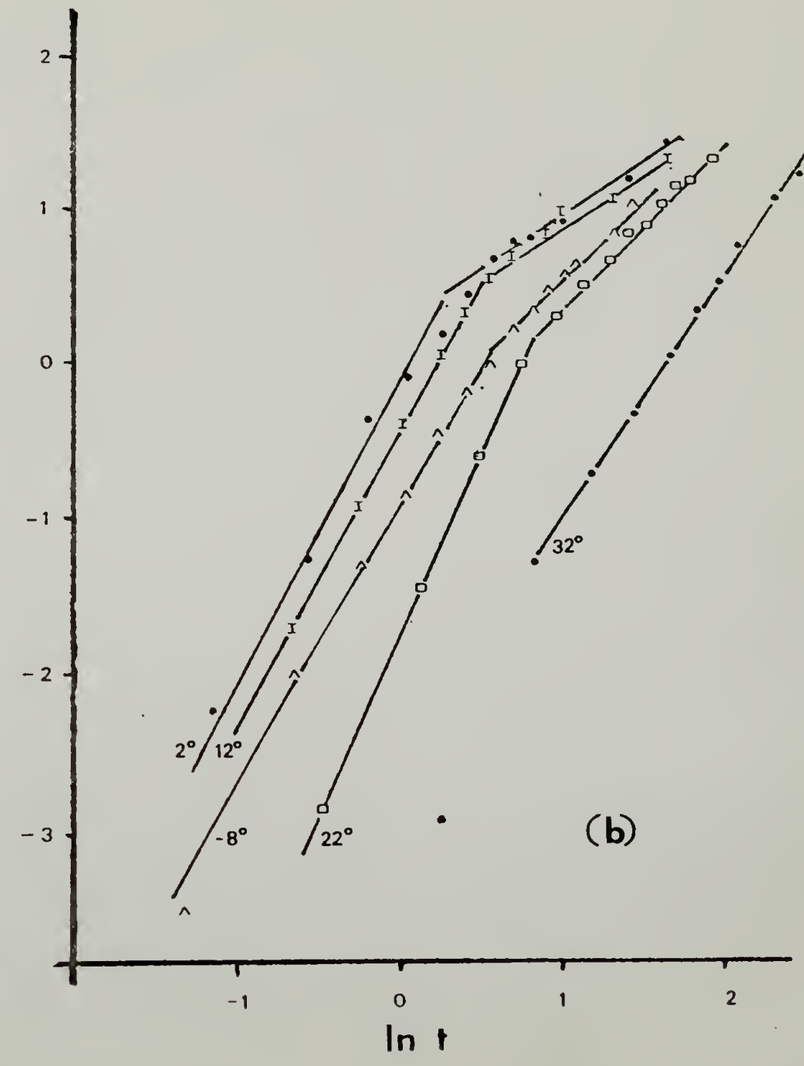

figure 38

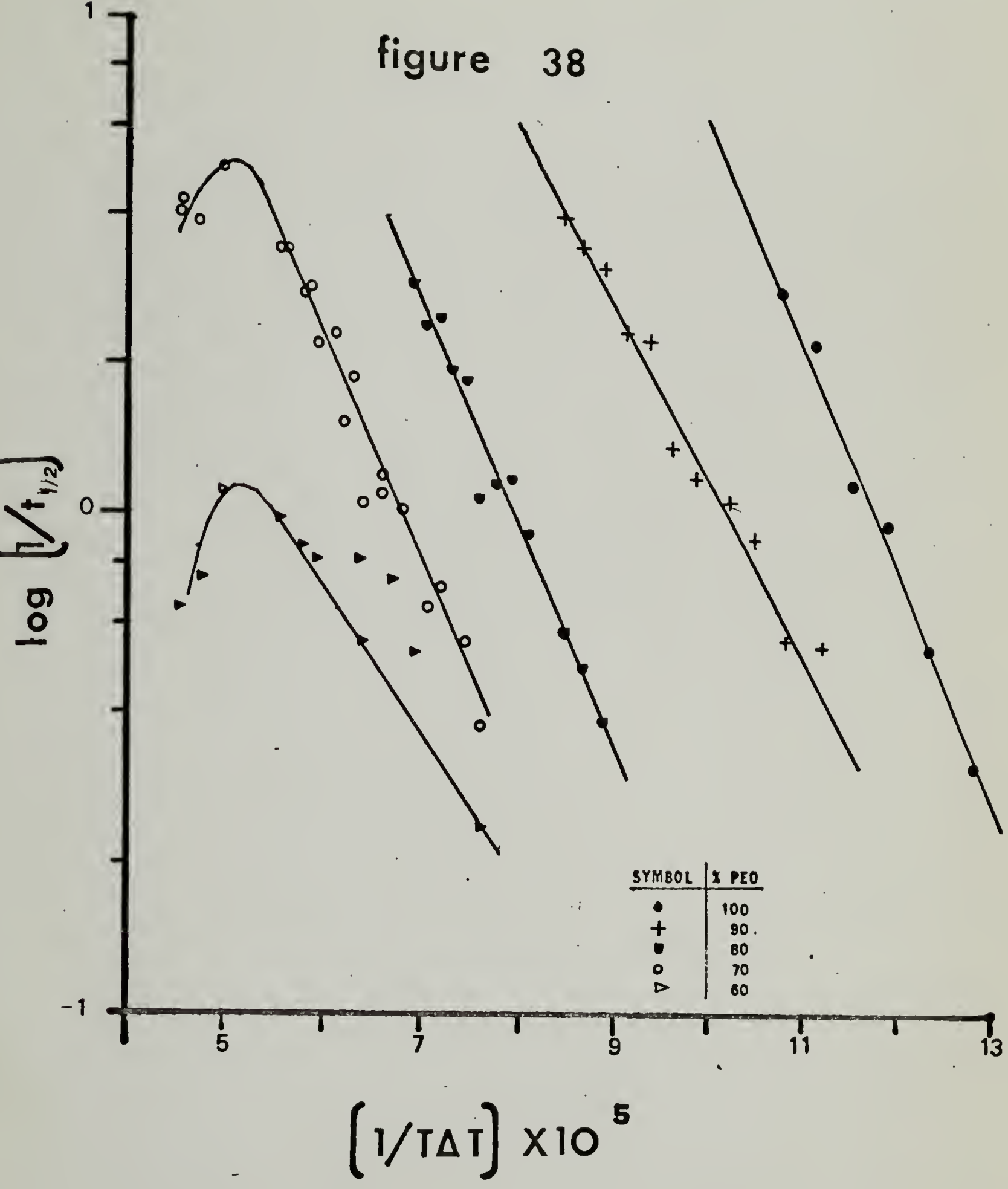

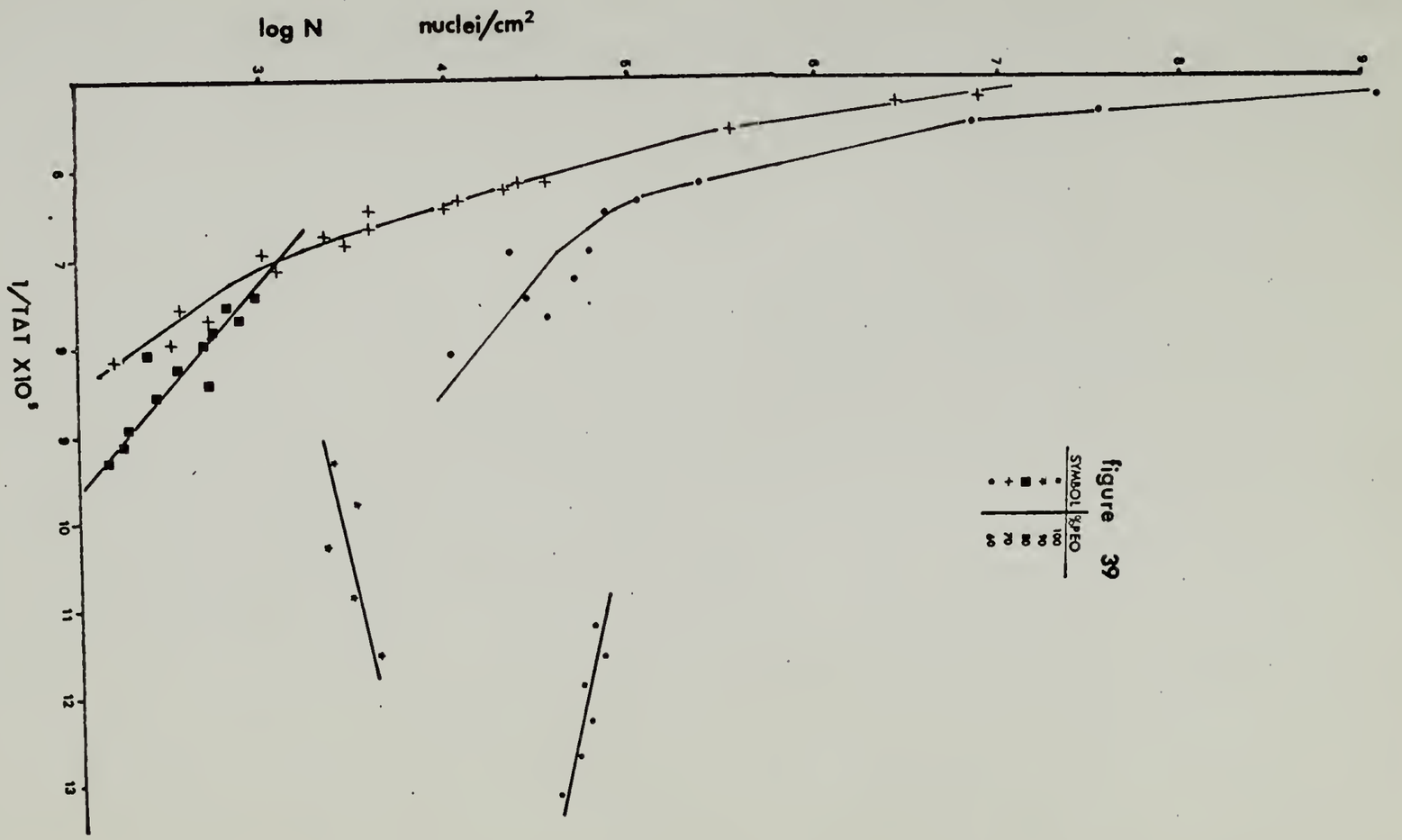

figure 39

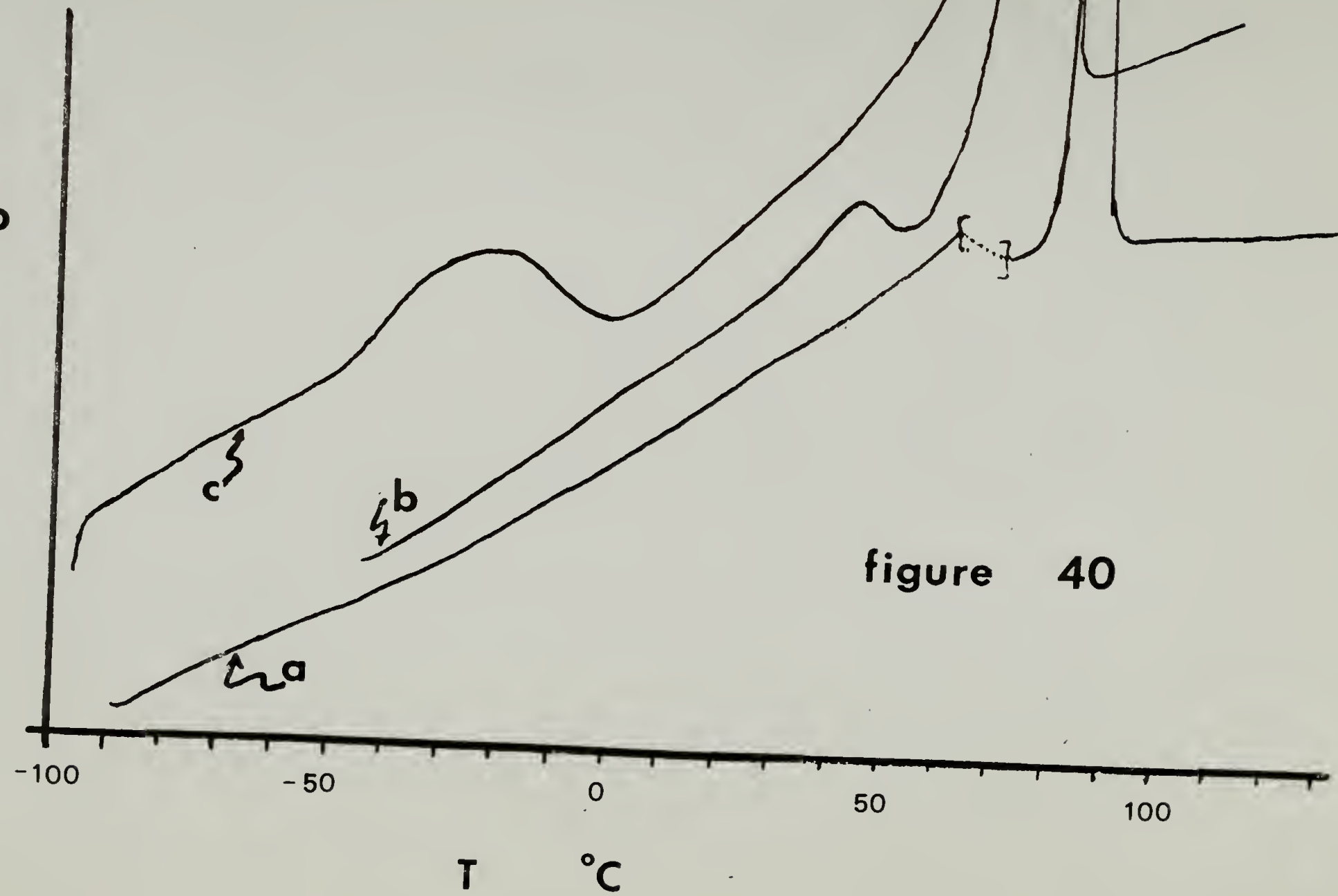

figure 40

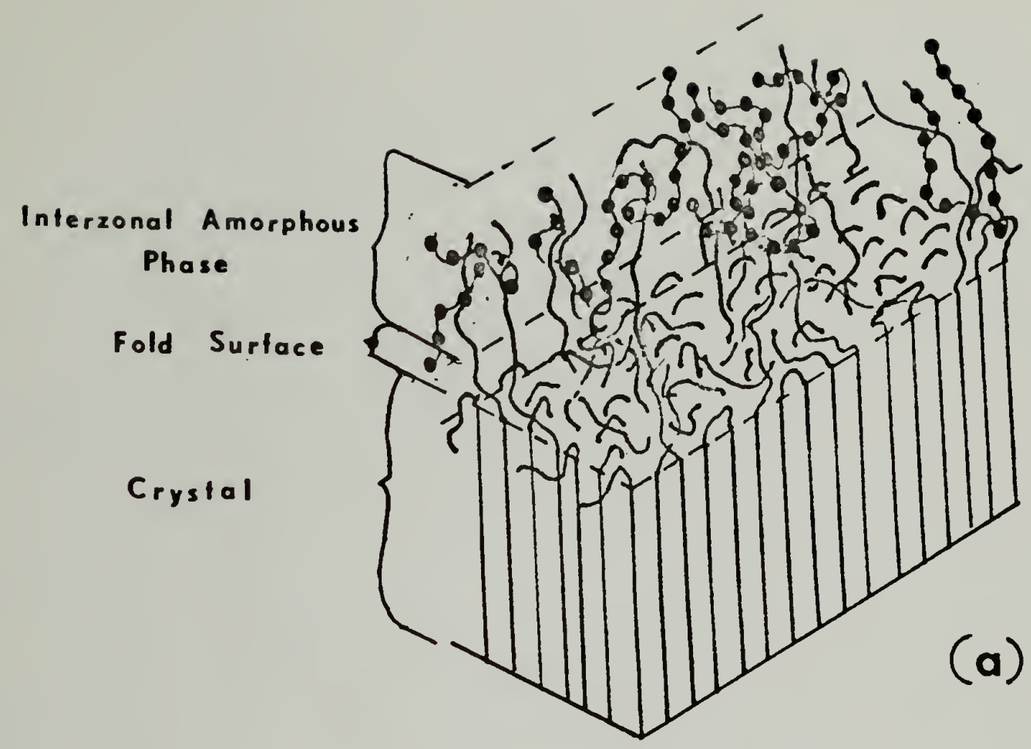
Interzonal Amorphous Phase
Fold Surface
Crystal
(a)
Intersticial Phase
Interfacial Zone
Crystal
(b)

figure 41

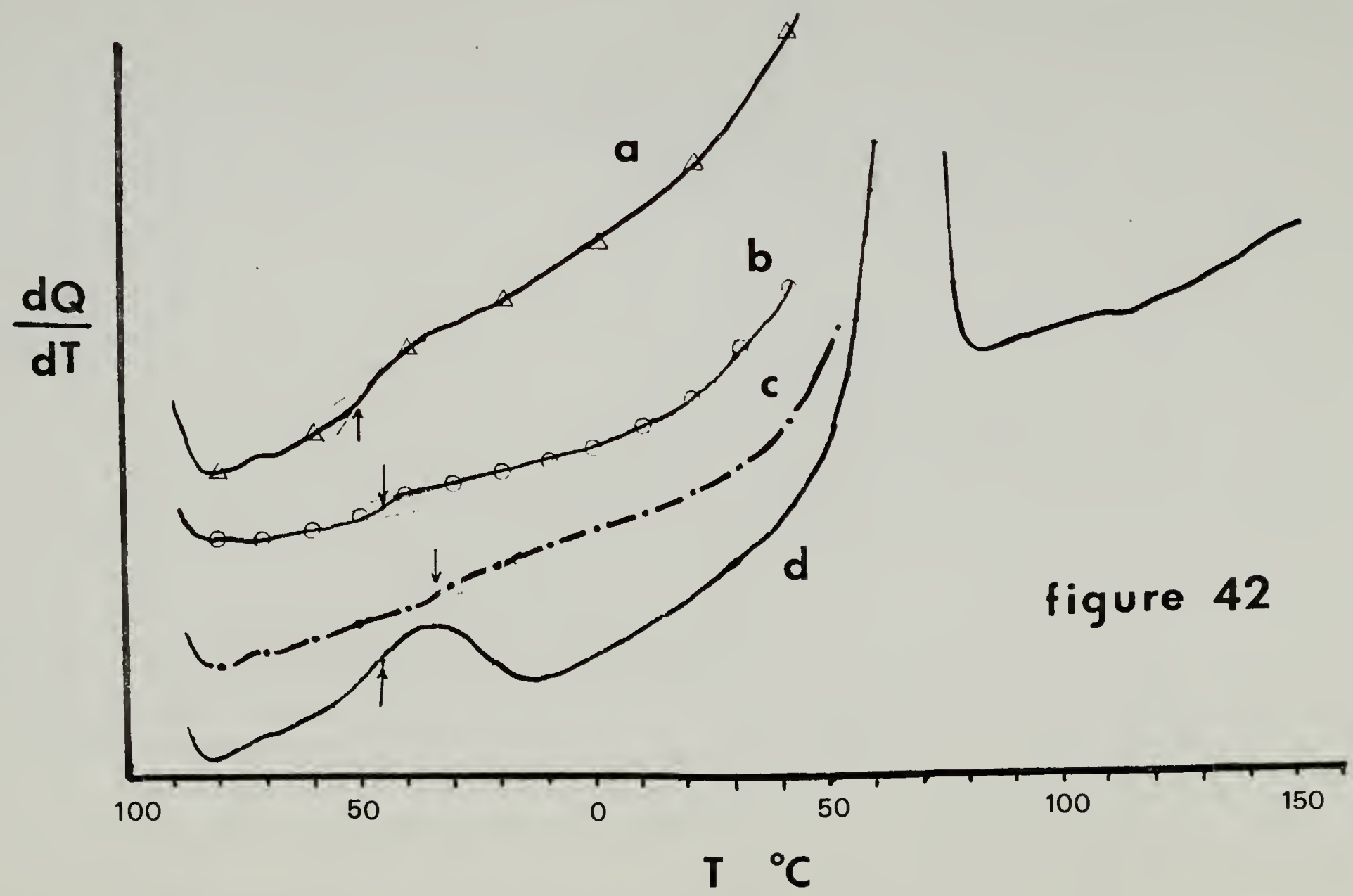

figure 42

figure 43

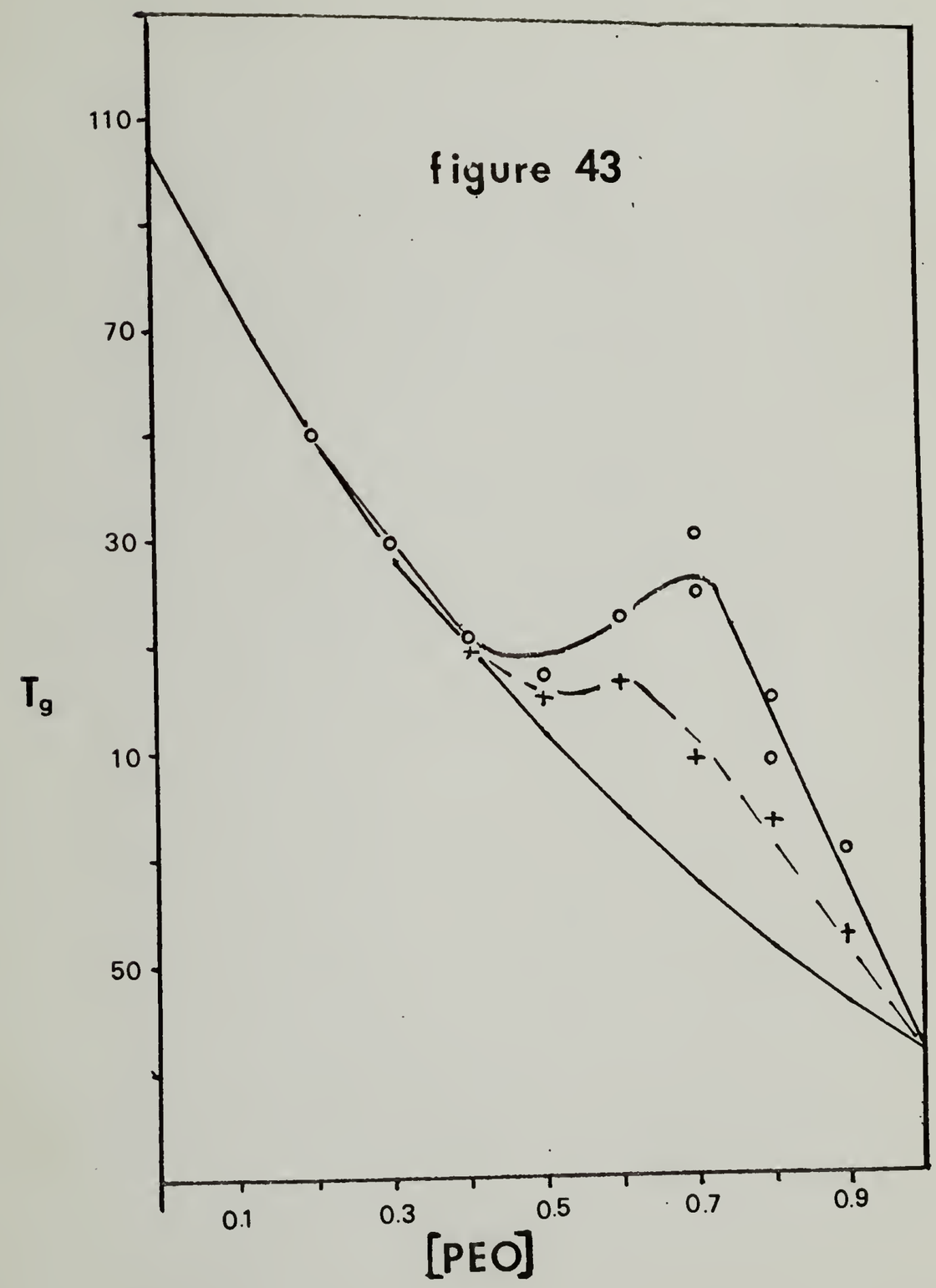

figure 44

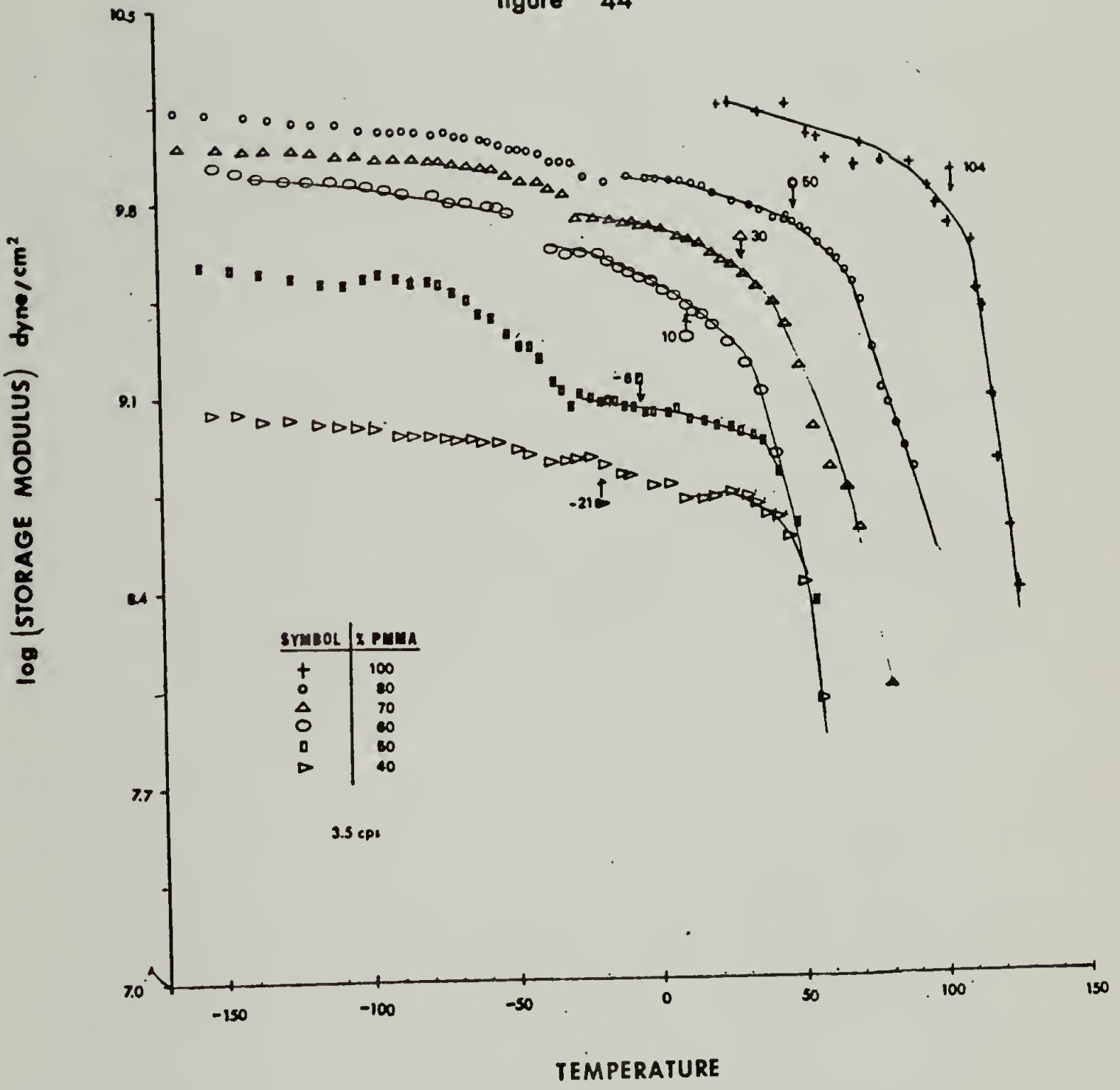
log (STORAGE MODULUS) dyne/cm²
10.5
9.8
9.1
8.4
7.7
7.0
-150
-100
-50
0
50
100
150
TEMPERATURE
SYMBOL | % PMMA
+ 100
o 80
Δ 70
O 60
□ 50
▷ 40
3.5 cps
50
30
10
-8
-21
104

figure 45

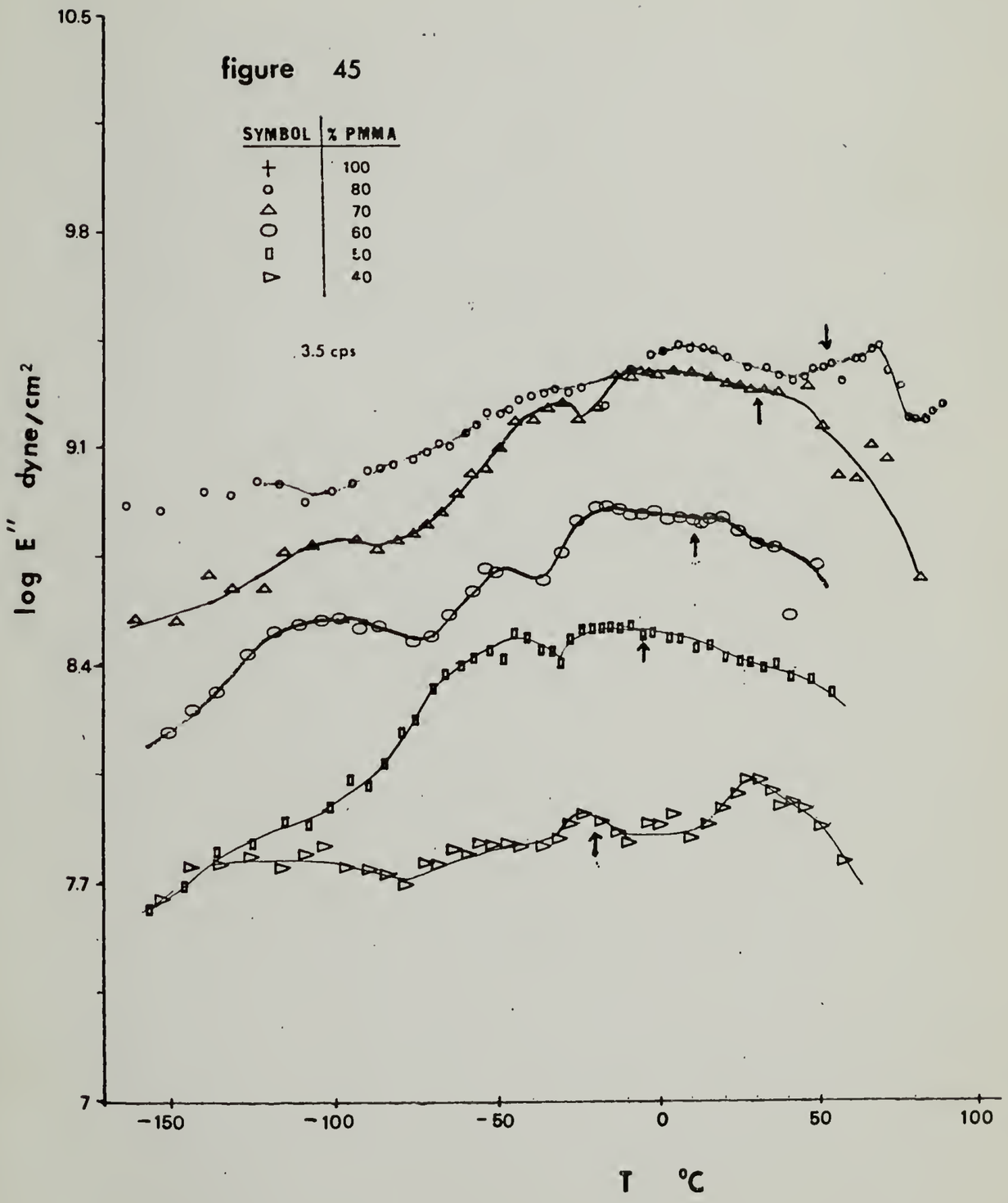
SYMBOL | % PMMA
+ | 100
o | 80
Δ | 70
O | 60
□ | 50
▷ | 40
3.5 cps
log E'' dyne/cm²
10.5
9.8
9.1
8.4
7.7
7
−150
−100
−50
0
50
100
T °C

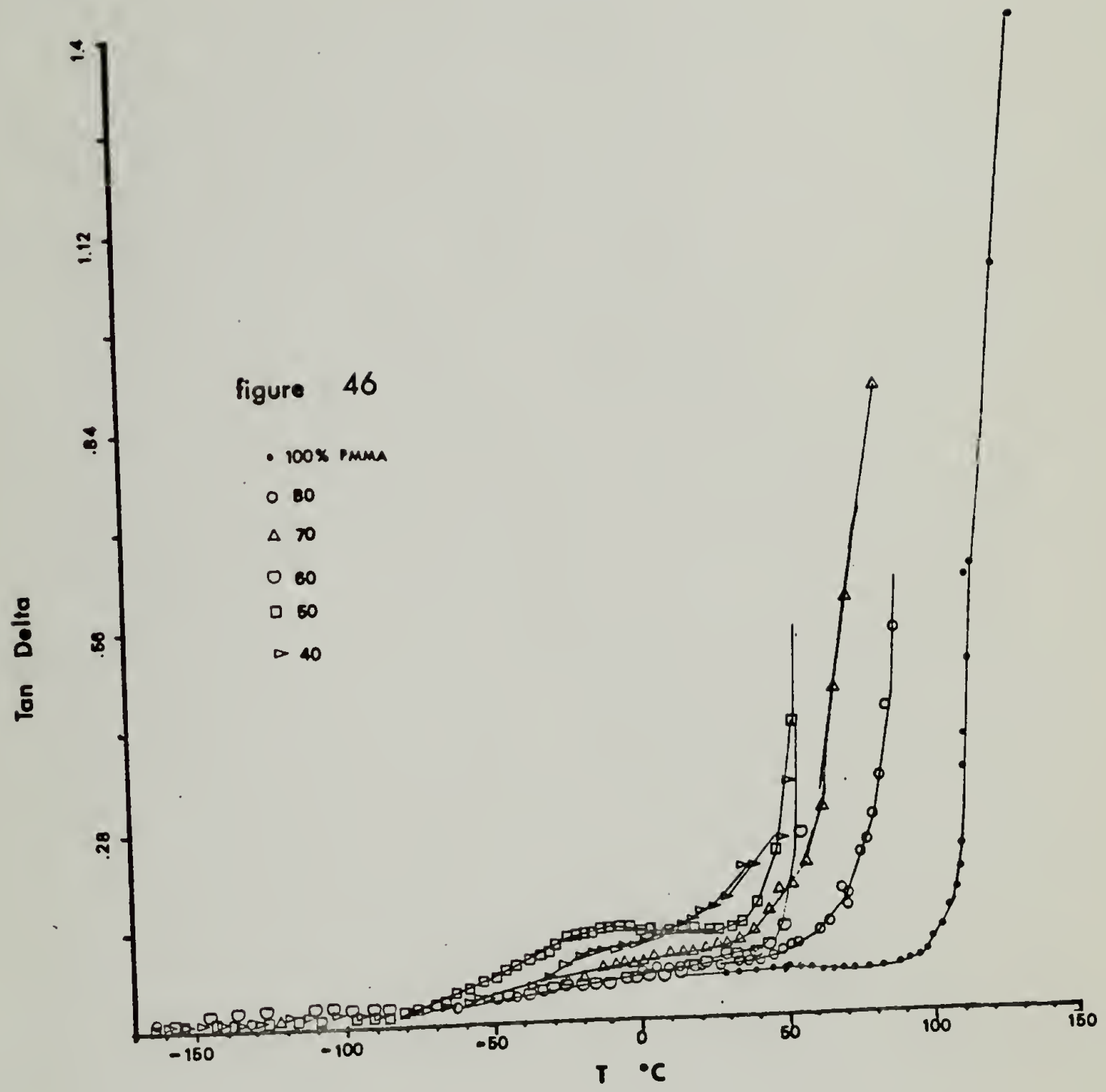
Tan Delta
1.4
1.12
.84
.56
.28
• 100% PMMA
○ 80
△ 70
○ 60
□ 50
▷ 40
-150
-100
-50
0
50
100
150
T °C

figure 46